SANDIA REPORT

SAND2006-3362
Unlimited Release
Printed June 2006

Acceleration of Dormant Storage Effects to Address the Reliability of Silicon Surface Micromachined Micro-Electro-Mechanical Systems (MEMS)

Michael T. Dugger, Danelle M. Tanner, Jeremy A. Walraven, James V. Cox, Troy J. Skousen, James A. Ohlhausen, Mark W. Jenkins, Bernie Jokiel, Ted B. Parson, Sam A. Candelaria, Michelle A. Duesterhaus, and Shannon J. Timpe

Prepared by
Sandia National Laboratories
Albuquerque, New Mexico 87185 and Livermore, California 94550

Sandia is a multiprogram laboratory operated by Sandia Corporation, a Lockheed Martin Company, for the United States Department of Energy's National Nuclear Security Administration under Contract DE-AC04-94AL85000.

Issued by Sandia National Laboratories, operated for the United States Department of Energy by Sandia Corporation.

Available to DOE and DOE contractors from
U.S. Department of Energy
Office of Scientific and Technical Information
P.O. Box 62
Oak Ridge, TN 37831

Telephone: (865)576-8401
Facsimile: (865)576-5728
E-Mail: reports@adonis.osti.gov
Online ordering: http://www.osti.gov/bridge

Available to the public from
U.S. Department of Commerce
National Technical Information Service
5285 Port Royal Rd
Springfield, VA 22161

Telephone: (800)553-6847
Facsimile: (703)605-6900
E-Mail: orders@ntis.fedworld.gov
Online order: http://www.ntis.gov/help/ordermethods.asp?loc=7-4-0#online

SAND2006-3362
Unlimited Release
Printed June 2006

Acceleration of Dormant Storage Effects to Address the Reliability of Silicon Surface Micromachined Micro-Electro-Mechanical Systems (MEMS)

Michael T. Dugger, Danelle M. Tanner, Jeremy A. Walraven, James V. Cox, Troy J. Skousen, James A. Ohlhausen, Mark W. Jenkins, Ted B. Parson, Sam A. Candelaria, Michelle A. Duesterhaus and Shannon J. Timpe

Sandia National Laboratories
P.O. Box 5800
Albuquerque, New Mexico 87185-0889

Abstract

Qualification of microsystems for weapon applications is critically dependent on our ability to build confidence in their performance, by predicting the evolution of their behavior over time in the stockpile. The objective of this work was to accelerate aging mechanisms operative in surface micromachined silicon microelectromechanical systems (MEMS) with contacting surfaces that are stored for many years prior to use, to determine the effects of aging on reliability, and relate those effects to changes in the behavior of interfaces. Hence the main focus was on "dormant" storage effects on the reliability of devices having mechanical contacts, the first time they must move.

A large number (~1000) of modules containing prototype devices and diagnostic structures were packaged using the best available processes for simple electromechanical devices. The packaging processes evolved during the project to better protect surfaces from exposure to contaminants and water vapor. Packages were subjected to accelerated aging and stress tests to explore dormancy and operational environment effects on reliability and performance.

Functional tests and quantitative measurements of adhesion and friction demonstrated that the main failure mechanism during dormant storage is change in adhesion and friction, precipitated by loss of the fluorinated monolayer applied after fabrication. The data indicate that damage to the monolayer can occur at water vapor concentrations as low as 500 ppm inside the package. The most common type of failure was attributed to surfaces that were in direct contact during aging.

The application of quantitative methods for monolayer lubricant analysis showed that even though the coverage of vapor-deposited monolayers is generally very uniform, even on hidden surfaces, locations of intimate contact can be significantly depleted in initial concentration of lubricating molecules. These areas represent defects in the film prone to adsorption of water or contaminants that can cause movable structures to adhere. These analysis methods also indicated significant variability in the coverage of lubricating molecules from one coating process to another, even for identical processing conditions. The variability was due to residual molecules left in the deposition chamber after incomplete cleaning. The coating process was modified to result in improved uniformity and total coverage. Still, a direct correlation was found between the resulting static friction behavior of MEMS interfaces, and the absolute monolayer coverage.

While experimental results indicated that many devices would fail to start after aging, the modeling approach used here predicted that all the devices should start. Adhesion modeling based upon values of adhesion energy from cantilever beams is therefore inadequate. Material deposition that bridged gaps was observed in some devices, and potentially inhibits start-up more than the adhesion model indicates. Advances were made in our ability to model MEMS devices, but additional combined experimental-modeling studies will be needed to advance the work to a point of providing predictive capability. The methodology developed here should prove useful in future assessments of device aging, however. Namely, it consisted of measuring interface properties, determining how they change with time, developing a model of device behavior incorporating interface behavior, and then using the age-aware interface behavior model to predict device function.

Acknowledgments

The work of Robin Jacobs-Gedrim in the die and package testing of over 1000 parts is gratefully acknowledged. This work would not have been possible without the support of Elizabeth Huffman in developing ultrahigh vacuum tubes with appropriate fixtures for aging packaged MEMS in controlled environments, and that of Scot Swanson in setting up an oven array used in the experiments. Mike Baker furnished the single bit mechanical memory design and performed calculations. Alex Corwin and Maarten DeBoer provided insight into surface adhesion measurements using cantilever beams. The work of Adam Hook (North Carolina State University) to investigate coverage of chemisorbed monolayers and associated friction of MEMS tribometer devices is appreciated. The authors are also grateful for the assistance of Bill Wallace with XPS measurements, Michael Rye's help with FIB sections, and Josh Wiehn's AFM measurements.

Contents

List of Figures

Page

List of Tables

Page

Nomenclature

AFM	Atomic Force Microscope
CBA	Cantilever Beam Array
DIP	(Ceramic) Dual in Line Package
DMS	Discriminating Micro Switch
ESD	Electrostatic Discharge
FIB	Focused Ion Beam
FOTAS	perfluoro-octyltris(dimethylamino)silane, $C_8F_{13}H_4Si(CH_3CH_3N)_3$
MEMS	MicroElectroMechanical System
NVM	Non-Volatile Memory
RDC	Release, Dry, Coat
SEM	Secondary Electron Microscopy
SNL	Sandia National Laboratories
ToF-SIMS	Time-of-Flight Secondary Ion Mass Spectrometry
TRA	Torsional Ratcheting Actuator
VSAM	Vapor-deposited Self-Assembled Monolayer
XPS	X-ray Photoelectron Spectroscopy

1. Introduction

Many MEMS devices have applications where they sit in storage for a long period of time and then must operate when requested. If the device is complex with surfaces in contact, surface interactions over time can determine whether a device functions or not.

A critical factor in the long term reliability of surfaces in contact during storage is the stability of monolayer coupling agents applied during processing to reduce adhesion. These coatings are popular processing aides because they can be applied at the back end of the manufacturing line, thus having no impact on the fabrication process. The coatings are typically one molecule thick, and as such do not modify the stress state of the polycrystalline silicon layers. The adsorbed films are also self-limiting in thickness, and can penetrate in either the liquid or vapor phase to coat deeply hidden interfaces.

Qualification of microsystems for defense applications is critically dependent on our ability to build confidence in their performance by accurately predicting the evolution of their behavior over time in the stockpile. Understanding the effects of dormant storage on device performance is the greatest challenge we face to insure reliable operation of devices over required stockpile service life. The SUMMiT V module and test structures described here were used to provide data in accelerated test conditions to develop fundamental understanding of the aging mechanisms involved.

There are several principal objectives of this work. The first is to determine whether failures in complex MEMS devices can be accelerated using high temperatures and controlled humidity environments consistent with packaging processes. It is known that very high levels of humidity will cause hydrolysis of the monolayers [1.1], but effects such as these have not been documented for water vapor concentrations in the hundreds to thousands of ppm. The second objective is to relate these failures to measurable changes in the behavior of contacting surfaces using test structures and surface analysis techniques. In particular, this project sought to examine failures due to dormant (non-moving) storage of devices, rather than examine the maximum operational lifetime of devices. This is particularly relevant to the use of MEMS devices in future weapon applications. Finally, this project seeks to relate device operation to interface behavior for real devices after exposure to realistic processing environments, making use of large numbers of packaged parts. The largest numbers of parts for any single program to date have been packaged as part of this project, and this has provided many insights into the role of packaging processes reproducibility on device functionality.

1.1 Module Design

There were three versions of the SUMMiT V module fabricated for this work. As structures were tested, we gained knowledge which lead to improved designs. The main philosophy for module design was to have prototype surety-like devices (aka “functional” devices) on the same module with diagnostic structures for measuring attributes of the

surfaces and interfaces. In this way, the behavior of the functional devices might be related to measurable behavior of surfaces and interfaces, such as surface chemistry, adhesion, and friction response.

The first version of the module contained a microengine-driven gear train (DMS), mechanical non-volatile memory (NVM), pulltabs for fracture strength measurement, square cuts to the single crystal Si for AFM measurements of monolayer behavior or agglomeration, a sidewall MEMS tribometer for friction measurement, two beam-in-cave structures for examining coverage on hidden surfaces, and a cantilever beam array for adhesion measurement.

In the second version, the NVM was upgraded to a more robust design with the ability to carry more current in the thermal actuator legs. This prevented accidental over-voltage effects. In addition, power and ground lines were re-routed using an over/under approach which substantially reduced the number of bond pads. One of the beam-in-cave structures was replaced with surface characterization flaps in this version.

In the third version, we replaced the microengine actuator with a TRA to drive the gears in the DMS. It was found in testing that the microengine-driven gears did not yield well through the die-attach process. This was probably because the microengine is the weakest of all SUMMiT V actuators, only managing an output force of roughly 9 μN with a voltage of 80V. The move to a TRA actuator which has smaller size enabled the added bonus of using two DMS per module. Additionally, some of the comb fingers which are susceptible to electrostatic discharge were removed. A final modification of removing all dimples prevented failures due to a dimple groove issue. An AutoCAD layout of the final module design is shown in Figure 1.1.

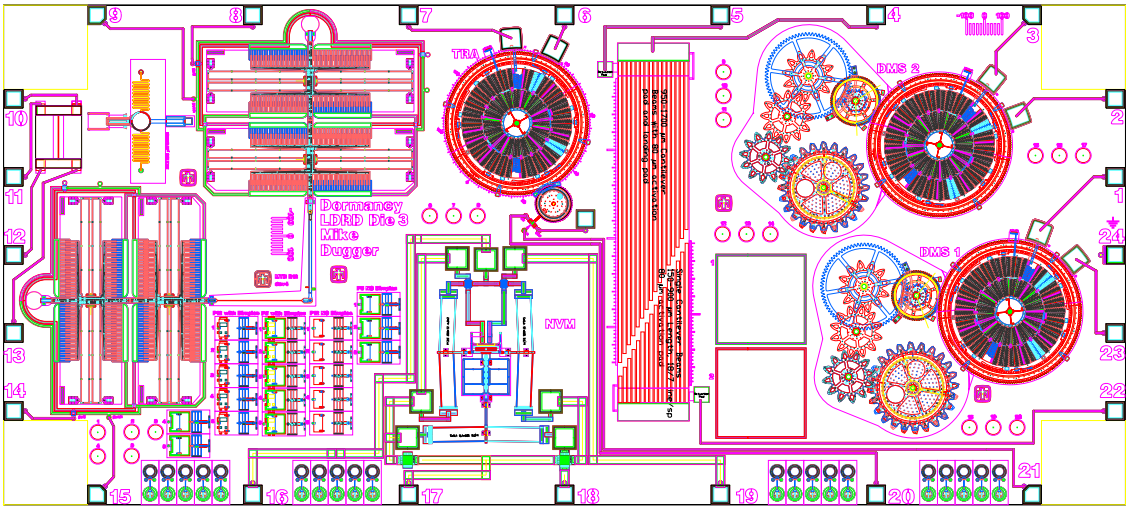

Figure 1.1 AutoCAD drawing of Dormancy Die 3, containing prototype surety (aka "functional") devices as well as diagnostic test structures.

1.2 Test Structures

The "dormancy module" contains functional devices such as a Discriminating Microswitch (DMS) gear train, a Torsional Ratcheting Actuator (TRA), and a single bit of Non-Volatile Memory (NVM). Diagnostic structures include a cantilever beam array (CBA) for adhesion measurement, a sidewall tribometer for friction studies, and occluded region structures for investigating the chemistry of hidden surfaces.

1.2.1 Functional Devices

We used three functional devices to represent possible defense applications. The TRA device is an electrostatic actuator driving a single load gear. The DMS device is an electrostatic actuator driving a special arrangement of six gears. The NVM device is a thermally-actuated latching switch.

TRA Device

The TRA device uses rotational comb drives for electrostatic operation and in this case drives a single gear and toggle beam [1.2]. A large circular frame ties the movable banks of combs together. An SEM image of the fabricated device is shown in Figure 1.2. Four cantilever beams support this frame in its center and act as the frame's spring return. These four beams are stiff to any lateral motion of the frame but compliant to rotation. There are three ratchet pawls and three anti-reverse pawls located symmetrically around the ring gear. Four guides are used to maintain alignment of the ring gear, constraining motion along the x, y, and z planes. The TRA rotates the load gear which contains a toggle beam between the gear teeth that applies a tangential resisting force of 13 μN.

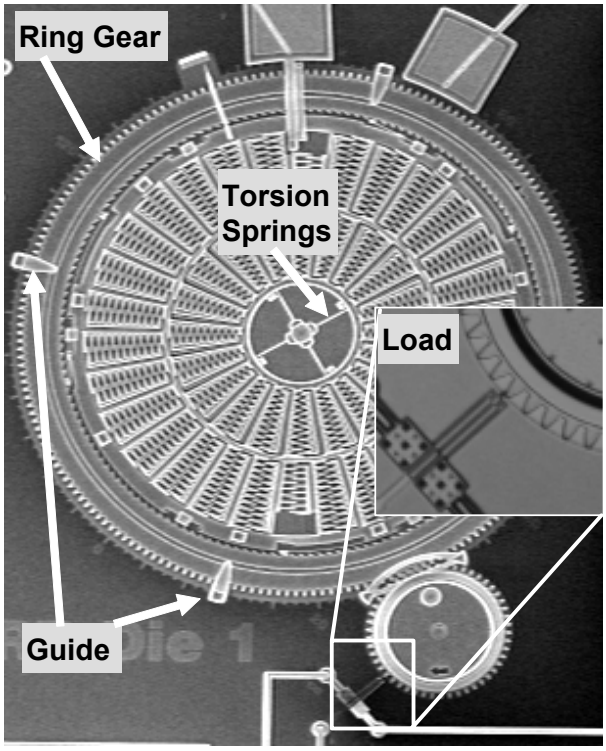

Figure 1.2 SEM image of the fabricated torsional ratcheting actuator showing the guide and ring mechanisms. The inset shows an enlarged view of the load gear and beam.

For operation, a periodic voltage is applied between the stationary and moving combs. As the voltage increases, the torsion frame rotates counter-clockwise about its springs in response to the electrostatic attraction. As the frame begins to rotate, the ratchet pawls engage the ring gear and cause it to rotate also (Figure 1.3). As the gear is rotating, the anti-reverse pawls are forced out of their engagement with the ratchet teeth. Once the ring gear has moved sufficiently, the anti-reverse pawls engage the next tooth. When the voltage is removed, the central torsion springs force the frame to return to its rest position. As the frame is returning, the ratchet pawls attempt to drag the ring gear in the reverse direction via friction of the ratchet pawls with the ring gear. Because the anti-reverse mechanisms have engaged, the ratchet pawls are forced to skip over the tooth and engage the next tooth. At this point, the frame has returned to its initial position, and the cycle can be repeated. For simple functionality tests, we use a modified saw-tooth pulse as shown in Figure 1.3. At a frequency of 10 Hz, the voltage is ramped up in 70 ms, stays high for 10 ms, and then falls to zero for the last 20 ms of the 100 ms pulse. The zero voltage section of the pulse allows the ratchet-pawl to return to the rest position. This type of pulse has provided consistently high yield for TRA actuators.

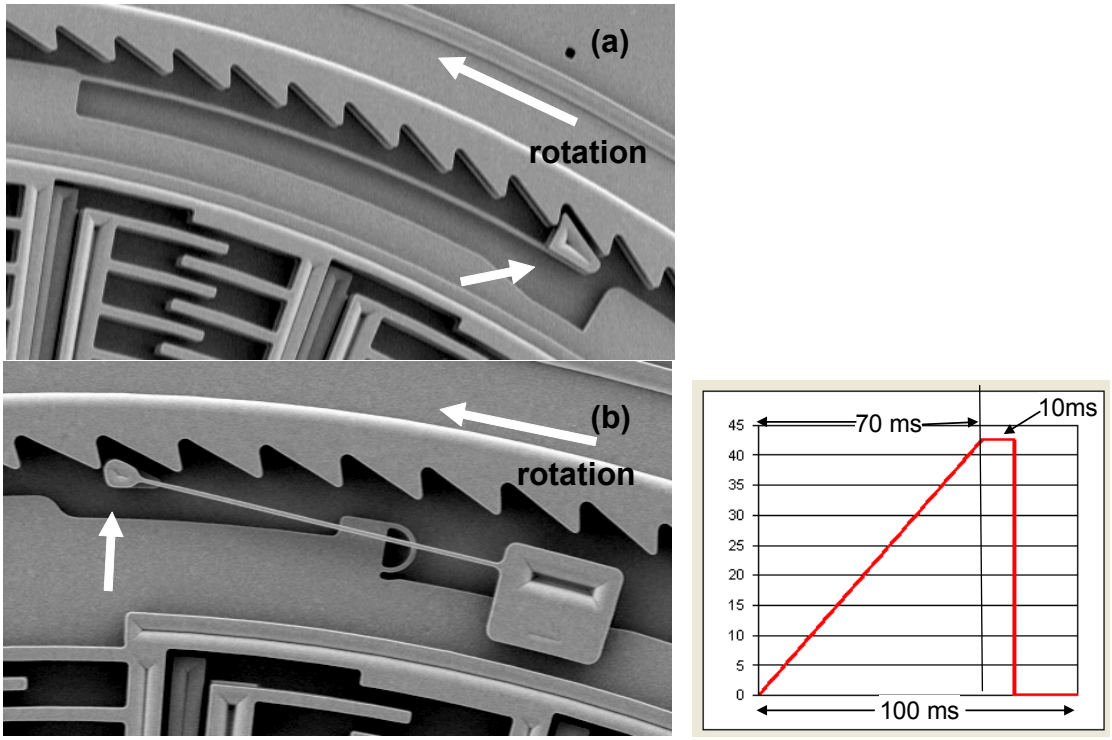

Figure 1.3 SEM images of the (a) ratchet pawl, and (b) anti-reverse pawl. The rotation direction of the ring gear is shown by the arrow. The applied voltage pulse is shown to the right of the image.

Two changes were made to the design of the TRA actuator in the course of these experiments. The first change reduced susceptibility to ESD events by removing comb fingers that had too small a gap. The other change removed all dimples in the design to prevent failure by the dimple getting stuck in a processing-related dimple groove. Both changes are discussed in the appendix of this report.

DMS Device

The DMS gear train was actuated with a microengine on the first two module designs. However, the microengine was a weak actuator where an 80 V input only yielded an output force of 9 μN [1.3]. A calculation was performed to estimate the TRA output force at 42.5V. The TRA transfers roughly 25 μN to the load gear. This higher output force made the TRA a more robust actuator and prompted the transition to it.

The DMS device consisted of a series of six gears (5 hubs). This is ½ of a counter-meshing discriminator designed for a real prototype MEMS surety device. These devices were tested with the same 42.5V pulsed saw tooth described earlier. An image of the DMS is shown in Figure 1.4.

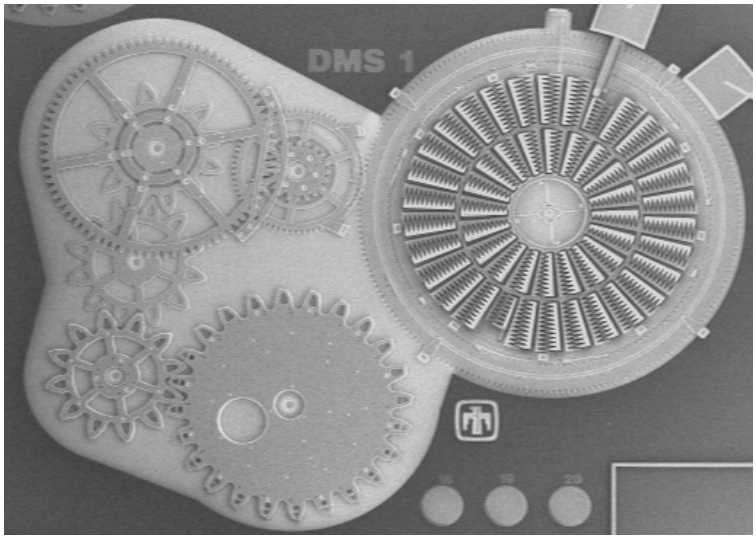

Figure 1.4 SEM image showing a DMS six-gear configuration.

NVM Device

The NVM is a single bit of a mechanical latching memory. It is operated by thermal actuators and is shown in Figure 1.5. The single actuator at the bottom of the image pushes the shuttle and closes the switch. At the same time, the latches engage which hold the grounded shuttle and bar to the contacts. To open the switch, current is forced through the left and right actuators, pulling the latches outward and disengaging the latch. The shuttle spring provides restoring force to pull the bar off of the contacts, thus opening the switch.

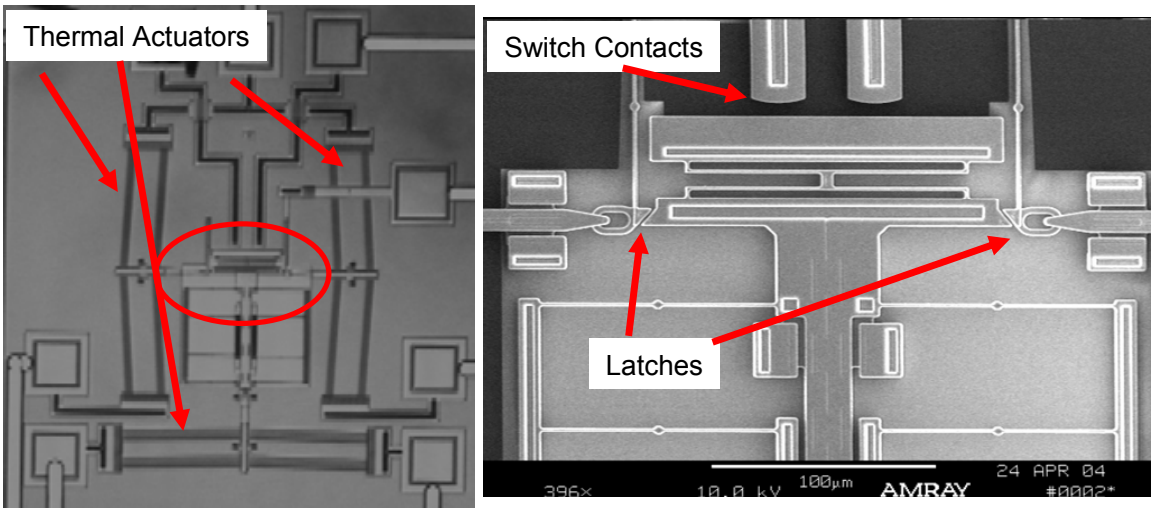

Figure 1.5 The entire NVM bit is shown in the left image with the three thermal actuators located by arrows. The right SEM image is an enlarged view of the switch area showing the contact points and the latches that hold the switch closed.

The first version of the NVM had very sensitive thermal actuator legs. It would latch at 13 V (23mA) and unlatch at 15V (27mA). Small excursions in voltage above these values would result in damage to the actuators. The more robust version had balanced thermal actuators so that an applied voltage of 7 V would cause enough movement to latch and unlatch the bit. We used wider power lines to minimize resistance effects on the current. Over-voltages could be tolerated without damage.

Devices of the new design were characterized using a DC power supply. The minimum voltages to latch or unlatch the device were recorded. A frequency plot of the results is shown in Figure 1.6. The operational voltage chosen was 7.5 V for the experiments because it should easily latch and unlatch all devices.

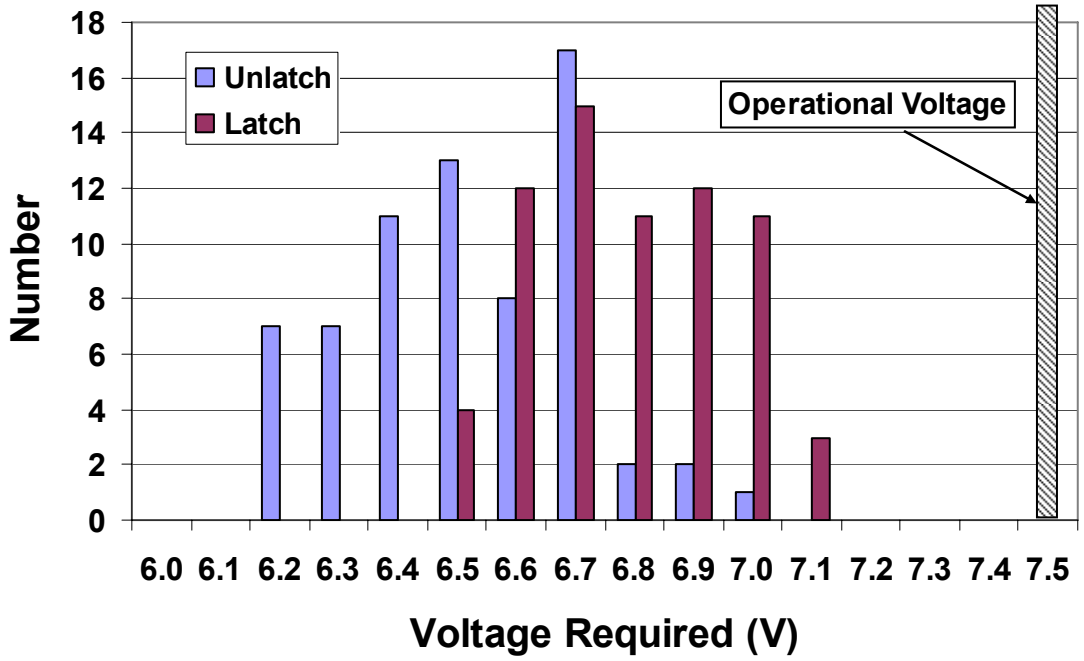

Figure 1.6 Unlatch thermal actuators require slightly less voltage than the latch thermal actuators in the NVM. The operational voltage chosen to encompass all actuators was 7.5 V.

The forces on the two contacting surfaces when latched were calculated. Based on nominal geometry assuming a 0.1 micron edge bias, we calculated the electrical contact spring stiffness to be 9.75 μN/μm. This is approximate as the spring geometry is not an exact match to the closed form equations and there exists uncertainty in the edge bias. Using this stiffness, we then calculate a 16 μN total force on the contacts in the closed position. The restoring spring stiffness was calculated to be 3.4 μN/μm, and when latched the displacement is 7.8 μm, so the restoring force (and also the force on the latches) is 27 μN.

1.2.2 Adhesion using Cantilever Beam Array

Each die has a cantilever beam array to allow surface adhesion characterization. An image of the array is shown in Figure 1.7. The array is composed of poly12 beams, 18-μm wide with a 7 μm gap between beams. The actuation region is an 80 μm wide pad under the beams. Application of voltage to this pad will bring the bottom surface of the beam into contact with the poly0 ground plane. After release of the voltage, the restoring force of the beams and the adhesive force of the surface will come to equilibrium.

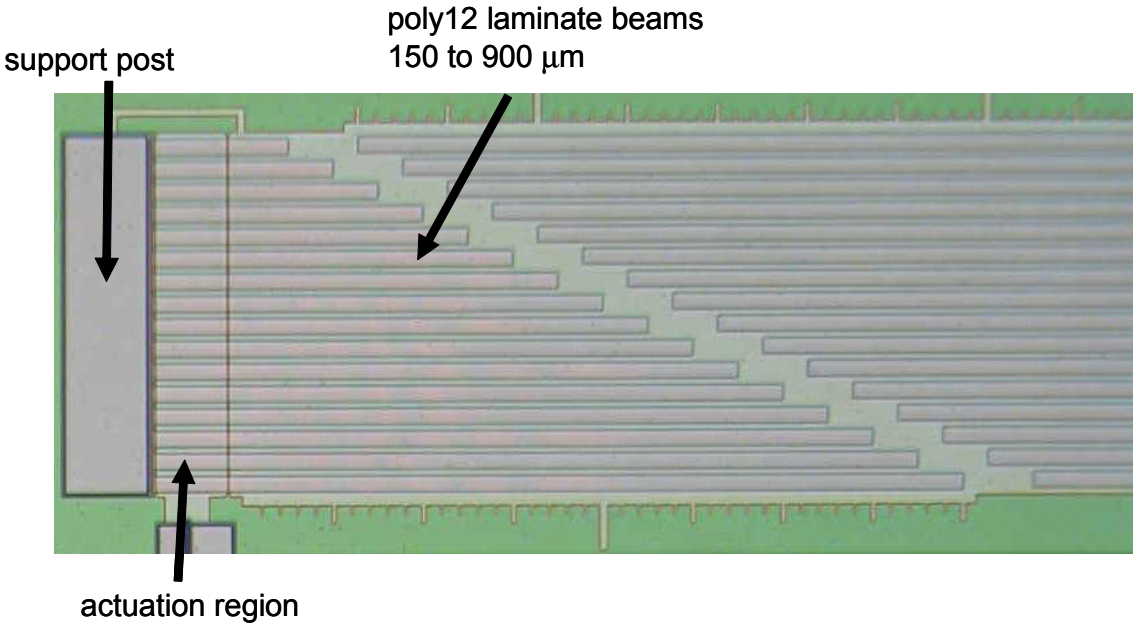

Figure 1.7 Cantilever beam array showing the support post that holds the poly12 beams, which can be brought into contact with the surface by applying voltage to the actuation region.

1.2.3 Friction using Sidewall Tribometer

Each die contains a device for measuring friction between sidewall surfaces. This type of contact occurs in the gear teeth of the TRA and DMS, the gear-hub of the DMS, and the latching points in the NVM. The sidewall friction device is shown in Figure 1.8.

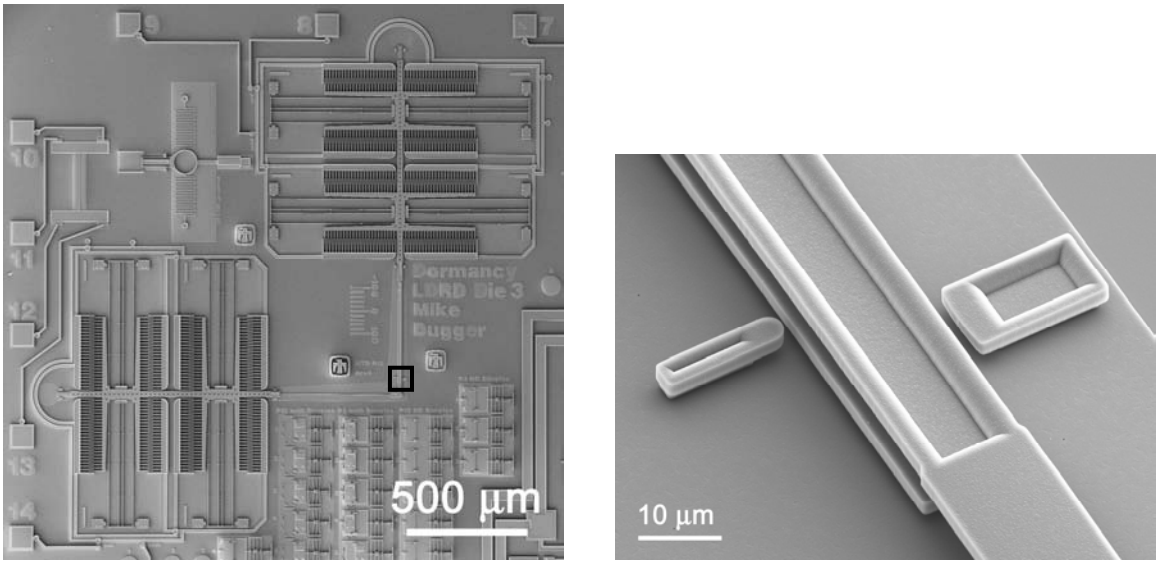

(a) (b)

Figure 1.8 SEM images of the sidewall friction device (a) and the movable beam (b) that may be pulled into contact with either of the fixed posts. The area represented in (b) is highlighted by the small black square in (a).

The MEMS sidewall tribometer uses two orthogonal bidirectional electrostatic actuators, one to pull a movable beam into contact with either of two fixed posts, and the other to oscillate the beam against the post. This device produces sliding contact between sidewall surfaces for which the morphology is determined by the processes used to etch the polycrystalline silicon. Contact occurs between poly12 layers in both the beam and the posts. Prior to measurement, the device is calibrated by determining the displacement versus applied voltage with no contact between the beam and posts. The measured voltage can then be used to compute the electrostatic force produced by the actuators, and the restoring forces exerted by the suspension springs can be computed from measured beam thicknesses. This device may be used in several different modes. For static friction measurement, the load actuator is used to pull the beam into contact with one of the posts, and then the tangential force is ramped up until the device slips. The tangential force at the moment of slip provides a measure of the static friction force. Dynamic friction force can be determined by oscillating the device at a known amplitude with no normal force applied between the beam and post. The beam is then loaded against the post, and the displacement is reduced due to friction at the beam/post interface. This reduction in displacement provides a measurement of the dynamic friction coefficient at the beam/post interface. This method is described in more detail in [1.4]. This device uses a rigid movable beam connected to the load actuator by a rotational joint. The rigid beam simplifies mechanical analysis of the structure to extract forces.

1.2.4 Occluded Regions

Each die contained structures designed to permit measurements of the coverage of intentionally-applied coatings and/or contaminants in hidden areas. In the first Dormancy module, a beam-in-cave structure was fabricated, as shown in Figure 1.9. This device consisted of a cantilever beam of poly3 in a cave defined by poly3 on the sides, poly4 on top and poly0 below. The central ring is used to manually pull the beam out of the cave against the force of the serpentine springs, and latches hold the beam out of the cave for analysis. The device can be coated in the as-fabricated position and then opened for analysis of the hidden surfaces. The primary difficulty with this device was that the beam was very narrow, and measurements by Time of Flight SIMS (ToF-SIMS, described later) were therefore dominated by edge effects.

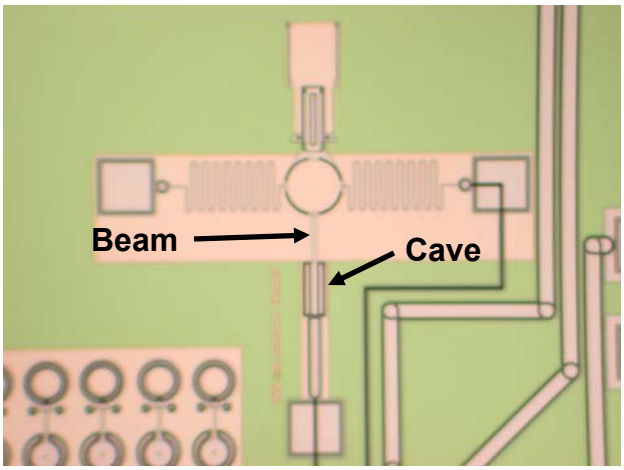

Figure 1.9 Beam-in-cave structure for measuring composition of hidden surfaces. The central ring is 100 μm in diameter.

A second type of structure was designed for Dormancy modules 2 and 3, after the initial experience with module 1. The flap structures were created to produce hidden surfaces for analysis that were larger than the beam-in-cave structures and that contained several different types of hidden surfaces. The flap structures are shown in Figure 1.10.

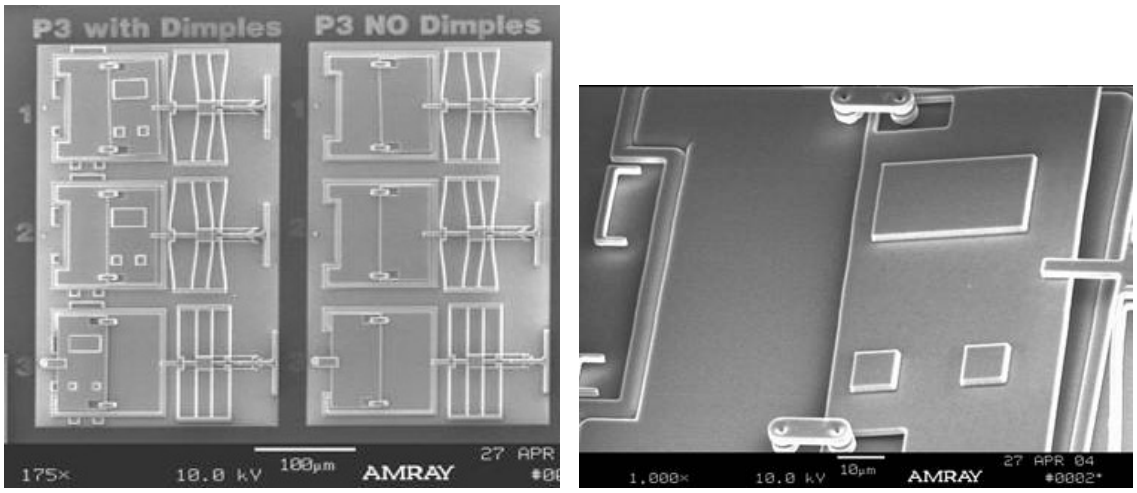

(a) (b)

Figure 1.10 SEM images of a bank of poly3 flaps (a), and a detail of the bottom of a poly3 flap with dimples after flipping over and latching into place. In (a), the top two rows of flaps have been flipped over and latched into place, while the bottom row remains in the as-fabricated position.

The flaps have tabs (left side in Figure 1.10a) that hold them in the as-fabricated position during removal of the sacrificial oxide. The flaps are hinged on the opposite side. After release and coating, the tabs can be manually broken off, and the flap flipped over to expose the hidden surface. A suspended latch is then pushed over the free end of the flap to hold it in place for analysis.

Chapter 1 References

1.1. U. Srinivasan, M.R. Houston, R.T. Howe, and R. Maboudian, "Alkyltrichlorosilane-Based Self-Assembled Monolayer Films for Stiction Reduction in Silicon Micromachines" *J. Microelectromechanical Systems* **7**, pp. 252-260, 1998.

1.2. S. Barnes, S. Miller, S. Rodgers, and F. Bitsie, "Torsional Ratcheting Actuating System," Inter. Conf. On Modeling and Simulation of Microsystems, San Diego, CA, March 2000, pp. 273-276.

1.3. D. M. Tanner et al., "MEMS Reliability: Infrastructure, Test Structures, Experiments, and Failure Modes," Sandia Report, SAND2000-0091, January 2000, pp 70-71.

1.4. D.C. Senft and M.T. Dugger, "Friction and Wear in Surface Micromachined Tribological Test Devices", Proc. of the SPIE - The International Society for Optical Engineering 3224, pp. 31-38, 1997.

2. Experiments and Results

Most of the experiments described here were performed under controlled temperature and humidity conditions. Each die was attached to a 24-pin DIP ceramic package without a lid for environmental testing. The die in this test had a coating deposition scheme termed VSAM (vapor-deposited self-assembled monolayer) that employed supercritical CO_2 drying followed by the chemical vapor deposition of a fluorinated-amino silane precursor. Specifically, for these tests, we used perfluoro-octyltris (dimethylamino) silane, or FOTAS, $C_8F_{13}H_4Si(CH_3CH_3N)_3$ which has been shown to achieve repeatable yield of complex devices through typical packaging processes [2.1].

Controlled environment tubes were designed and fabricated to enable testing in standard ovens. The tubes were constructed from stainless steel ultrahigh vacuum components such as tubes and flanges, in order to facilitate cleaning and minimize sources of contamination. All tubes, frame structures, and screws were subjected to a chemical wash (Brulin detergent clean) to remove any organic contamination prior to package insertion and exposure to temperature. They were then rinsed in deionized water and baked to dry. Each tube has the capability to hold 20 packages. The packages were mounted in a grounded frame as shown in Figure 2.1. The frame, packages, and tube were placed in a controlled environment glove box containing the test environment of interest for a 24-hour period to reach equilibrium. Then the frame was inserted into the tube and sealed while inside the glovebox using the copper gasket and end plate. Oxygen levels were maintained below < 10 ppmv with the desired amount of water vapor and balance nitrogen.

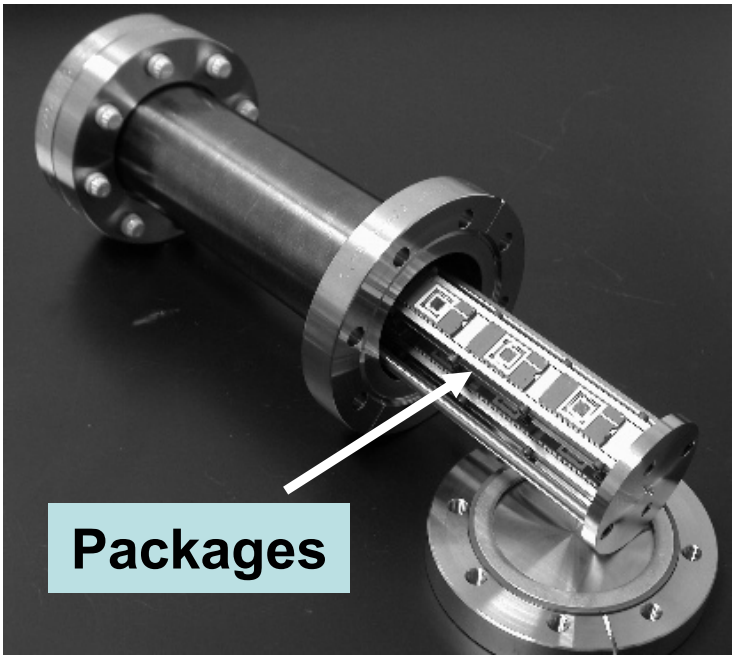

Figure 2.1 Controlled environmental tubes were constructed to define the test environment. The package placement inside the tubes is shown here.

Nitrogen was chosen as a typical package atmosphere. We have chosen accelerated stress temperature levels of 200°C, 250°C, and 300°C which are higher than the standard product operating range of -55°C to +125°C. We also performed one series of experiments at 100°C for comparison. The two humidity levels of 500 and 2000 ppmv H_2O chosen are lower than the military-standard of 5000 ppmv (15.8% RH at 25°C) because of the known sensitivity of MEMS devices to humidity [2.2, 2.3]. Additionally, hermetic packaging processes exist to easily reach the 5000 ppmv H_2O level. We wanted to determine if there is a susceptibility to lower levels of moisture.

For each temperature and humidity level, we tested for at least three time intervals. We used roughly 30 packages for each test to insure a good statistical sample and included a single crystal silicon die in a package to perform surface analysis after the test. A control set of packages was also stored in a dry nitrogen environment throughout the length of the experiments. After the test for the defined time interval, the packages were removed from the environmental tubes and devices were checked for functionality in ambient air. Failed devices were analyzed and functioning devices were censored from further testing. Each time interval has a different set of packages. The overall test plan describing the temperature, proposed humidity level, and duration of the experiment is shown in Table 2-1.

Table 2-1. Test plan for the experiments

Temp (ºC)	Target Humidity Level (ppmv)	Duration (hours)
100	2000	500
100	2000	1000
100	2000	2000
200	500	500
200	500	1000
200	500	2000
200	2000	518
200	2000	1000
200	2000	2000
250	500	500
250	500	1000
250	500	2000
250	2000	200
250	2000	500
250	2000	1000
300	10	2
300	500	50
300	500	100
300	500	200
300	2000	2
300	2000	10
300	2000	24
300	2000	50
ambient	dry nitrogen	Controls

The release, dry, and coat (RDC) process can run roughly 60 die at one time. This is enough to perform two experiments. Therefore, we had to use many RDC requests to provide enough die. One concern was with the reproducibility of the process over multiple runs. In order to monitor the RDC process, we examined VSAM coverage on a bare silicon die that went through the same process as the test die.

2.1 Device Functionality Experiments

The three functioning devices (TRA, DMS, NVM) described in Chapter 1 were tested for functionality before insertion into the environmental tubes. The same devices were tested after the exposure and failures (devices that worked before and not after) were recorded. Due to the amount of handling of the packages, we observed ESD failures and broken devices. These were censored from the test with these known failure mechanisms. Any other failure was typically investigated further and that analysis follows here.

2.1.1 TRA Driving a Load

Susceptible regions of the TRA that are in intimate contact are the hub region of the load gear, the toggle beam on the load gear, the dimples that support the ring gear, and any interaction points of the meshing teeth or ratchet pawls. The gap in the hub was nominally 0.3 μm and was fabricated using the same process described in earlier work investigating wear of contacting surfaces [2.4]. In that work, we observed adhesion in the contacting surfaces, but only after over 100,000 cycles and using a higher force than applied here. These devices are only operated for tens of cycles to check functionality.

Procedure

The TRA driving a load was checked for functionality before the test in an ambient air environment. All the devices, functioning or not, were loaded into the tubes for exposure to the environment. At the end of the time interval, the TRA functionality was tested again and failures were recorded. All of the packages in that time interval (tube) were censored from any further testing.

Results

The raw data from the completed series of experiments is shown in Table 2-2. The censored data column was the number of functioning devices removed from the test at the end of that time interval. The removal of functioning devices necessitated use of the Kaplan-Meier technique for multiply censored interval data [2.5]. The 250ºC data at high humidity is not included because there was an adjustment to an amplifier which increased the voltage on those devices to 50V post-test when they were tested at 42.5V pre-test. The force output is related to the voltage squared so this increased the force by a factor of 1.4. This was probably enough to break through some of the failures and so that data set was not included in the table or any subsequent analysis.

Table 2-2. TRA Failure Data.

Temperature (ºC)	Measured H_2O (ppmv)	Time Interval (hours)	Number Failed	Number Censored	Total on Test
300	2280	2	0	24	24
300	2150	10	7	3	10
300	2150	24	3	6	9
200	2050	518	2	13	15
200	1990	1000	2	15	17
200	1988	2000	2	11	13
300	570	50	4	20	24
300	490	100	3	20	23
300	510	200	6	7	13
250	587	500	4	22	26
250	524	1000	2	21	23
200	480	500	1	23	24
200	470	1000	1	26	27
200	477	2000	2	21	23

Failure data from the upper temperature of 300°C and the two humidity levels is shown in Figure 2.2. We observed a mean time to failure of 26 hours for the 300°C, 2000 ppmv tests and a mean time to failure of 290 hours for the 300°C, 500 ppmv tests. This indicates a strong link to moisture content.

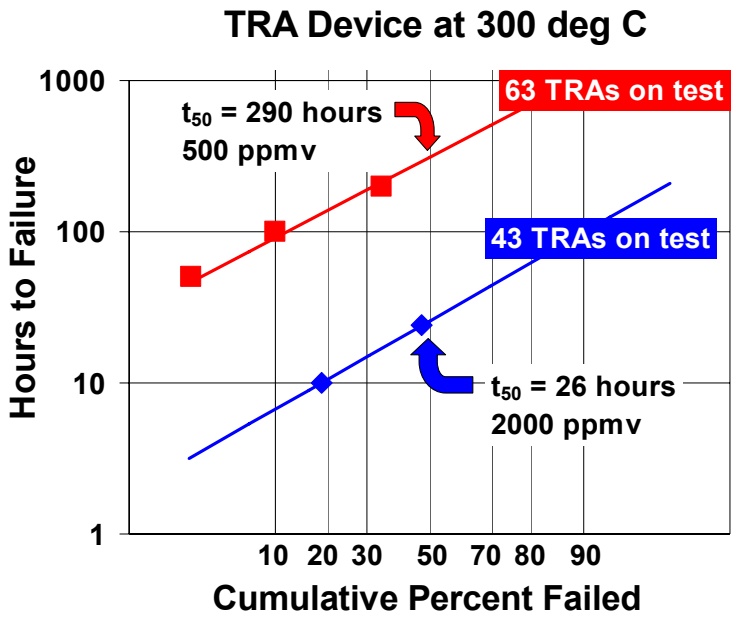

Figure 2.2 Failure data for a TRA device driving a load indicates a definite dependence on humidity.

Each lognormal distribution can be described by the median number of cycles to failure and a slope parameter, σ. The median number of cycles to failure is simply the intersection of the data fit line and the 50% cumulative failed. The slope parameter is the slope of the fit line on a log scale. This slope of the line fit was used to estimate a 90% confidence interval for the median times to failure using the equation:

$$\pm CI = t_{50} 10^{\pm 0.1\sigma/\sqrt{N}} \qquad (2.1)$$

The same technique was used to analyze all of the time interval data from other experiments. The predicted median times to failure and averaged humidity levels are shown in Table 2-3. The slope parameter and number of devices on test are also included.

Table 2-3. Analyzed data from all TRA device experiments.

Temperature (°C)	Average H_2O (ppmv)	t_{50} (hours)	σ	Number on Test	-CI (hours)	+CI (hours)
200	2020	6200	1.2	46	3030	12700
300	2190	26	1.0	43	14	48
200	480	13900	1.3	74	7670	25400
250	550	4090	1.2	49	2100	7970
300	520	290	0.9	63	190	440

The 200°C, low humidity data had time intervals with only 1 failure. Care must be taken in the interpretation of those failures as accidental inclusion of a handling failure would skew the results. We had one case where we observed a failure in the controls due to handling. Figure 2.3 shows the data from all TRA device experiments. The trend to longer life at both lower temperature and lower humidity is apparent. We used this data only to observe trends; there is not enough solid data or understanding of the failure mechanism to begin predictive model development.

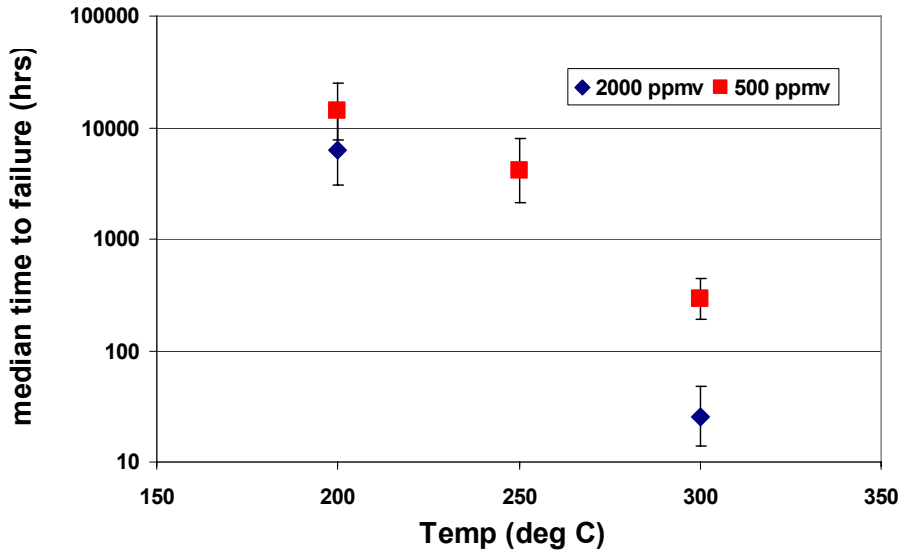

Figure 2.3 The median time to failures from all TRA device experiments is shown here. The error bars are statistical indications of 90% confidence intervals. The trend indicates longer life at lower temperatures and humidity levels.

The majority of these failures were due to an adhesion in the hub region of the load gear. This region has a 0.3-μm gap and in its normal, as-fabricated condition there is expected to be contact between surfaces. More details of the failure analysis can be found in section 2.1.4.

2.1.2 DMS

Areas of concern in the DMS are hub regions in the many gears. There are also dimples under the gears to provide stability which are in contact with the underlying poly surface.

Procedure

The DMS was checked for functionality before the test in an ambient air environment. All the devices, functioning or not, were loaded into the tubes for exposure to the environment. At the end of the time interval, the DMS functionality was tested again and failures were recorded. All of the packages in that time interval (tube) were censored from any further testing.

Results

The raw data from the completed series of DMS device experiments is shown in Table 2-4. The censored data column was the number of functioning devices removed from the test at the end of that time interval. Most of the data at high humidity used the module with a microengine actuator. We observed problems with yield after packaging and large numbers of failures. Analysis of the microengine DMS at 300ºC and humidity level predicted a median lifetime of only 11 hours. The TRA driving a single gear under the same conditions had a predicted lifetime of 26 hours. The decision was made to go to TRA actuation to improve yield. We experienced the same amplifier problem as in the TRA device at 250ºC data and high humidity so it is not included.

Table 2-4. DMS Failure Data.

Temperature (ºC)	Actual H_2O (ppmv)	Time Interval (hours)	Number Failed	Number Censored	Total on Test
300	570	50	11	16	27
300	490	100	15	26	41
300	510	200	8	14	22
250	587	500	2	33	35
250	524	1000	11	34	45
200	480	500	1	29	30
200	470	1000	3	44	47
200	477	2000	2	35	37

We analyzed all of the time interval data from these experiments. The predicted median times to failure and averaged humidity levels are shown in Table 2-5. The slope parameter and number of devices on test are also included.

Table 2-5. Analyzed data from all DMS device experiments.

Temperature (°C)	Average H_2O (ppmv)	t_{50} (hours)	σ	Number on Test	-CI (hours)	+CI (hours)
200	480	11100	1.2	114	7210	17000
250	550	1870	0.6	80	1450	2400
300	520	220	1.0	90	150	320

The DMS data is shown in Figure 2.4 with the TRA data of 500 ppmv. There is surprisingly close resemblance between the two. We expected the DMS to have lower median lifetimes due to the large number of hubs.

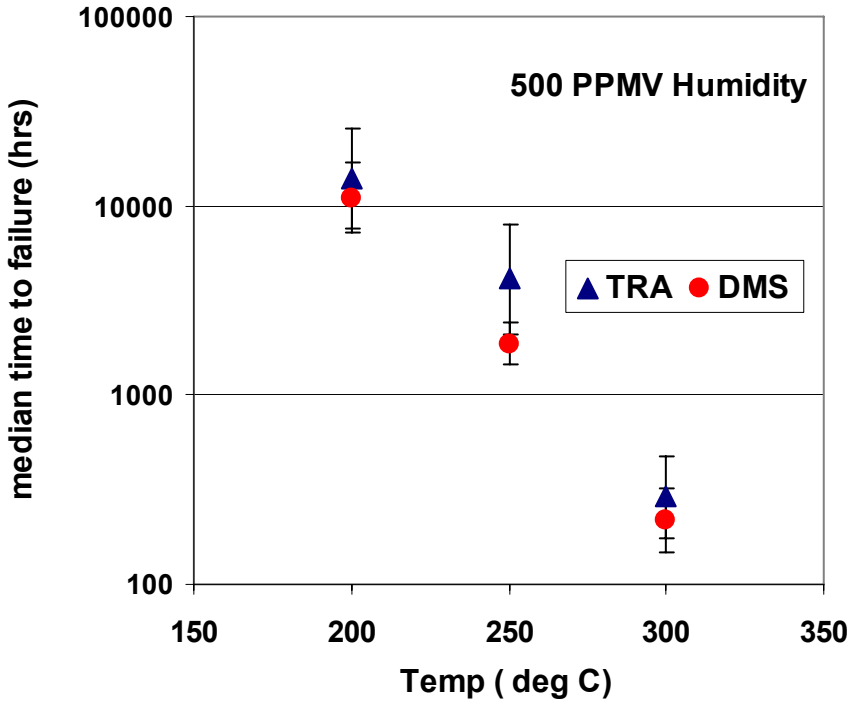

Figure 2.4 The predicted median times to failure for the DMS device are compared to the TRA device.

2.1.3 NVM Single Bit

Areas of concern of the NVM are dimples under the shuttle and springs which could be in contact with the underlying poly surface. A closed switch has latches and switch contacts in intimate contact which may promote adhesion between the surfaces.

Procedure

The NVM was checked for functionality before the test in an ambient air environment. All the devices, functioning or not, were loaded into the tubes for exposure to the environment. At the end of the time interval, the NVM functionality was tested again and failures were recorded. All of the packages in that time interval (tube) were censored from any further testing.

During each time interval, we tested half of the NVM in an unlatched state and the other half in a latched state. In the unlatched state, there are no surfaces in contact. In the latched state, the electrical switch is in contact with a force of 16 μN. In our tests, the switch was not metallized, so the surfaces in contact were polysilicon against polysilicon. In addition, the latches hold the force of the restoring spring which is 27 μN. These forces were calculated based on the nominal geometry and assuming a 0.1 μm edge bias.

This single bit NVM is a very robust design. We latched and unlatched with a minimum voltage of 7.5 V in order to explore small changes in contact force. At this voltage, the thermal actuators output about 200 μN to latch and 240 μN to unlatch. The actuators can survive up to 14 V before deformation of the arms prevents normal motion. In an actual application, one could run with higher voltages and break through most of the contact adhesion we observed in these tests.

Results

The raw data from the completed series of NVM device experiments is shown in Table 2-6. The censored data column was the number of functioning devices removed from the test at the end of that time interval. We upgraded to a more robust design after some of the earlier experiments revealed problems with slight over-voltages. Basically, the thermal actuator legs would deform and sometimes vaporize. The more robust design enabled voltage settings that would actuate the entire population under study. All devices were tested with an input voltage of 7.5 V for both latch and unlatch actuation.

Table 2-6. NVM Failure Data.

Temperature (°C)	Actual H_2O (ppmv)	Time Interval (hours)	Unlatched Number Failed	Unlatched Number Censored	Latched Number Failed	Latched Number Censored	Total on Test
300	570	50	2	38	0	8	48
300	490	100	0	25			25
300	510	200	3	8	5	3	19
300	1960	50	0	7	0	8	15
250	590	500	0	15	2	13	30
250	520	1000	0	13	0	14	27
250	520	2000	0	13	2	11	26
250	2020	200	1	8	0	13	22
250	1980	500	0	8	2	12	22
250	1980	1000	0	13	3	9	25
200	480	500	0	10	1	11	22
200	470	1000	0	9	0	12	21
200	480	2000	0	13	0	15	28
200	1990	2000	0	16	3	10	29
100	2000	2000	0	15	0	15	30
		Totals	6	211	18	154	413

For a functionality test after the environmental stress, we latch and then unlatch the device. The data from the unlatched NVM stressed at temperatures of 250°C and below shows only 1 failure. In that case, the latches stuck during the functionality test, probably due to a change in the surface. A voltage of 7.7V was enough to break the adhesion and unlatch that device.

If we look at the overall numbers of failures, we see that the failure percentage of the unlatched NVMs is 3% and of the latched NVMs is 11% which is almost a four-fold increase. Holding these surfaces together with force definitely promotes failures.

In most cases, the failures were due to an adhesion event. The dominant failure was the inability of the latches to unlatch at the test voltage. In all of these cases, the use of a slightly higher voltage (roughly 10% higher) would shear through the adhesion and continue to latch/unlatch. The second type of failure was adhesion of the switch contact surfaces, which could occur during the environmental stress (for latched devices) or during functional testing after the stress where closing the switch initiated an adhesion event preventing operation. There was one case where the shuttle was stuck and increasing current into the actuator to move the shuttle only deformed the actuator legs.

We analyzed all of the time interval data from the experiments that had failures in at least two time intervals. The predicted median times to failure and averaged humidity levels are shown in Table 2-7. The slope parameter and number of devices on test are also included.

Table 2-7. Analyzed data from all NVM device experiments.

Status under test	Temperature (°C)	Average H_2O (ppmv)	t_{50} (hours)	σ	Number on Test	-CI (hours)	+CI (hours)
Latched	250	550	14900	1.7	42	5450	40700
Latched	250	1990	1950	0.8	39	1210	3160
Unlatched	300	520	590	1.0	76	380	930

2.1.4 Failure Analysis of Devices

Failure analysis has been performed on the MEMS devices tested under different dormancy conditions. These dormancy conditions as stated in the experimental section focused on different parameters to accelerate dormancy-induced failure modes. These parameters included humidity (500 ppmv, 2000 ppmv), time (2 – 2000 hr), and temperature (100^oC – 300^oC). Failure analysis was performed on failed MEMS devices after accelerated dormancy lifetime testing. Results from these analyses have identified a dominant failure mode in the MEMS components. All of these devices have a critical element in common; they contain components in contact during the test. In the case of the DMS and the TRA, the load gears are in contact with the hub during test. When the NVM is in the latched position during test, the latches and contacts are touching.

Results have identified the failure mechanism as adhesion or material bridging contacting components preventing motion. This failure mode was observed in all three MEMS devices, where there were components in contact. Analysis also identified material growth bridging some of the underlying dimples to the ground plane. Reliability testing and analysis indicated several failures during high temperature and high humidity experiments. Failure verification analysis identified an error in the reliability testing protocol and uncovered an amplifier setting of 12.75 instead of the planned 15. This difference in amplifier setting resulted in a lower force output of the electrostatic actuators. We decided to maintain the lower setting because most of the pre-test functionality was determined using this lower setting. The most important comparison is pre to post-test functionality. However, for the thermal actuator, we re-analyzed all failed devices using the higher setting, thus assuring 7.5V on the actuators legs.

After delivering the correct drive signals to the NVM devices, failures were still observed. Initial areas of concern such as the guides and shuttle were inspected. Analysis (not shown) did not identify any foreign material or reliability concerns. Although dimple grooves were observed in the shuttle guides, the guides themselves were cut using a focused ion beam (FIB) to allow the shuttle to move freely in the event adhesion was found along the guide areas (further analysis did not identify any problems with the guides or shuttle). As shown in Figure 2.5a, the SEM micrograph of a failed NVM device after 300^oC for 200 hours shows material bridging the two latch surfaces keeping the device in the contact position. The same device also shows material bridging some of the bottom level dimples to the ground plane (Figure 2.5b-d).

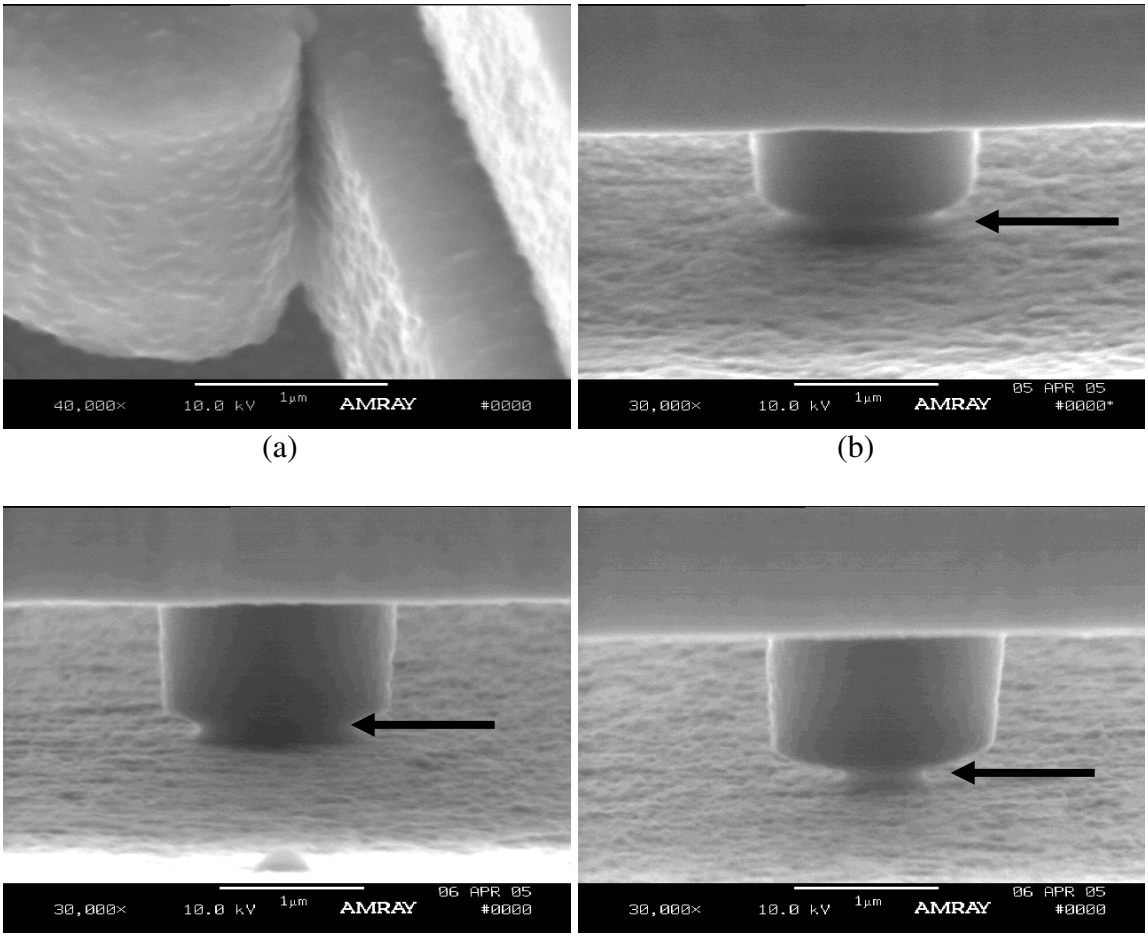

Figure 2.5 Material bridging the contacting region of a latched NVM (a), and foreign material bridging the bottom level dimples to the ground plane (b-d).

This failure mode was identified on various NVM devices tested at 300°C for 10 hours or longer. Other devices such as the TRA and DMS were also affected by this material growth. Analysis of the contacting regions resulted in the presence of foreign material binding critical portions of the device preventing motion. In the case of the TRA, a load gear and toggle switch are present. Analysis of the TRA device identified the ratcheting pawls, anti-reverse pawls, and contacting gear teeth as areas of concern. The load gear and toggle switch had contact areas consisting of the meshed gear teeth, toggle to gear tooth contact, and the load gear to hub (Figure 1.2). SEM analysis of the failed TRAs did not identify foreign material along the contacting regions of the TRA. Analysis identified growth material between the toggle and the load gear tooth shown in Figure 2.6a and 2.6b.

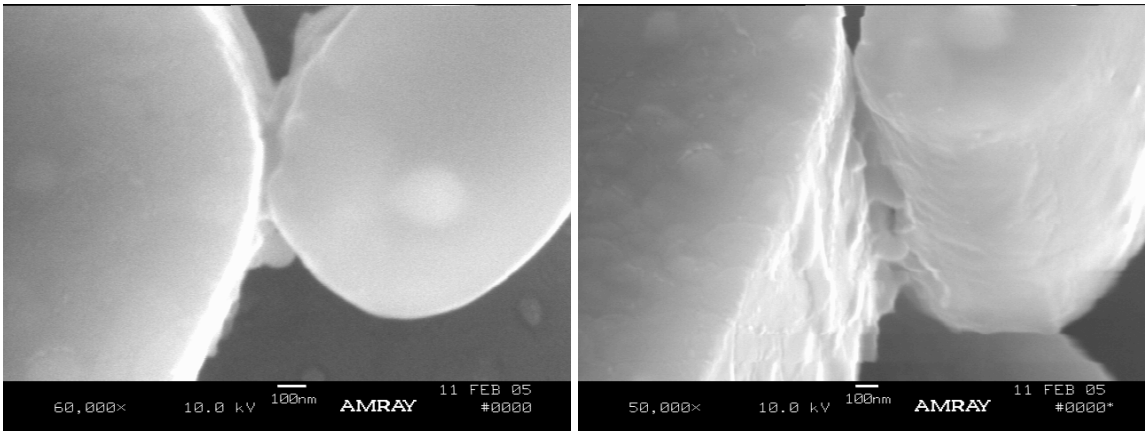

(a) (b)

Figure 2.6 Top down view of material bridging the toggle switch on a TRA (a), and angle view showing the two distinct components "fused" into one component along the contact region (b).

After inspection, the material appears to have the same morphology as the material found in the NVM. However, analysis of the contact area and foreign material showed that the material would amount to less than 1 μm^3, which should not be enough binding material to seize the TRA. After removing the toggle component, the TRA still failed. Further analysis of the load gear using the FIB identified sticking regions between the gear and the hub (Figure 2.7a and 2.7b).

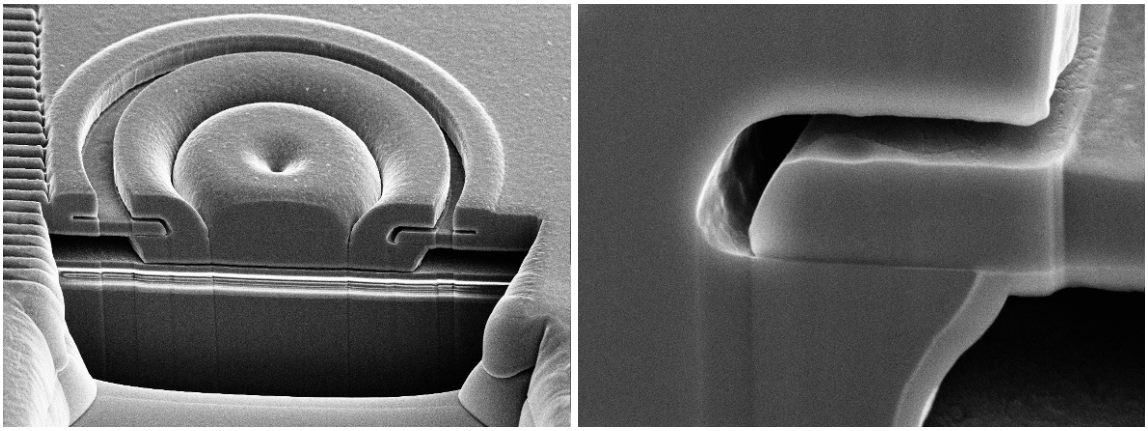

(a) (b)

Figure 2.7 FIB cross-section through a load gear revealing adhesion between the gear and the hub (a), and high magnification image showing the contact/adhesion site between the gear and the hub (b).

After identifying the adhesion/contact region in the hub of the TRA load gear, load gears were removed from the TRAs. Testing of the TRAs after load gear removal revealed the TRAs would function according to their designed specifications. This result clearly indicates the failure mechanism does not reside within the TRA device itself, but the attached load gear and toggle switch.

After finding that the majority of failures in the TRA were the result of adhesion/stiction between the load gear and the hub, it was determined that the DMS component would have a similar failure mechanism especially given the number of gears (5) contained within the gear train. FIB cross sectioning of a gear contained within the gear train of the DMS did reveal sticking along the gear/hub interface. Observing this result in one gear leads us to believe that it may occur in multiple gears.

After identifying the presence of foreign material bridging critical portions of the device, chemical and other structural analysis was needed to determine the material's chemical makeup and understand why it is present. Experimental parameters combined with oxidation modeling data using SUPREM [2.6] determined that the level of oxidation from highly doped polysilicon under these experimental conditions should be ~ 20Å. This result would indicate that silicon oxidation is negligible, and would not be the root cause of the failure.

To perform the chemical analysis, portions of the device were removed to gain access to the adhered spots and materials. The sample preparation varied depending on the structural and chemical analysis techniques used. In the case of transmission electron microscopy (TEM) and energy dispersive x-ray spectroscopy (EDS) of NVM structures, a cross-section was made through the latched components (shown in Figure 2.8a and 2.8b). The resulting TEM cross-section revealed the morphology of the foreign material while the EDX analysis identified the chemical constituents. EDX analysis of these regions identified expected materials such as silicon, oxygen, carbon, copper, and gallium (carbon being ubiquitous, copper x-rays coming from the sample holder, and gallium being an artifact from the FIB sample preparation process).

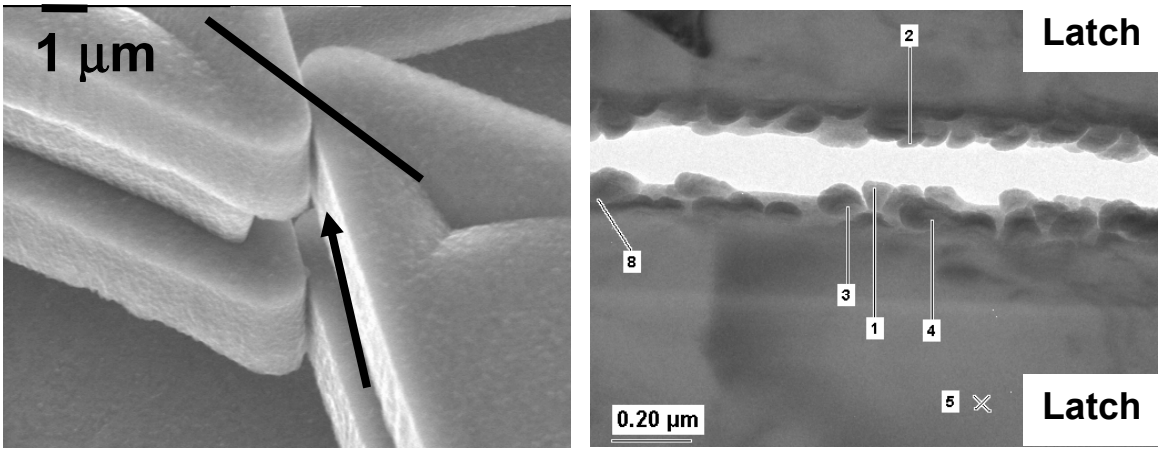

(a) (b)

Figure 2.8 SEM micrograph indicating the location of the TEM cross-section (a), and TEM cross section showing the latch topography. The numbers represent areas where EDX analysis was performed (b).

While x-ray analysis identified the typical elements (C, Si, O), other elements were found on the surface of the contacts that are normally not present. Elements such as Cl, Fe, and Ca were identified in certain areas. The source of these contaminants is unknown, but

their presence will impact the reactivity of the surface changing the rate of oxidation. As shown in Figure 2.9a and 2.9b, EDS analysis performed on spots 3 and 4 show traces of Cl, Fe, Ca and Al. One potential source of contamination may be due to the package fixtures, gas, or tubing used in the dormancy experiment. Other sources may be the equipment used to plasma clean packages, or cure the die attach epoxy. Similar results were observed on a TEM cross section prepared from the other latch region. Small amounts of foreign material that may be undetectable on non-aged parts may migrate to contact locations and collect at touching surfaces, ultimately resulting in bridge formation.

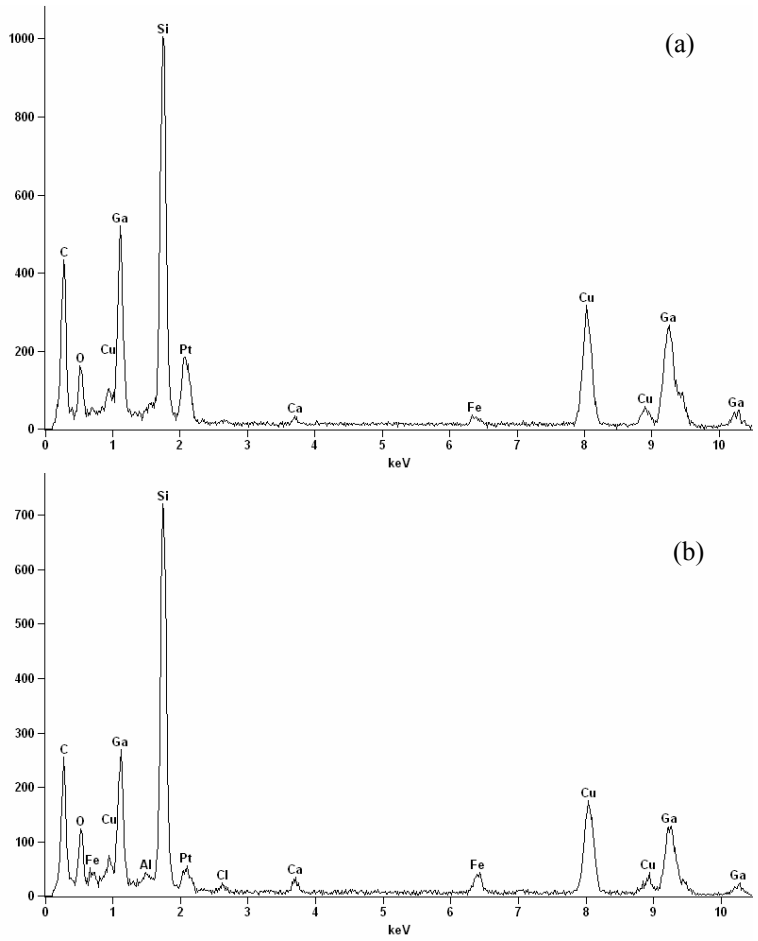

Figure 2.9 EDX spectra resolving iron, calcium, chlorine, and aluminum from spots 3 (a) and 4 (b) of the TEM cross section, respectively.

To confirm the results from x-ray analysis, Auger analysis was performed on a different NVM device from the same experiment. In this case, the latched surfaces were kept in the closed position but were separated to expose the contacting surfaces. Auger analysis was performed along the contact regions as depicted in Figure 2.10a and 2.10b. Analysis was performed along both sets of latches as well as both sides of the latch. Results from these analyses confirmed the presence of contaminants found in the EDS analysis. These

contaminants were found only on one of the latching surfaces. Auger analysis of the other latching surface (Figure 2.10b) did not reveal any contaminants. The numbers on the latch surfaces indicate where Auger analysis was performed. As shown in Figure 2.11a and 2.11b, Auger spectra taken from these regions also identify Ca, Cl, Fe, and Al.

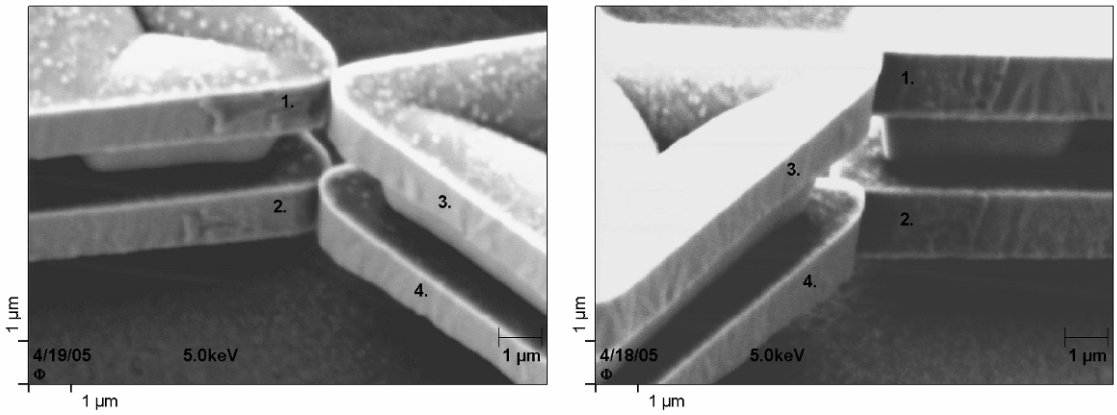

(a) (b)

Figure 2.10 Latching surfaces of an NVM (a, b). The numbers indicate the locations where Auger analysis was performed. No contaminants were identified on b.

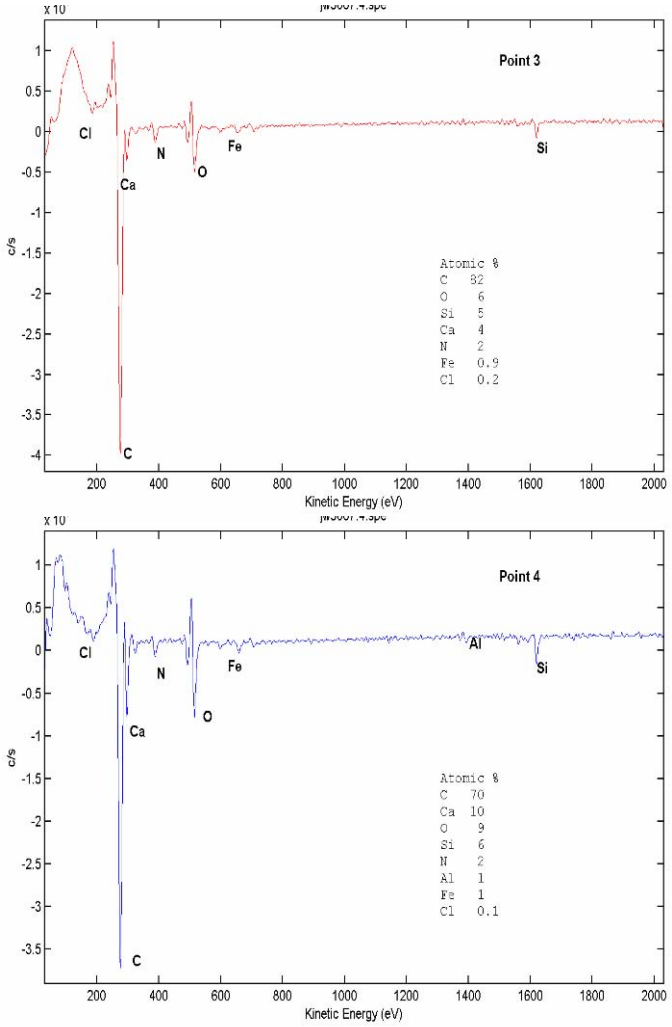

Figure 2.11 Auger spectra confirming the presence of contaminants identified from EDS on Figure 2.10a.

2.1.5 Conclusions from Device Experiments

We have determined that failures in complex MEMS devices can be accelerated using high temperatures and controlled humidity environments. The failures are dependent on both temperature and humidity. The trend indicates longer life at lower temperature and humidity levels.

The failure data show that the most robust devices have actuators that provide enough force to "break through" any adhesion in the contacting surfaces. Figure 2.12 shows that the overall best results are with the NVM which has thermal actuators capable of 200 to 300 µN of force output. The NVM test in the latched state is a much harsher test than the TRA or DMS involving simple hubs of gears. The latch and switch contacts in the NVM are held together with forces of 27 and 16 µN, respectively, while the contact forces in the hub/gear regions of the TRA and DMS are negligible. A poly12 laminate gear of 400 µm diameter has a mass of 700 ng. If the forces in the hub region are only due to gravity, this implies a contact force of 7 nN.

The TRA driving a load or driving the DMS gear train used an electrostatic actuator with about 25 µN of output force. Not shown in the figure was the microengine actuator driving the DMS gear train where experiments at 300°C and 2000 ppmv produced a median time to failure of 11 hours. This actuator has an output force of only 9 µN.

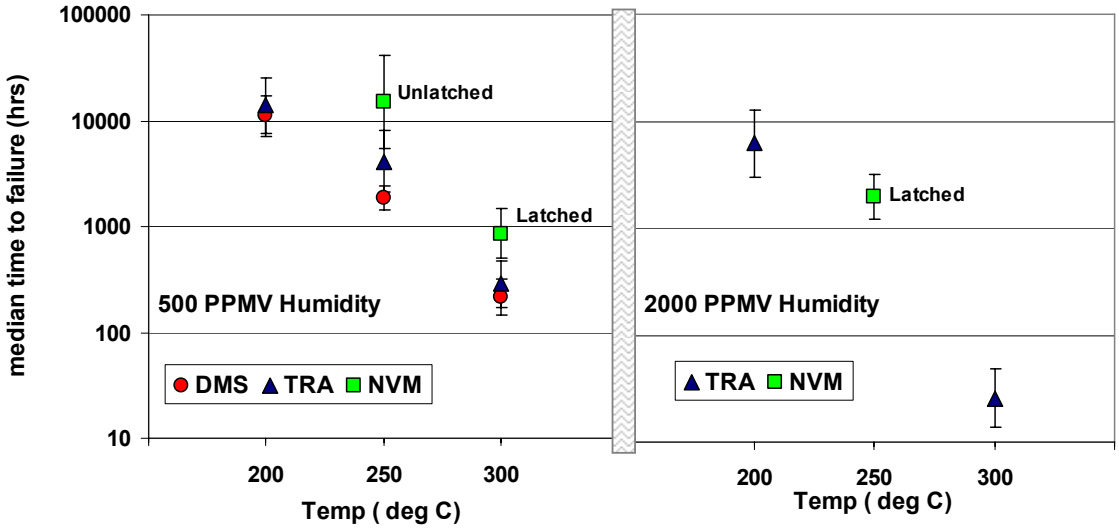

Figure 2.12 Comparison of the median time to failure for the various devices, showing the NVM (either latched or unlatched) as the most reliable device.

We observe a failure of the TRAs due to the environment with most failures occurring at 300°C and some failures at 200°C. These failures are due to an adhesion site in the hub of the load gear where the typical gap is 0.3 µm. There were no failures due to the environmental stress in the TRA or DMS actuator, which is a hub-less device. This actuator employed a large ring gear supported by dimples and was guided by dimples in a groove on the ring gear (Figure 1.2). None of these dimples posed a problem.

2.2 Surface Adhesion Energy Experiments and Results

Surface adhesion energy, Gamma, was measured using the cantilever beam array on at least 15 packages (typically 16 measurements per package) before insertion into the environmental tubes. The same arrays were measured after exposure and the difference in the two measurements was calculated. This difference was attributed to changes on the contacting surfaces due to VSAM degradation.

Procedure

A technique was developed by de Boer and Michalske to measure surface adhesion by using cantilever beam arrays [2.7]. The procedure uses interferometry to measure s-shaped deflections in cantilever beams when they are adhered to the substrate. As shown in Figure 2.13, a beam is pulled into contact with the substrate by applying 90V to the actuation pad near the beam support. When the voltage is released, the restoring force of

the beams and the adhesion of the surface come to equilibrium. The crack length, s, the length from the support post to the point the beam is adhered, was extracted from the measured deflection for each cantilever beam. The adhesion energy, gamma, depends on the inverse of this parameter to the fourth power. The equation used was

$$\Gamma = \frac{3Et^3h^2}{2s^4} \tag{2.2}$$

where the standard value for E, Young's modulus, was 165 GPa [2.8], the thickness, t, was 2.5 μm, and the gap, h, was 1.8 μm.

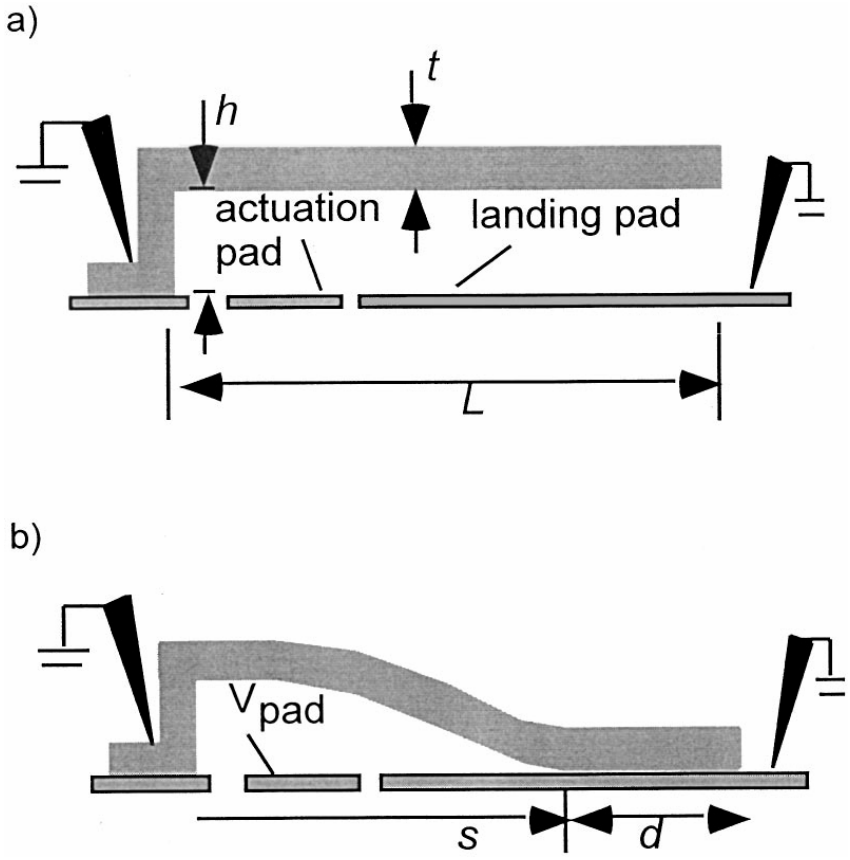

Figure 2.13 Schematic illustration of the approach for measuring the surface adhesion between silicon surfaces showing a) the basic free-standing beam with appropriate parameters and b) the adhered beam after it was pulled into contact by applying and then removing a voltage with the voltage, V_{pad}.

Results

We have characterized the adhesion energy of the surfaces of control die and test specimens using cantilever beam arrays. In early experiments, we simply compared control die to post-test die as shown in Figure 2.14. The control die which were kept in a dry nitrogen environment with no temperature stress was compared to a die that was

tested at 300°C for 50 hours with a humidity level of 572 ppmv. The fringes indicate deflections of the beam; sections of no fringes indicated adhered beams. The measured crack length of 870 μm for this particular control was used to calculate a surface adhesion of 14 $\mu J/m^2$ using Equation 2.1. The exposed specimen had a crack length of 470 μm which equates to 260 $\mu J/m^2$ of surface adhesion. Control beam arrays that were stored in a dry nitrogen environment during the test showed virtually no change in the adhesion energy over longer time intervals.

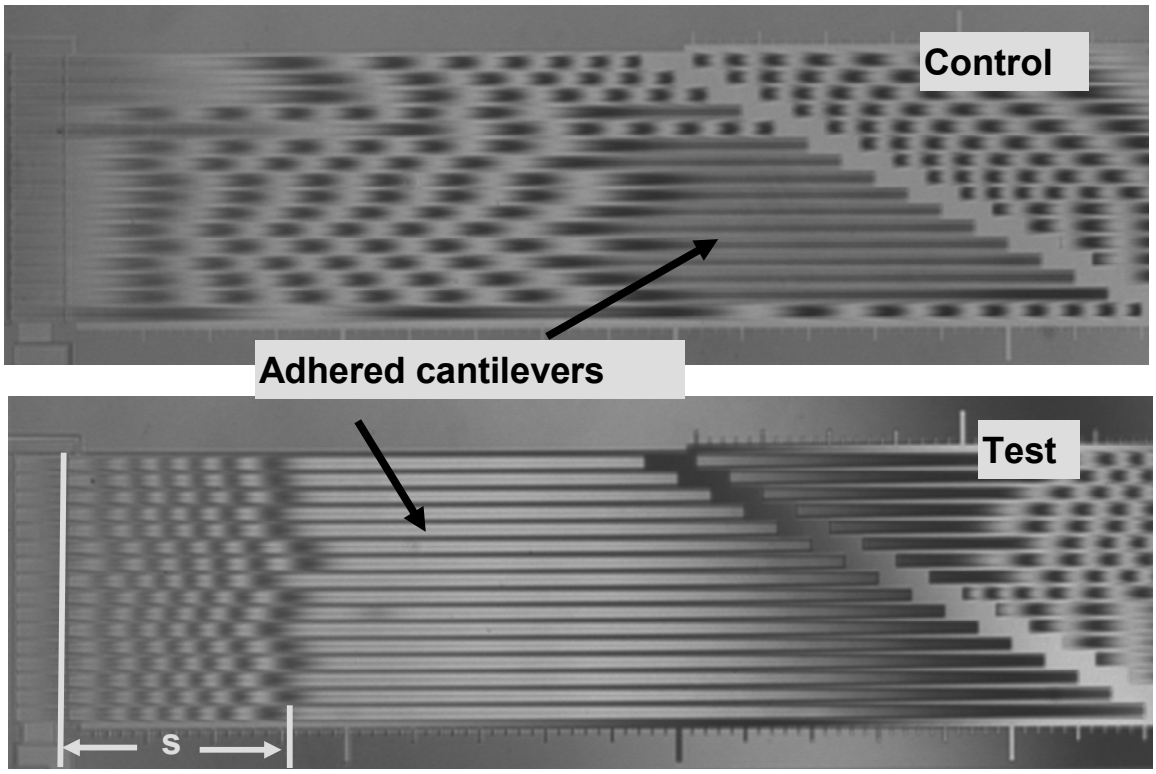

Figure 2.14 Interferograms of cantilever beam arrays showing beams that are adhered to the substrate. The crack length, *s*, shown on the test beams was extracted from the measured deflection for each beam.

In order to discern changes more accurately, for later experiments, we decided to measure the same beams both pre-test and post-test. For example, we used an actuation voltage to force the beams into contact with the substrate ("zip" the beams), released the voltage, and measured adhesion. These beams were then exposed to the environments in their 'zipped' equilibrium state. The advantage of this method is that we then investigate the very same beams after test so that we have a clear before and after description of the surface adhesion.

To get a clear picture of the surface adhesion before exposure to environments, we analyzed the beams from many of the release requests. Each request had an identifying number (RID) and was composed of about 60 die. Measurements made on 30 packages

are shown in Figure 2.15. Each data point represents the average of roughly 100 individual beams. These results indicate that the VSAM process is relatively stable with average surface adhesion energy of 13 ± 4 μJ/m^2 before any exposures.

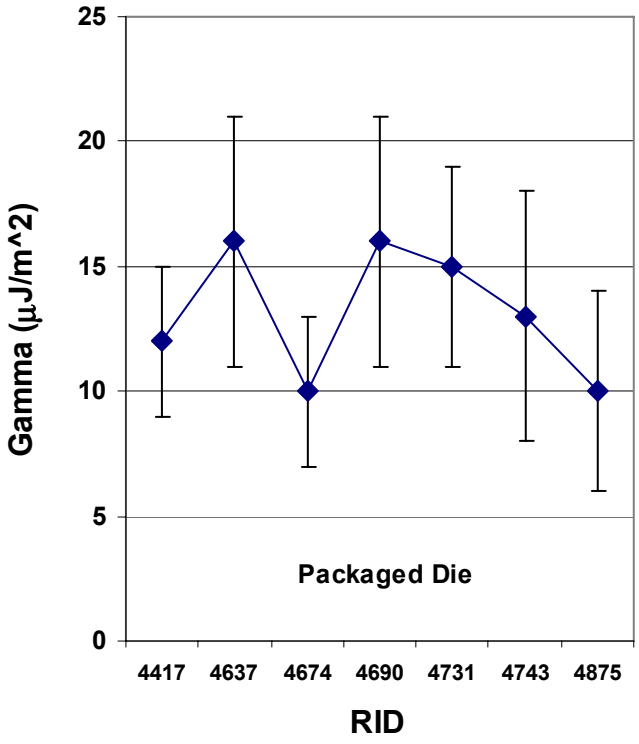

Figure 2.15 The initial surface adhesion energy measurements show a stable process averaging 13 μJ/m^2.

One of the interesting observations was that there is package dependence in the data as shown in Figure 2.16. The crack length data are shown for each independent beam in the array, both pre- and post-test. Each data point was used to calculate adhesion energy and the adhesion energy change between pre and post was determined. Although all of the die were released in the same batch, packaged at the same time, and had similar pre adhesion measurements, we observed differences in the adhesion energy change as shown in Figure 2.17.

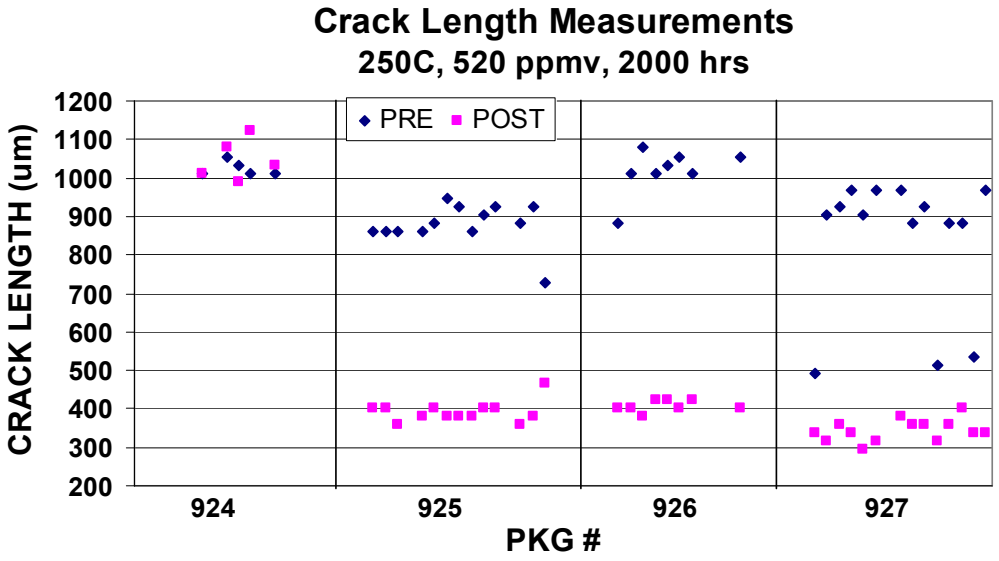

Figure 2.16 Package dependence of pre- and post- crack length data for four packages subjected to the same environmental stress. There was virtually no change in package 924, but large changes were noted in the other three packages.

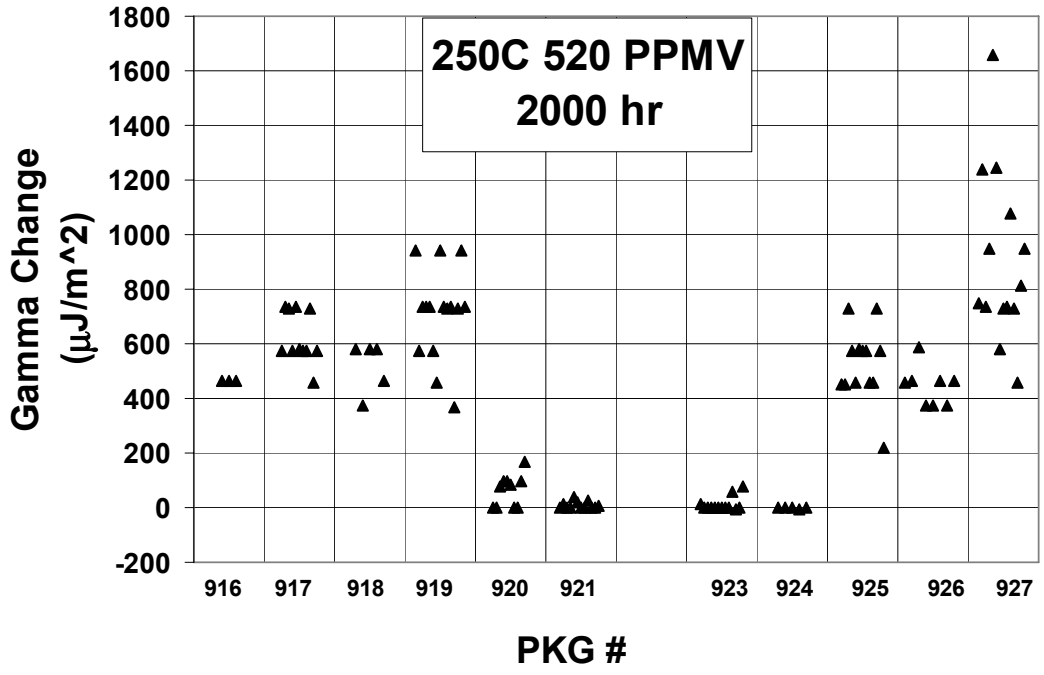

Figure 2.17 Adhesion energy change in the cantilever beam arrays, sorted by package number.

To investigate the differences in the packages, we took packages 924 (0 adhesion change) and 927 (900 $\mu J/m^2$ adhesion change) and performed surface characterization under the cantilevers. We chose the area under the longest cantilever beam and about 20 μm from the beam tip. A 5 x 5 μm^2 – area was scanned in an Atomic Force Microscope (AFM) at four random locations. The scans are shown in Figure 2.18, where the scan on the left is from package 924 and the scan on the right is from package 927. The major difference is the density of 50-nm particles (seen as the white spots). These small particles under the beams are large enough to prevent pull down, thus interfering with the surface adhesion measurement. The particles were introduced at some point in the release chemistry, were not consistent from die to die, and are not identified at this point.

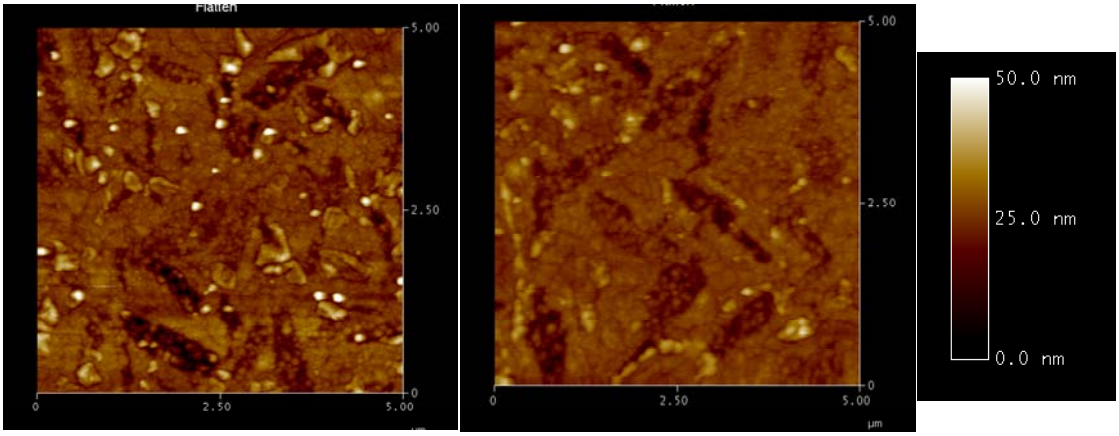

Figure 2.18 AFM scans under the cantilever beams from package 924 (left) and package 927 (right) show the presence of 50-nm particles. The particle density is higher under the beams that measured no adhesion change.

To analyze the data, we sorted it into bins of adhesion energy change. This enabled identification of one or more distributions of data. For the case of the 250°C, 520 ppmv, and 2000 hour data, there were two distributions which were fit to a Normal Distribution to get the average and standard deviation. The data and the normal distribution fit are shown in Figure 2.19.

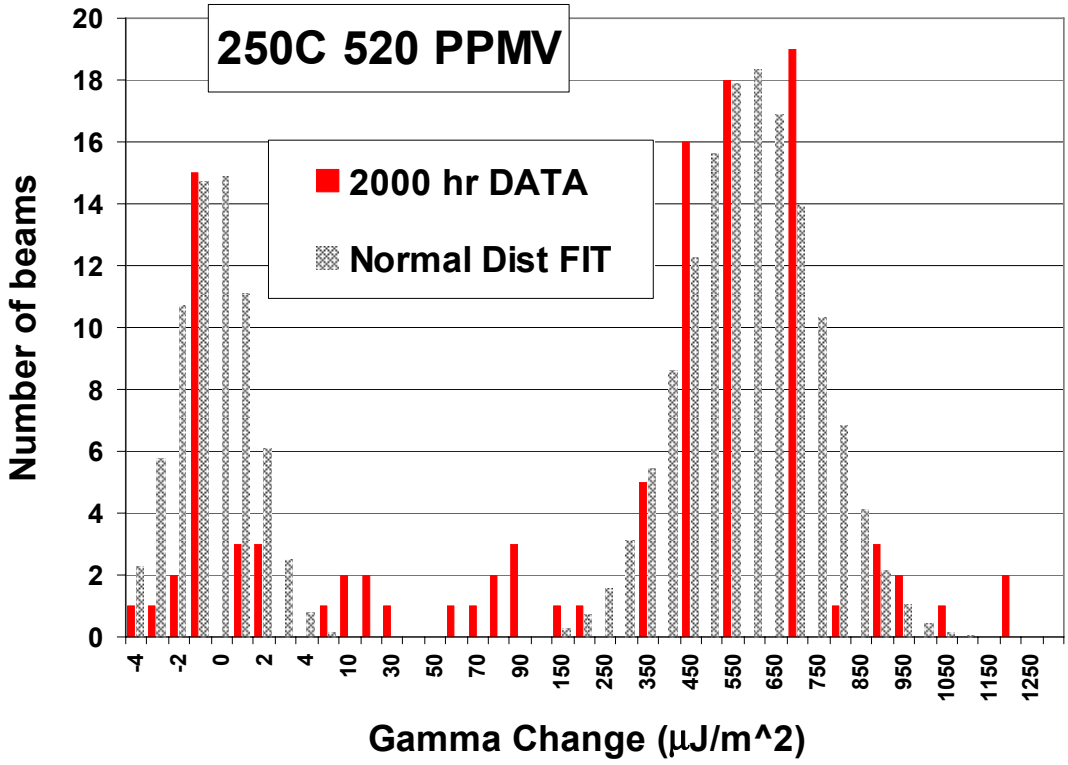

Figure 2.19 Analysis of the adhesion energy, Gamma, change as a result of the stress required sorting the data to determine groups.

The same procedure was followed for all of the experiments and the results were tabulated below. In Table 2-8, the actual humidity sealed in the tubes is listed. The Gamma Change was the average and sigma was the standard deviation of the normal distribution fit to the data. N is the number of measurements in the fit. In most cases there are more than one distribution (grouping) of data. Overall, this data is the compilation of 1562 individual measurements. There were 326 control beams which were stored in a nitrogen-filled dry box. The control data was sorted in the same manner, which revealed a Gamma Change of -1 ± 3 $\mu J/m^2$ which we view as the baseline of zero change.

Table 2-8. Gamma change measured for the cantilever beam arrays.

Temp (°C)	H_2O (ppmv)	Interval (hrs)	Gamma Change (uJ/m^2)	sigma	N
300	2280	2	0.1	2.5	19
300	2150	10	1140	780	59
300	2150	10	4700	100	14
300	2150	24	1750	670	42
300	2150	24	4700	200	4
300	1964	50	85	51	87
300	1964	50	870	370	20
300	1964	50	3300	870	37
300	572	50	-2	2	45
300	572	50	10	3	13
300	488	100	1560	510	68
300	508	200	670	250	32
300	508	200	18000	1000	22
250	2016	200	-3	3	13
250	1984	500	-1	2	40
250	1980	1000	125	58	33
250	1980	1000	500	127	32
250	587	500	-1	2	65
250	587	500	8	3	63
250	524	1000	-1	3	86
250	524	1000	17	9	46
250	520	2000	-1	2	26
250	520	2000	586	152	64
200	2000	1000	3	5	29
200	2000	2000	-0.33	2	24
200	2000	2000	13	7	12
200	500	500	-2	3	51
200	500	1000	1	3	9
100	2000	500	0	3	96
100	2000	2000	0.3	3	85
Ambient	<10	Controls	-1	3	326

We can eliminate the distributions with zero change by assuming that the high particle density was affecting those measurements. Furthermore, we can refine the data by making an assumption that the groups of values with the highest Gamma change (minimum particle density) in a time interval are more representative of the surfaces in the hubs. In this case, the data is shown in Figure 2.20. The data is plotted on a log-log scale simply to observe all the data, not to suggest any functional dependence.

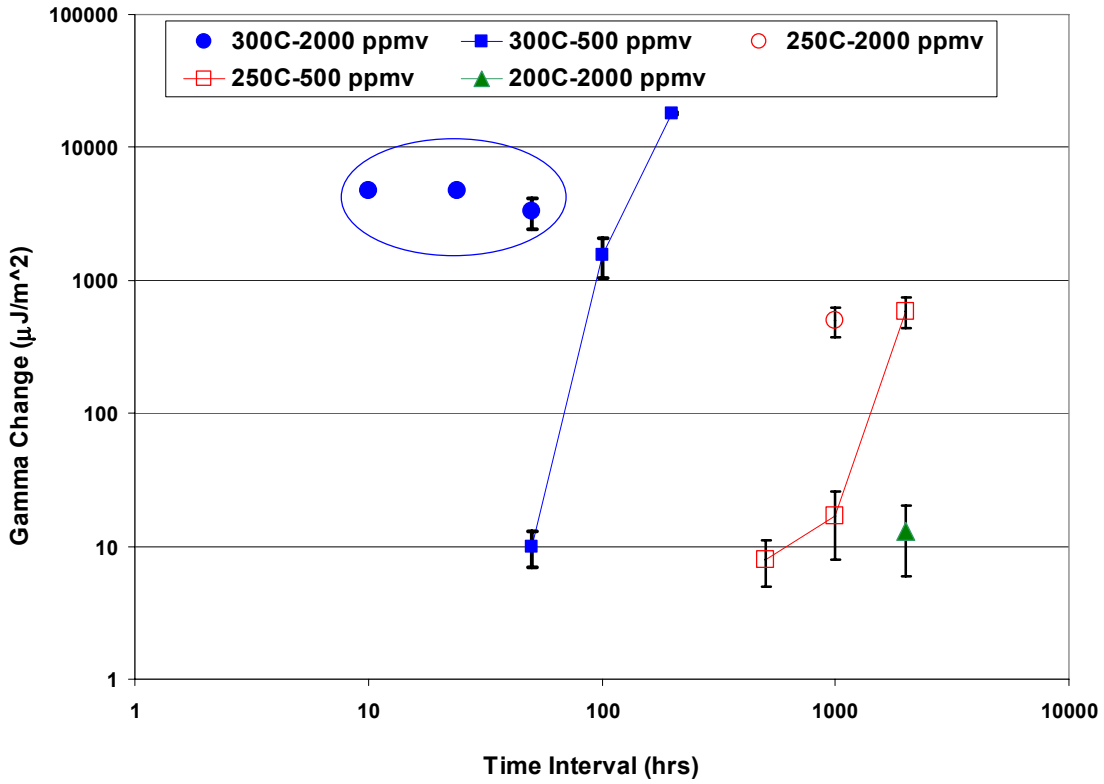

Figure 2.20 CBA surface adhesion change data showing a humidity and temperatue dependance.

The trend toward lower Gamma Change as the temperature and humidity are lowered is seen in the figure. Certainly at 300°C and 2000 ppmv humidity, the data appears to have no time dependence. In this case, after 10 hours the damage is done. However, for the 300°C and 500 ppmv humidity case there is time dependence. Unfortunately, for the 250°C-2000 ppmv case, we only got data for one time interval. It did yield a higher Gamma Change than the lower humidity case. The data for the 250°C-500 ppmv case also shows time dependence.

Conclusions

We have shown that there are measurable changes in surface adhesion energy using these cantilever beam test structures. There is an influence from humidity where a higher humidity at the same temperature will cause more adhesion change. There is also an influence from temperature where higher temperatures produce larger changes in adhesion.

All of our measurements reveal degradation of the VSAM surface coating when stressed at high temperatures with controlled humidity. In particular, we have seen the surface adhesion change for experiments stressed at 300°C for time intervals of 10, 24, 50, 100, and 200 hours. But there is no measurable change at 2 hours. A factor of four increase in humidity promotes the same change in a factor of ten less time.

2.3 VSAM Coverage Experiments and Results

2.3.1 Technique

Procedure

Time-of-Flight Secondary Ion Mass Spectrometry (ToF-SIMS) is a highly surface sensitive analytical technique. It has high spatial resolution (200 nm) and high chemical selectivity. This technique can provide a detailed chemical inventory of a surface to which it is applied. For these reasons, ToF-SIMS is used to analyze the coverage of VSAM molecules on silicon devices.

At Sandia National Laboratories, a suite of multivariate tools has been developed. AXSIA (Automated eXpert Spectral Image Analysis) contains powerful tools for interrogating large datasets. The multivariate methods used in the toolkit are ideal for the signals generated in ToF-SIMS. We have used AXSIA to evaluate VSAM coverage on MEMS structures.

Results

A typical positive secondary ion mass spectrum of FOTAS on polySi-0 acquired using ToF-SIMS is shown in Figure 2.21. In this spectrum, fragments originating from the perfluorocarbon pendant chain dominate the spectrum. Additionally, SiF^+ is a peak resulting from the fragmentation of the VSAM and the activation of the silicon surface. This peak is the most intense fragment of the VSAM molecule. It also shows the most linear response with VSAM coverage. Therefore this peak is used to quantify the coverage of VSAM on silicon surfaces.

The coverage of the VSAM is related to SiF^+ as measured by ToF-SIMS according to the plot in Figure 2.22. Conditions used in this quantification are based on measurements of varying VSAM concentration on Poly0-Si. ToF-SIMS measurements were calibrated using X-ray Photoelectron Spectroscopy (XPS). In ToF-SIMS, a 25kV $^{69}Ga^+$ primary ion beam is rastered over a 65x65 μm^2 area for 5 minutes while positive secondary ions are acquired. From the resulting integral mass spectrum, the SiF^+ peak is ratioed to the Si^+ substrate peak to remove instrument variations. This number is then used in the quantification equation in Figure 2.22. The error as measured by the standard deviation of the calibration curve is $0.1x10^{14}$ molecules/cm^2. A detailed description of this quantification process has been submitted to Applied Surface Science for publication.

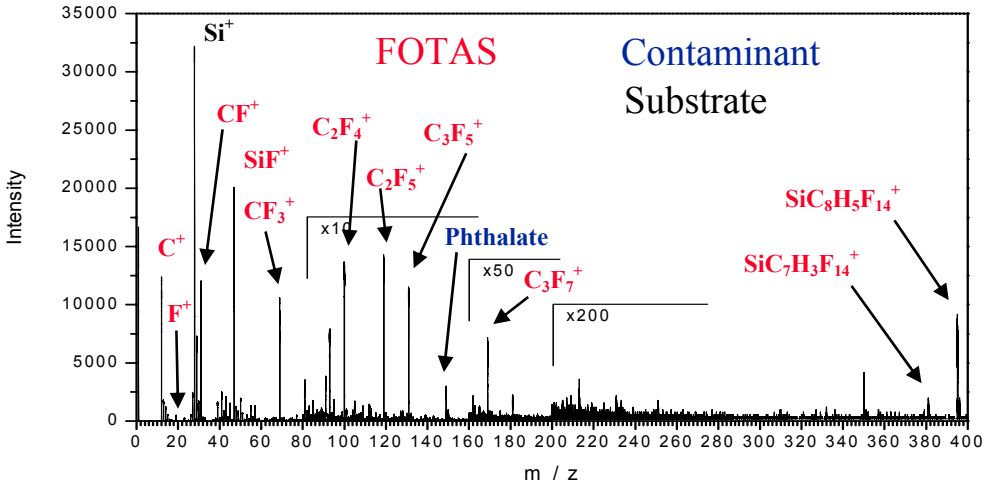

Figure 2.21 Typical positive secondary ion mass spectrum from ToF-SIMS. Note the major peaks associated with the VSAM (FOTAS) are in red, while contaminants and sustrate peaks are labeld in blue and black respectively.

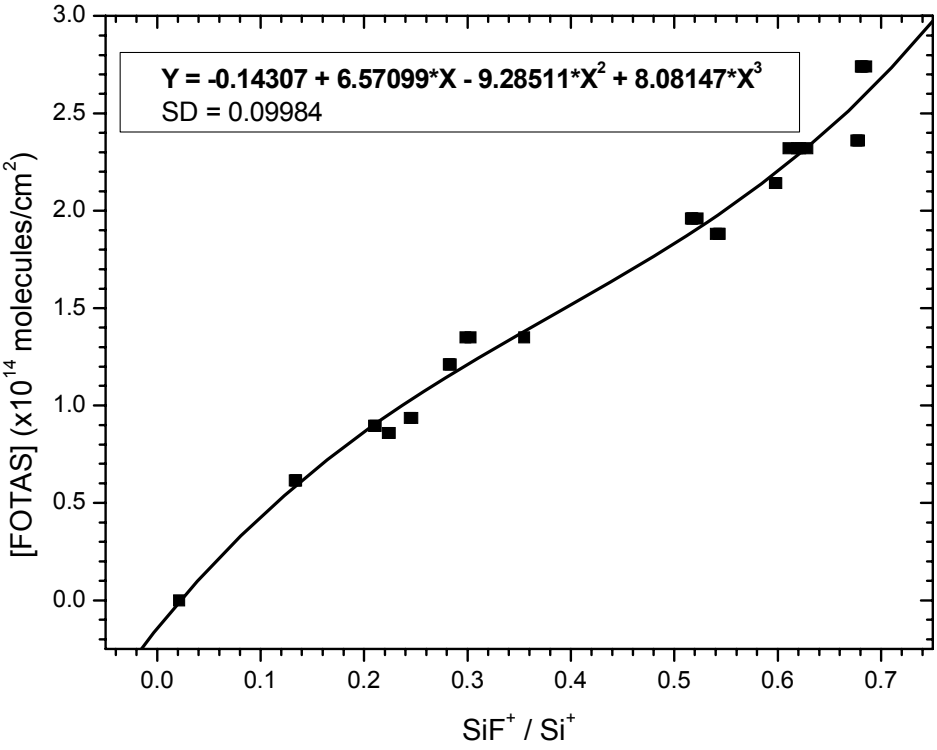

Figure 2.22 Calibration curve for the coverage of the FOTAS VSAM when measured using ToF-SIMS. The SiF^+ fragment is ratioed to Si^+ to account for instrument variations. Note that the error is +/- $0.1x10^{14}$ molecules/cm^2 in this calculation.

Conclusions

We have developed a method to quantify VSAM coverage on polySi devices using ToF-SIMS. This method can been used to quantify the coverage of VSAM both on large area coupons and device-level surfaces. In the following sections, coverage measurements are made on coupons as a function of processing. In addition, device-level measurements are made on custom structures specifically designed to test VSAM deposition in occluded areas.

2.3.2 Packaged Die

In most of the release requests for die, four bare silicon dice were included in the RDC process. Three of these dice also went through the packaging process of die attach cure. One of the die remained in the gel pack in the dry box for the entire experiment as a control. One packaged dice remained in the dry box as a control. The other two packaged die were placed in the controlled environment tubes and run on the test along with packaged die containing devices.

Procedure

Data were acquired using a Physical Electronics TRIFT I Time-of-Flight Secondary Ion Mass Spectrometer (ToF-SIMS) system. Spectral images were acquired in positive secondary ion mode using a 25 kV, 200 nm-sized, 600 pA, ^{69}Ga static beam rastered over a 65 x 65 μm^2 analysis region. Raw files were stored during each 5 minute acquisition with no charge compensation methods employed. The data contained in each raw file were binned to 256x256 pixel images with spectra ranging from 0-400 amu at 1-amu bins. The spectral images were concatenated together to form a spectral image montage. The resulting spectral image montage was processed using Sandia National Laboratories' multivariate analysis program, AXSIA (Automated eXpert Spectral Image Analysis) [2.9].

Results

We used the above procedure to measure the FOTAS coverage from the samples. There was slight degradation in this coating due to the packaging process as shown in Figure 2.23. The packaging process includes a die attach and cure at elevated temperature. Each measurement has a standard deviation of 0.092 x 10^{14} molecules/cm^2 shown as the upper and lower error bars in the graph.

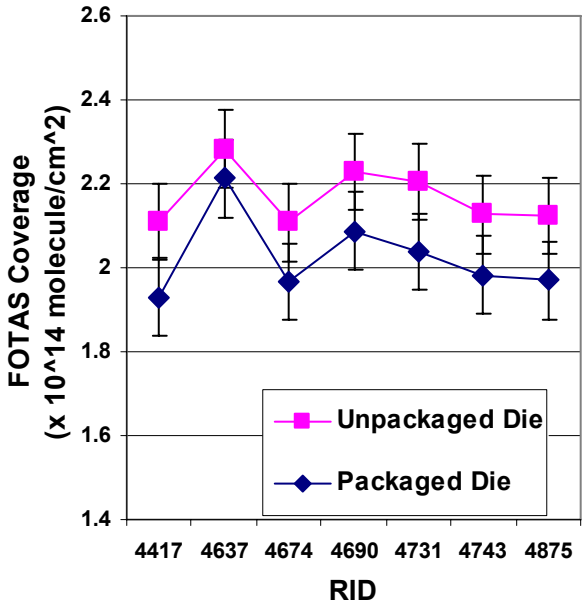

Figure 2.23 The FOTAS coverage is shown as a function of the Release Identification number, RID, for an unpackaged die and a packaged die. This graph demonstrates that coverage in each release varies and that packaging affects the VSAM.

The bare silicon die in packages were placed in the environmental tubes along with the experimental packages. After the experiment, the VSAM coverage was measured and in most cases was degraded. The data are shown in Figure 2.24 which used a normalized value of coverage instead of absolute to factor out the release variations. Each measured FOTAS coverage after the environmental exposure was divided by the measured unpackaged die coverage from the same RID. From the plots, we observe that 300ºC is very harsh, reducing the FOTAS coverage dramatically. The 100ºC data is quite the opposite, showing no degradation. The 200ºC data shows more degradation with higher humidity than lower humidity which is what we expected after looking at device functionality in Section 2.1. However, comparing the 250ºC data at the two different humidity levels (as in Figure 2.25) is quite puzzling. One would expect that if humidity was contributing to the degradation, then the higher humidity case would degrade the FOTAS more. But at 1000 hours, the higher humidity case degrades less. Exponential fits to the data intersect rather than remain parallel. This might indicate a mechanism change.

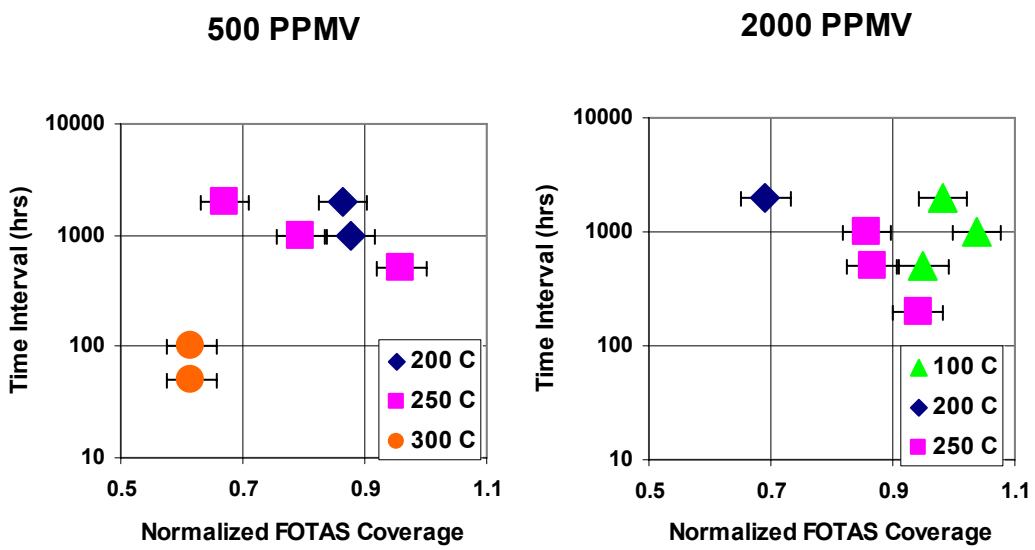

Figure 2.24 The normalized FOTAS coverage after exposure depends on temperature, humidity, and time of exposure.

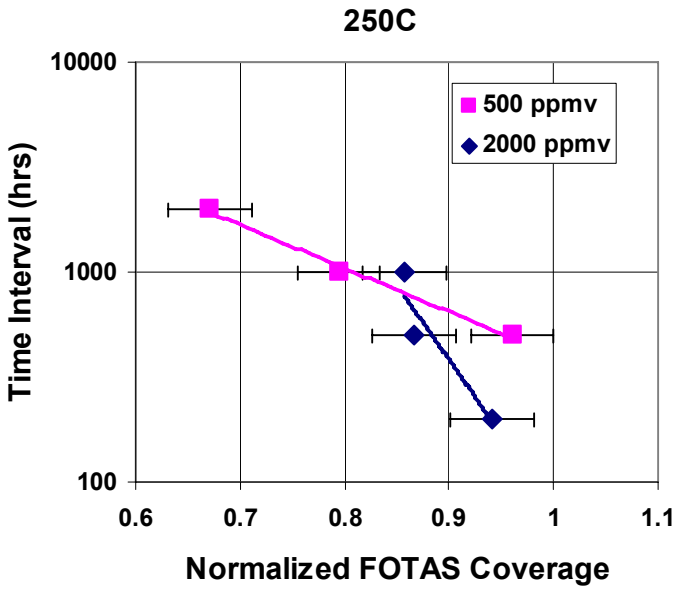

Figure 2.25 The normalized FOTAS coverage for the 250°C case shows fit lines intersecting instead of the expected parallel behavior.

This FOTAS degradation was probably the cause of the surface adhesion changes shown in Section 2.2. The functional dependence is not the same, but the trends show agreement as shown in Figure 2.26 for beams stressed at 250ºC in a 500 ppmv environment.

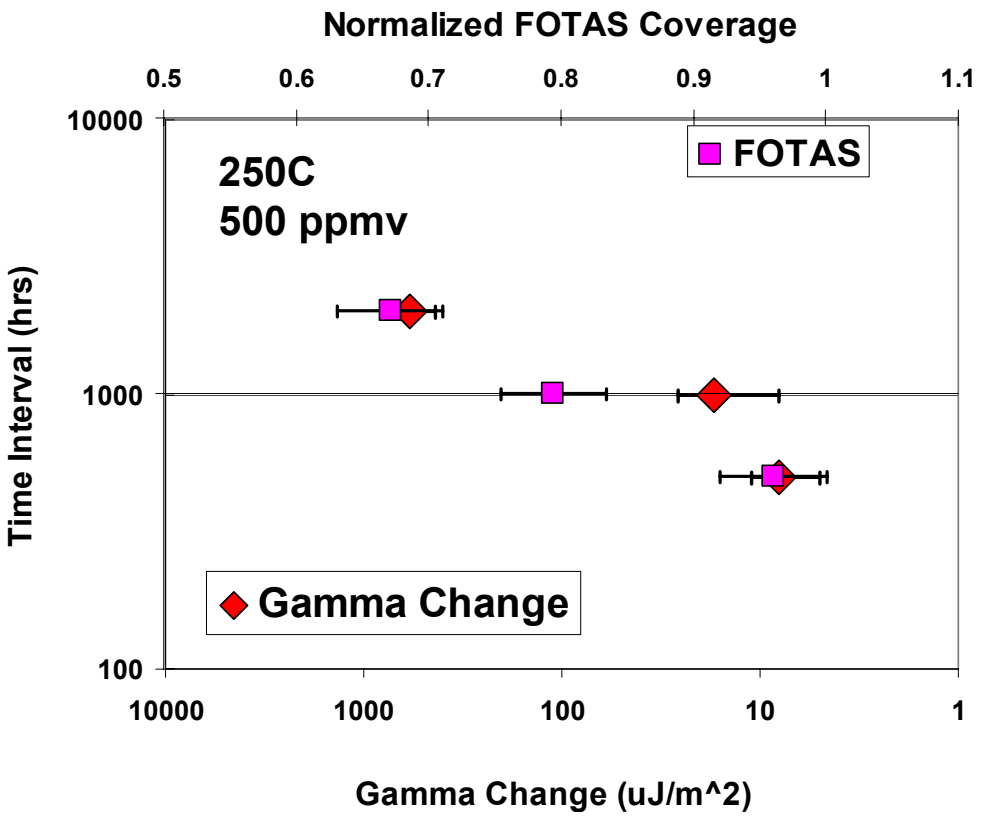

Figure 2.26 Comparison of the FOTAS coverage degradation at 250°C and 500 ppmv to the Gamma Change measured in the cantilever beam array shows agreement in the time dependence of both effects.

Conclusions

There is a measurable degradation in the coverage of the FOTAS as a result of the exposure to high temperature and two humidity levels in nitrogen gas. The most degradation came from a temperature of 300ºC. No degradation was measured at a temperature of 100ºC. We believe that this degradation in VSAM coverage caused the measured changes in surface adhesion.

2.3.3 Thermal and Hydrolytic Stability of Monolayers

Procedure

Previous research has demonstrated the susceptibility of monolayer surface treatments for MEMS, particularly silanes, to hydrolysis in the presence of water vapor [2.10, 2.11]. This is particularly true for non-fluorinated silanes. Process control is difficult when using alkylsilane molecules since they can react with physisorbed water as easily as hydroxyl sites on the oxidized silicon surface, such that any variation in the surface hydroxylation or amount of adsorbed water results in variation in the coating. Adsorbed water is extremely difficult to control, and even trace amounts of dissolved water (ppm levels) in “anhydrous” solvents can lead to variability in the process.

Process variability in liquid-deposited alkylsilanes was the primary motivation for investigation of alternate surface treatment processes for MEMS at Sandia National Laboratories, eventually leading to the development of the VSAM process and selection of the FOTAS molecule as the monolayer precursor [2.12, 2.13]. As shown in Figure 2.27, alkylsilanes require excess water to hydrolyze the chlorinated head group, and then application of heat and removal of water to bond the molecule to the surface via a siloxane linkage. The vapor-deposited aminosilane reacts directly with surface hydroxyls, and the reaction is sufficiently energetic that it proceeds at room temperature without added heat.

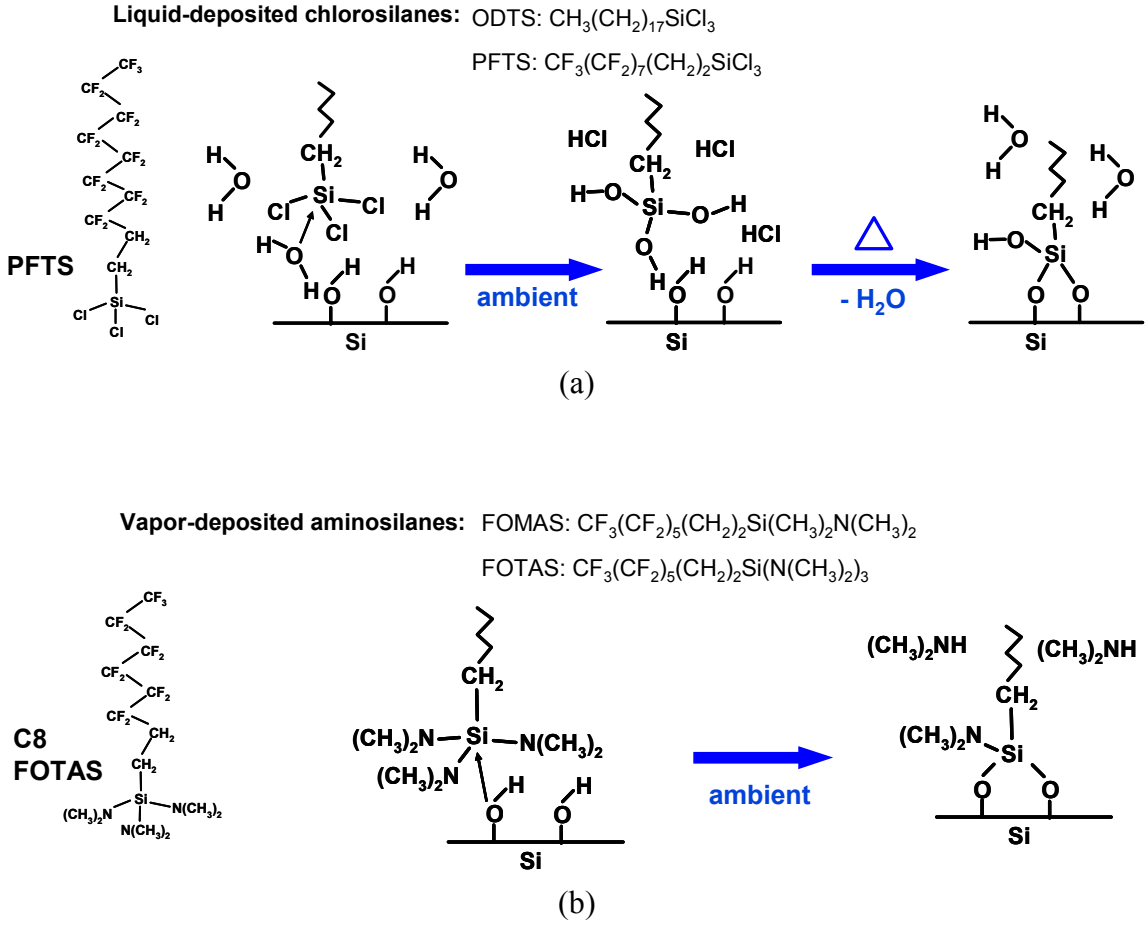

Figure 2.27 Illustration of the assembly process for liquid-deposited alkylsilanes (a) and vapor-deposited aminosilanes (b) on oxidized silicon surfaces.

Once the aminosilane is bonded to the surface, a siloxane bond is formed that still may be susceptible to hydrolysis in the presence of water vapor. Early in the project, the hydrolytic and thermal stability of FOTAS was examined relative to other molecules which have been used to modify the surface chemistry of MEMS devices.

Four different surface treatments were examined as part of this study. The alkylsilanes octadecyltrichlorosilane, $CH_3(CH_2)_{17}SiCl_3$ (ODTS) and perfluorodecyltrichlorosilane, $CF_3(CF_2)_7(CH_2)_2SiCl_3$ (PFTS) were deposited from organic solvents in solution as described elsewhere [2.11]. Briefly, this consisted of release etch, solvent exchange to an organic solvent containing 1 mM of the silane molecule in solution, then submersion in the same sequence of solvent in reverse order until the devices are submerged in DI water. The devices are then pulled from DI water and allowed to dry. The aminosilanes tridecafluorotri(dimethylamino)silane, $C_8F_{13}H_4Si(C_2H_6N)_3$ (C8 FOTAS) and tridecafluoromono(dimethylamino)silane, $C_8F_{13}H_4Si(C_2H_6N)$ (C8 FOMAS) were deposited from the vapor phase. Briefly, this consists of release etch, supercritical CO_2 extraction of the solvent, plasma cleaning, and dosing with the precursor molecule in a vacuum chamber. The process is described in more detail by Mayer [2.12]. The FOTAS molecule was deposited using the tool and process used to treat other MEMS die with hydrophobic coatings.

Sections of Si(100) were coated with these monolayers and then subjected to a variety of exposures to both mimic a typical packaging operation and to examine hydrolysis of the molecules in an aggressive water vapor environment. The samples were divided into four groups, whose exposure conditions are detailed in Table 2-9.

Table 2-9. Sample Groups and Exposure Conditions

Group Designation	Exposure
0	Control; stored in dry N_2
1	150°C, 30 min. air oven (simulates die attach epoxy cure)
2	Group 1 + 2 hr vacuum bake, 150 °C (simulates degassing; ~ 3 mTorr)
3	Group 2 + 50 min. through belt furnace, 320°C peak temperature (simulates lid seal)
4	310°C, 105 min, 24625 ppm H_2O in N_2 (88% RH)

After exposure, water contact angle and surface composition were measured. The quantitative technique for FOTAS measurement on MEMS die using ToF-SIMS had not yet been developed at the time of this experiment, so XPS was used to quantify the atomic concentrations and bonding of F, O, C, and Si on sample surfaces.

Results

Figure 2.28 shows the resulting water contact angle on the Si(100) samples after exposure. The figure shows that PFTS was by far the most hydrophobic surface, while FOTAS was the least hydrophobic. None of the simulated packaging exposures had an affect on water contact angle for any of the coating materials. The samples in Group 4,

exposed to a high concentration of water vapor at 310°C, exhibited a significant decrease in contact angle after exposure. In fact, the FOTAS coated samples were no longer hydrophobic after this exposure, yielding contact angles between 85 and 87 degrees.

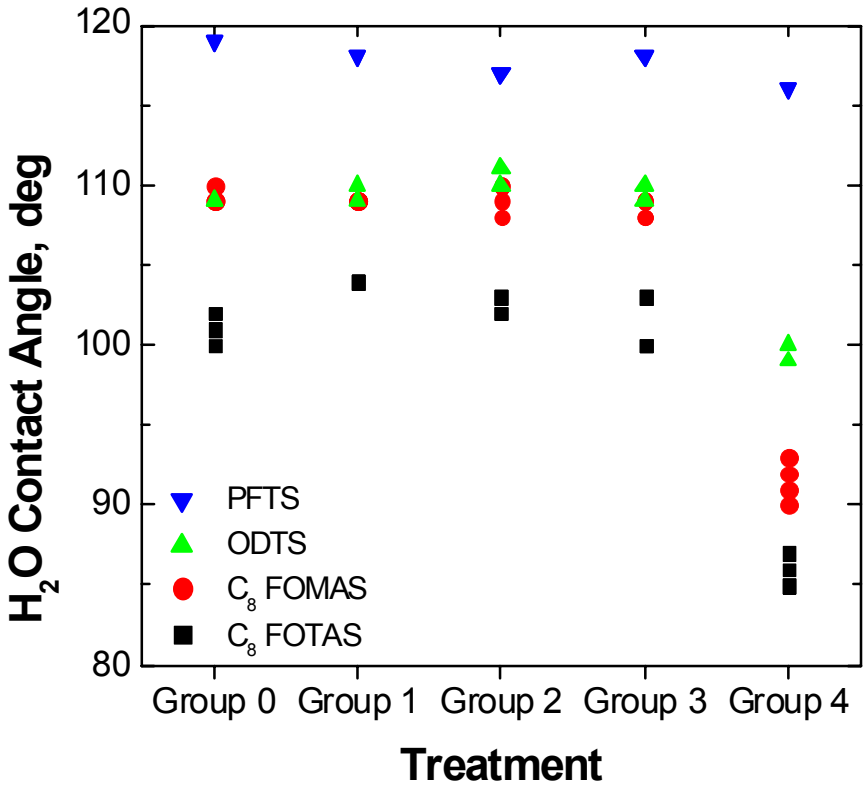

Figure 2.28 Water contact angle for several monolayer surface treatments in the as-deposited condition (Group 0), after exposure to simulated packaging operations (Groups 1-3) and after exposure to water vapor at 310°C (Group 4).

Composition measurements for the exposed samples are summarized in Figure 2.29. Figure 2.29 shows that for samples exhibiting a decrease in water contact angle (Group 4), there is a corresponding decrease in the atomic concentration of elements making up the coating (C and/or F). The fluorine concentration of the PFTS film did not significantly decrease after exposure to this environment, in agreement with the lack of change in contact angle.

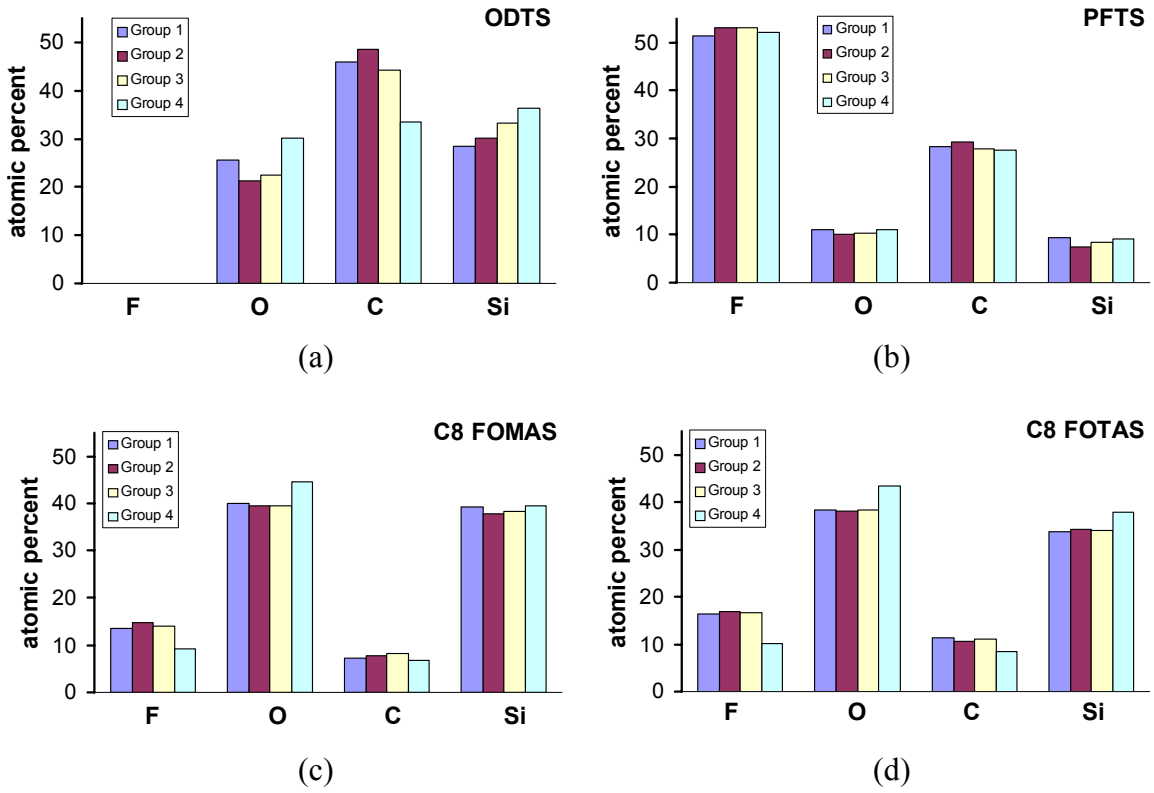

Figure 2.29 Atomic concentration of major constituents of ODTS (a), PFTS (b), FOMAS (c), and FOTAS (d) after exposure to simulated packaging conditions (Group 1-3) and after exposure to water vapor at 310°C (Group 4).

Comparison of peak shapes in XPS can be used to reveal changes in the bonding configuration of species at the surface. This is conventionally done by acquiring high resolution spectra around each of the constituent peaks, and then normalizing the peak for each element to constant total intensity. Subtle changes in peak shape and position can then be distinguished more easily, without the confusion that could be introduced by comparing peaks of very different height. The F 1s, O 1s, C 1s and Si 2p spectral regions were normalized to constant area (relative to background) for comparison. Of the coatings investigated in this study, only the C8 FOMAS exhibited any changes in peak shape with exposure. Figure 2.30 shows the normalized spectral regions for the FOMAS coating. In particular, a shift in the relative amounts of CF_3 and CF_2 bonding is seen after the first heat treatment in air, simulating die attach epoxy curing. A larger concentration of the more highly-fluorinated CF_3 species is observed in the first exposure. After subsequent exposures, the spectrum is dominated by CF_2 species.

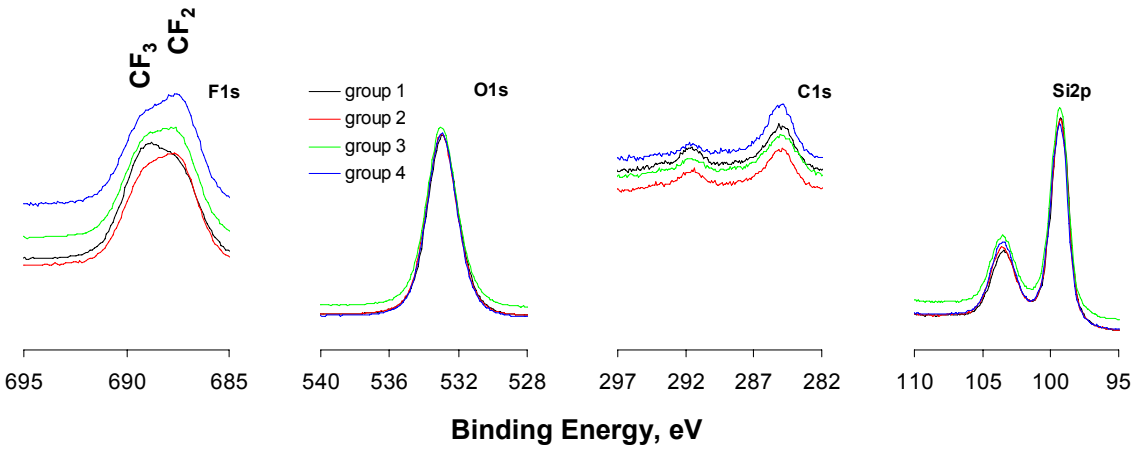

Figure 2.30 High resolution XPS spectra of the primary constituents of the C8 FOMAS film, normalized to constant total peak area (relative to background) by element. A change in relative concentration of CF_2 and CF_3 species is observed after the first exposure.

Conclusions

Exposure to elevated temperature in an inert atmosphere does not appear to degrade a FOTAS-treated surface, at least for short term exposures representative of typical MEMS packaging procedures. Similar to alkylsilane films, elevated temperatures combined with exposure to water vapor leads to loss of the molecule from the surface by hydrolysis. Interestingly, the hydrophobicity of the FOTAS treated surface was less than that achieved using previous, liquid deposition methods for alkylsilanes. This probably reflects insufficient deposition time to achieve full monolayer coverage for the FOTAS film using the standard process. In addition, the FOTAS film appeared to be less stable to reaction with water vapor than the PFTS film was. This is probably related to the lower total areal density of FOTAS molecules on the surface compared to PFTS molecules, providing more defect sites for adsorption and reaction of water vapor. Since it is not possible to completely exclude water or contaminants with other than a complete high vacuum process, other surface treatment options would be required to insure that all surfaces of the devices are covered. This could be accomplished with a bound plus mobile lubricant layer, as well as actuating devices at the die level and then recoating to fill in uncoated or damaged areas.

2.3.4 Occluded Region Structures

Procedure

Two devices were designed to test the effect of occluded versus line of sight coverage in actual device structures.

First, a beam in cave structure was devised. This structure is designed to provide high aspect ratio surface that has access to the VSAM from one side only. Therefore, complete coverage of the structure requires transport from the entrance of the cave

through the cave to cover the entire surface. Once coated, the beam can be extracted from the cave and latched into place. The device can then be analyzed by high resolution methods such as ToF-SIMS. This device suffers from several shortcomings. First, the beam is suspended in the cave during VSAM deposition. The gap between the cave ceiling and the beam, limited by oxide layer thickness and design rules, is sufficient that the VSAM is able to penetrate very large distances. Secondly, since the beam is supported by a spring suspension after release, the beam may not remain in the center of the cave after the oxide is removed. Finally, and most problematic for quantification, the beam is only 2μm wide, which causes the ToF-SIMS spectra to be dominated by edge effects.

A second approach was taken to better simulate occluded surfaces, using flap structures. Flaps in poly12 (P12) or poly3 (P3) were created having dimensions just sufficient to allow release during the oxide etch process used in the fab. The flap dimensions are 50 x 100 microns, and were designed with wide dimples underneath as well as dimple-less. The tabs are hinged on one side, and have a tab in the upper layer of polysilicon (P3 for the P12 flaps and P4 for the P3 flaps) on the opposite side to hold the flaps in the as-fabricated position during release and coating. The flaps are designed to fall to rest on the underlying substrate after release. During the coating process, the space between the bottom of the flap and the underlying layer is determined by the oxide layer thickness for the dimpled flaps, or in the case of flaps without dimples the separation is governed by the roughness of the two contacting surfaces. Roughness also governs separation between the dimples and the substrate on the flaps with dimples. At this point, VSAM is deposited on the die. Once coated, the tabs can be broken off, the flaps flipped over, and then latched into place to prevent static forces from moving the beams. The top of the underlying substrate is now exposed as well as the bottom side of the flap, and both are ready for surface analysis. The large area of the flap simulates a tortuous path seen in occluded areas of devices such as hinge joints and gear hubs.

Results

The beam in cave structure was first used to test the ability of ToF-SIMS to measure VSAM coverage. Spectral images were acquired on the extracted beam structure after VSAM deposition. The resulting images were processed using Sandia National Laboratories' Automated eXpert Spectral Image Analysis (AXSIA) multivariate analysis toolkit. This analysis method is fully documented elsewhere (9).

Flap structures were also tested using ToF-SIMS. Spectral images were acquired at four locations on two separate die. The data is then concatenated together to form an image montage. The mean ion image resulting from the montage is shown in Figure 2.31, for flaps that have been flipped over and latched in place. The hinges can be seen on the left side of each flap, and the central latch on the right side. The four locations analyzed on each die correspond to the four types of flap devices that were designed. Device 1 and device 3 are flat flaps made of poly1-2 on poly0 and poly3 on poly2 respectively. Devices 2 and 4 are made of the same poly levels, but have dimples on the bottom of the flap structure.

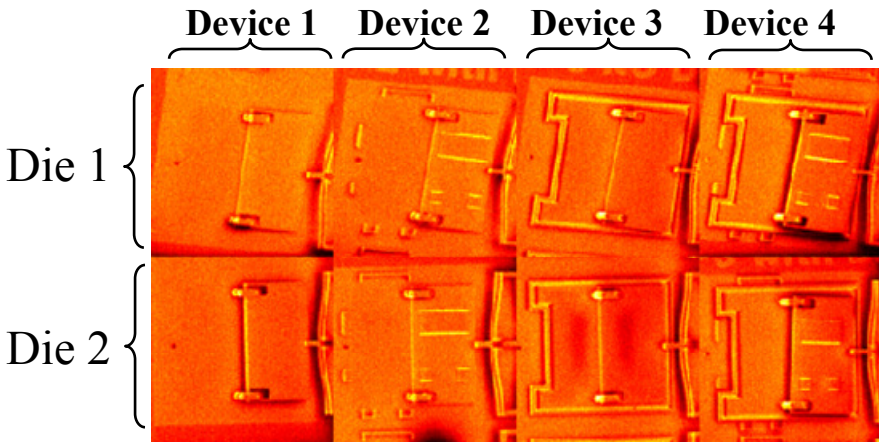

Figure 2.31 ToF-SIMS mean ion image montage of VSAM coated, flipped, and latched flap structures. Note that device 2, Die 2 and Device 4, die 1 locations have uneven response in total signal. This is due to field effects caused by a metal grid that was placed on the surface of the die for ToF-SIMS analysis.

The spectral image montage was processed using AXSIA. Three components were resolved in the analysis. Figure 2.32 shows the three components that were seen. Component 1, seen in tiles a. and d. represent the mainly occluded areas. The regions of the image that are highlighted are the substrate that was under the flap structure, and the underside of the flap structure itself. Component 2, seen in tiles b. and e. highlight the exposed areas of the die. Both components 2 and 3 contain VSAM fragments, but in different ratios. Component 3, seen in tiles c. and f. is the signal originating from the substrate. This component contains silicon peaks as well as some hydrocarbon signal. The separation of the VSAM signal into occluded and exposed fractions is caused by fragmentation differences in the two regions. Note that all of the same peaks occur in both components, but are at different relative intensities. The main difference is the C^+ peak at m/z=12 and the SiF^+ peak at m/z=47.

A change in coverage of the VSAM molecule is easily seen when comparing the two VSAM components. Die 1, device 3 and die 2, device 3 show changes in the VSAM signal in the occluded areas, while die 2, device 3 shows the most contrast. In fact, the second location shows a marked increase in substrate signal indicating intimate contact of the flap to the underlying structure during VSAM deposition.

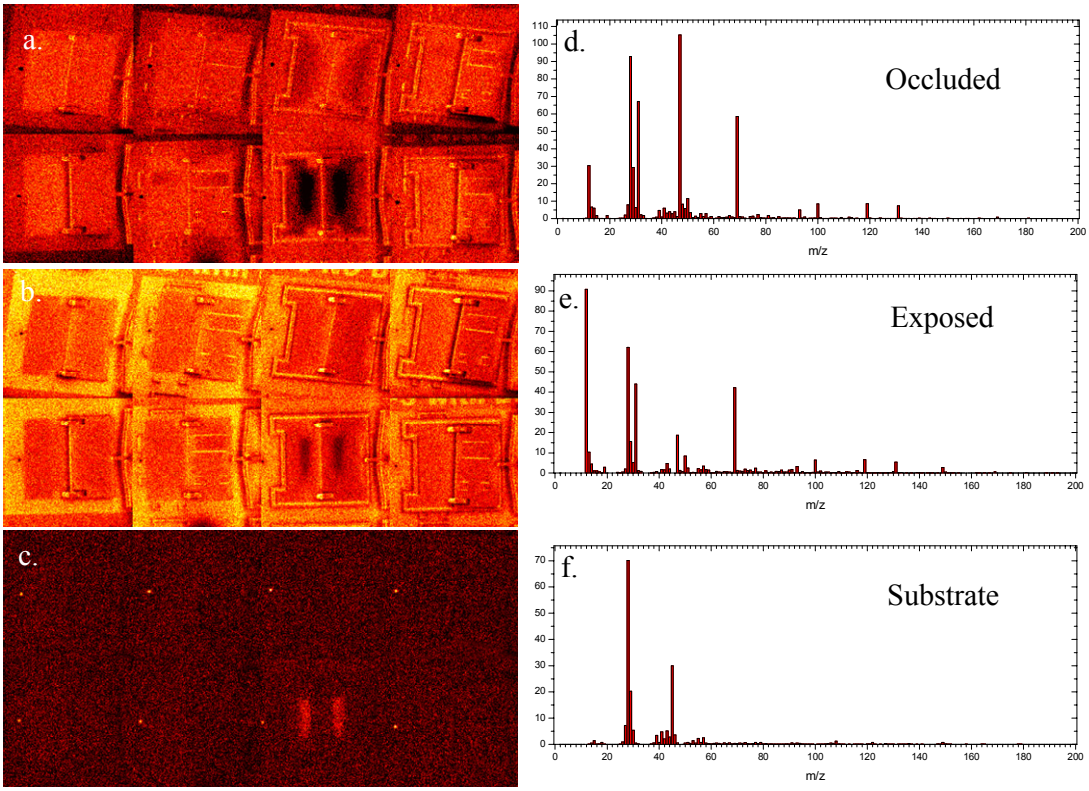

Figure 2.32 AXSIA analysis of die montage where tiles a. and d. are component 1 coming primarily from occluded areas, tiles b. and e. are component 2 coming primarily from exposed areas, and tiles c. and f. are component 3 coming from the substrate.

The spectral image montage contains full spectral data resolved over these 8 image areas in one dataset. Therefore, SiF^+ and Si^+ signals can easily be extracted from the data and processed with our calibration procedure to determine VSAM coverage in the image. Image slices from the SiF^+ peak and the Si+ peaks are extracted from the spectrum image, then smoothed by a 5x5 pixel averaging scheme. This averaging removes the high-frequency noise in the image data and provides numbers consistent with large area pixel averaging. A SiF^+/Si^+ image is created from the averaged peak images. Each pixel value is converted from the SiF^+/Si^+ ratio to VSAM coverage using the calibration formula. The resulting quantified image is shown as Figure 2.33.

The quantified coverage image montage can now be used to determine coverage values of the VSAM across the structure of interest. Note the die 2, device 3 location. In this location, a 'butterfly' image is seen. This same feature is slightly visible in the mean ion image and was obvious in the multivariate analysis. This portion of the image corresponds to a location where the flap came into intimate contact with the underlying substrate, limiting transport of the VSAM molecule in the low coverage areas. Both the concentration and size of the low concentration area can be determined from this image.

Areas of high concentration are also seen in the quantitated montage. This is an artifact of the SIMS process as edges enhance some fragments more than others. Additionally, the areas of low concentration seen in die1, device 4 and die2, device 2 are artifacts caused by field effects in the instrument.

The average VSAM concentration is ~2.5x10^{14} molecules/cm^2 and is generally homogeneous. No differences in coverage are seen in the line of sight versus occluded regions of the images. Lower concentration boxes do surround each structure. These areas are made of silicon nitride, which has a different fragmentation response than silicon. Therefore, these regions cannot be assumed to have a lower concentration of VSAM than the polySi structure itself. The adsorption of VSAM on nitride may also be different than on polySi, and contacts between nitride and polySi are generally not used in device design since the nitride may trap charge during contact, and ground planes are desired under movable structures to minimize effects due to charge accumulation.

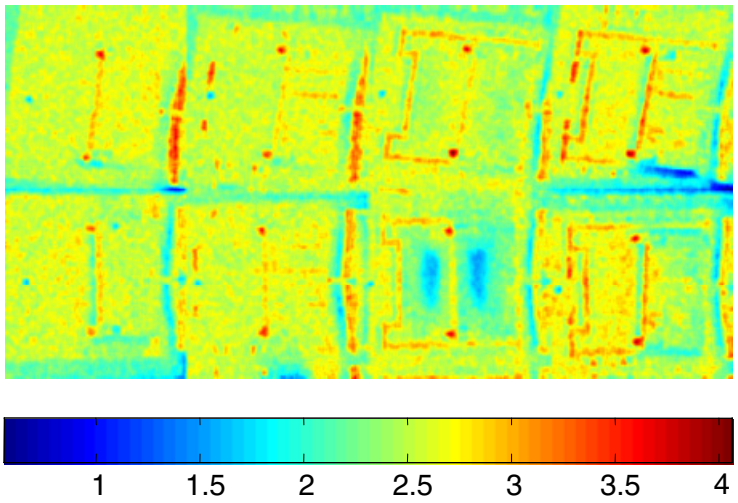

Figure 2.33 Image showing the quantification of the ToF-SIMS montage in units of 10^{14} FOTAS molecules / cm^2. The average concentration of exposed and occluded areas are the same: ~2.5x10^{14} molecules/cm^2. Red areas are an artifact caused by edges which affect fragmentation. Also, the field effect areas noted in Figure 2.31 are seen as low concentrations of FOTAS and are also an artifact.

Conclusions

VSAM covers hidden and line-of-sight surfaces equally in our devices in most cases. However, when two surfaces are in close enough contact to limit VSAM transport, a lower coverage is seen. Devices that have contacting surfaces in the as-released condition will have some areas that are in intimate contact. The coverage value measured for these areas in the flap structure can be used in further experiments to test frictional response of sidewalls in order to simulate device operation. The average coverage of VSAM using the standard deposition procedures for the aging die is ~2.5x10^{14} molecules/cm^2.

2.4 Sidewall Friction Experiments

2.4.1 Sidewall Morphology

Procedure

Examination of contact and sliding between polycrystalline silicon sidewall surfaces requires some knowledge of the morphology and roughness of the interacting surfaces. The sidewall surfaces are easily imaged in the SEM, but quantification of the surface roughness is challenging due to the orientation of the surface of interest perpendicular to the plane of the wafer. Atomic Force Microscopy (AFM) is the tool of choice for characterization of MEMS surfaces, but is capable of scanning only surfaces parallel to the wafer surface. In order to orient the sidewall for analysis, a poly12 beam was cut from a 2 μm wide MEMS device suspension (after release) and rotated 90 degrees using the in-situ manipulator in a Focused Ion Beam (FIB) sample preparation tool (FEI dual beam FIB, model DB235). The beam was then tacked in place by depositing platinum over one end of the beam inside the FIB. This was done to prevent the beam from shifting during contact AFM imaging, as preliminary attempts at imaging caused cut beams to move. Auger electron spectroscopy was used to verify that the platinum deposition was localized to within 10 μm of the target end. That is, no platinum could be detected more than 10 μm away from the edge of the area where it was deposited in the FIB. Therefore, the deposited Pt could be avoided and did not influence the AFM roughness measurements.

After cutting, rotating and tacking down the beam, a Digital Instruments DI3300 AFM was used to measure the sidewall surface. An etched silicon tip having nominal radius of curvature of 10 nm was used as the probe. An integrated optical microscope was used to place the tip on top of the beam with scan size set to zero. Once in feedback control, the tip position and scan size were adjusted to give a rectangular scan along the poly12 beam. This laminated polysilicon layer was 2.5 microns thick, and the entire beam was ~60 μm long.

Results

A resulting AFM image from the poly12 sidewall is shown in Figure 2.34. The scan is approximately 8 μm long and 2 μm wide, with the etch direction of the polycrystalline silicon oriented vertically and the top of the image toward the top of the poly12 laminate. A vertical texture can be seen in the figure, and is created during the plasma etch used to pattern the poly12 layer. This morphology is generated where grain boundaries in the polycrystalline silicon cross the mask edge, and is due to variation in the etch rate between the grain boundaries and interiors of the grains. The horizontal feature near the top of the image is the boundary between the poly1 and poly2 layers in the laminate, and the grain structure can be seen to renucleate at this level. The root-mean-squared surface roughness calculated from this image is 22 nm. Gear teeth, latches, and the rubbing surfaces in the sidewall MEMS tribometer will have this morphology. Contact of these types of surfaces having an overall curvature (such as an involute gear tooth) will result in very few points of contact, and depending upon the radius of curvature there may be a single point of real contact.

Figure 2.34 An 8 x 2 μm AFM scan of the poly12 laminate. The top of the image is near the top of the beam, and the discontinuity in grains represents the boundary between poly1 and poly2. The roughness is 22 nm rms.

2.4.2 Friction of Aged Devices

Procedure

The static friction coefficient was determined using the sidewall MEMS tribometer, in an effort to establish a relationship between the accelerated aging exposures and the friction response of aged surfaces. Although many devices were inspected and measurements attempted, reliable data was acquired from ten packages, primarily from the 500 ppmv H_2O and 200◦C exposures. These were from later release IDs, and later packaging runs which had a high percentage of working devices without packaging problems or surface damage due to handling. The specific packages where reliable static friction measurements could be performed are listed in Table 2-10.

Table 2-10. Parts used for Friction Measurements on Aged Devices

Release ID	Package ID	Time (hours)	Temperature (°C)	Humidity (ppmv)
4674	**767**	1000	200	474
4674	**768**	1000	200	474
4674	**769**	1000	200	474
4674	**790**	2000	200	477
4674	**791**	2000	200	477
4674	**792**	2000	200	477
4674	**793**	2000	200	477
4690	**670**	500	250	587
4258	**741**	Control Die - No Exposure		
4258	**750**	Control Die - No Exposure		

The surface coverage of FOTAS was determined using ToF-SIMS, as described above. Tests were then performed in order to determine the tribological properties of the devices. Two main experiments were performed – one to determine the friction forces and a second to determine the adhesion forces. These experiments were then combined to determine true friction coefficients. Static friction was the emphasis of these measurements, since these represent the forces that must be overcome after dormant storage in order to initiate device motion.

In the friction experiments, the load actuator was first activated in order to apply an external normal load of approximately 1.25 μN between the beam and the post. The shuttles are supported by conventional double folded flexure suspension systems. These suspensions can be modeled as linear springs with restoring forces given by:

$$F_r = 2kx = \frac{48EIx}{L^3} \tag{2.3}$$

where k is the suspension stiffness, x is the displacement, E is the elastic modulus of the polysilicon structural layer (165 GPa), I is the moment of inertia in the motion direction (~2.3 μm^4), and L is the suspension length (495 μm). The factor of two is present because each shuttle contains two double folded flexure suspensions. The mechanical restoring force is balanced by the electrostatic force of the comb drives given by:

$$F_e = \frac{N\varepsilon_0 \varepsilon h V^2}{g} \tag{2.4}$$

where N is the number of comb fingers (= 92 in the present design), ε_0 is the permittivity of vacuum (= 8.854×10^{-12} F/m), ε is the relative permittivity (= 1 for dry nitrogen), h is the structural layer thickness (= 6.75 μm), V is the voltage applied between stationary and moving comb fingers, and g is the gap between the comb fingers (= 3.2 μm).

The external normal load is given by the difference between the maximum electrostatic force and the mechanical restoring force at contact:

$$N_{ex} = F_e^{\max} - F_r^{con} \tag{2.5}$$

where $F_e^{\max}$ and F_r^{con} are given by Equations 2.4 and 2.3, respectively. The superscript 'max' refers to the maximum applied loading voltage and the superscript 'con' indicates the restoring force at the instant of contact.

Next, the voltage of the shear actuator was ramped up through the inception of surface sliding. As the voltage was ramped up, a series of images were taken of the device. A plot of position versus shear force could then be generated using the series of images. Figure 2.35 shows a set of characteristic friction data used to determine the critical sliding voltage.

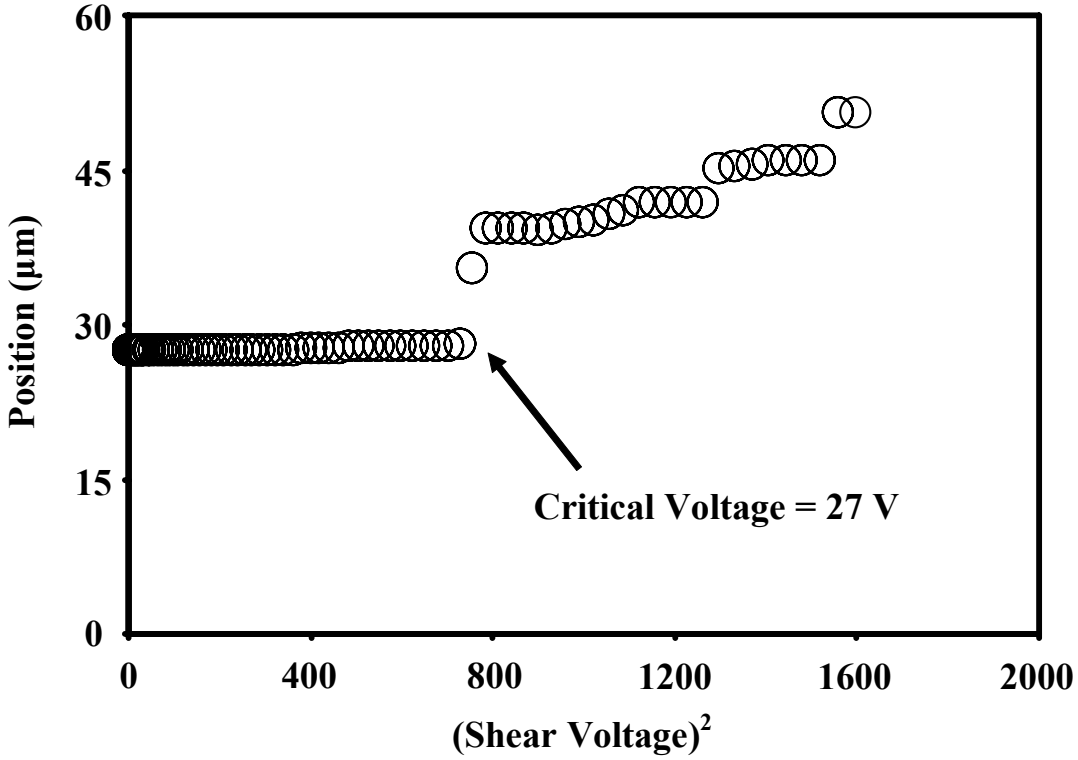

Figure 2.35 Beam position as a function of the square of the shear voltage used to determine the critical voltage for the inception of sliding.

The position is given as a function of the voltage squared because the electrostatic force is proportional to voltage squared as shown in Equation 2.4. At the instant of surface sliding, the electrostatic force in the shear comb drive is balanced by the static friction force and a simple balance can be struck in order to back out the friction force:

$$F_f = \frac{N\varepsilon_0 \varepsilon h V_{crit}^{\ 2}}{g} \tag{2.6}$$

where V_{crit} is the critical voltage at which surface sliding first occurs. The friction force can be divided by the external normal load to give the engineering coefficient of friction:

$$\mu_e = \frac{F_f}{N_{ex}} \tag{2.7}$$

In the adhesion experiments, the initial normal load was applied in the same manner as in the friction experiments. An unloading voltage was then ramped up through the instant of surface separation. At this instant, a force balance can be made in order to gain the adhesion force:

$$F_{ad} = F_e^U + F_r^{con} - F_e^L \tag{2.8}$$

where F_e^U and F_e^L are given by Equation 2 and are the electrostatic forces in the unloading and loading comb drives, respectively.

The position of the beam with respect to the post was monitored as the unloading voltage was ramped up and a series of images were taken during the testing cycle. A plot of the position as a function of the unloading voltage was then generated to determine the critical separation voltage. Figure 2.36 shows a set of characteristic adhesion data.

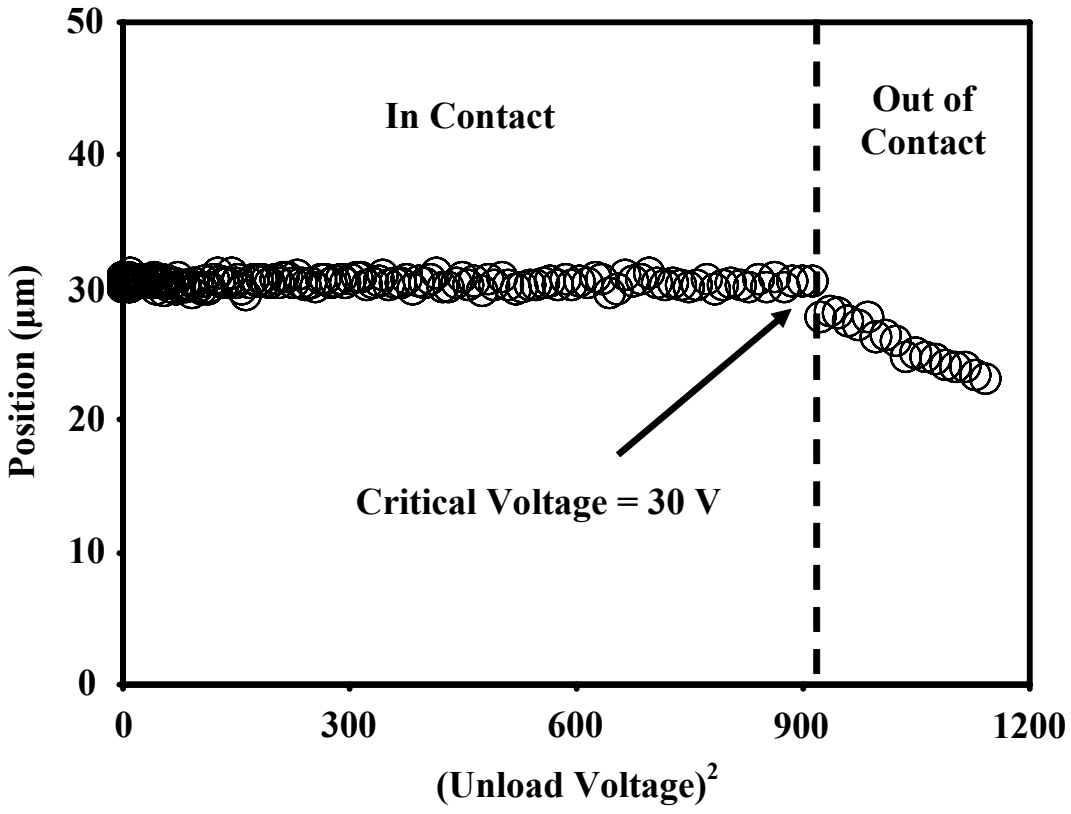

Figure 2.36 Beam position is plotted as a function of the square of the pull-out voltage in order to determine the critical voltage for surface separation.

Once the adhesion data were taken, the information could be combined with the friction data to determine the true coefficient of friction:

$$\mu_t = \frac{F_f}{N_{ex} + F_{ad}} \tag{2.9}$$

The denominator in Equation 7 represents the total normal load and is the sum of both external and internal components.

For statistical purposes, ten friction tests and ten adhesion tests were performed on each of the ten modules. All experiments were performed in a dry nitrogen environment with oxygen content of less than 5 ppm. It is important to note that although the aging environments on the test die were different, they were all tested in the same environment. This was done in order to investigate only the effects of aging on the shear behavior of the interfaces, and minimize the confounding of this information with additional forces due to capillary effects. Voltages were computer-controlled and were applied to the actuators using a DC power supply (Kepco, ATE 150-0.3M) and a series of function generators (Pragmatic Instruments, Inc., 2414A). The devices were visually monitored using an optical microscope (Mitutoyo America Corporation) and routed to imaging software through a Panasonic video camera.

Results

The tribological test data were plotted as a function of the FOTAS coverage determined by ToF-SIMS. Figure 2.37 shows the average friction force for each sample as a function of the monolayer concentration. It can be seen from this plot that the friction force decreases with increasing surface coverage. A decrease of approximately 0.3 μN was found using a linear estimation over the 3.1×10^{13} molecules/cm^2 range of surface coverage. A linear estimation was used due to the small range of surface coverage. However, it is predicted that this decrease will saturate as the coverage reaches its maximum value. The maximum theoretical density based on Langmuir films of fluoroalkanes and fluoroalkylthiols is 3.4×10^{14} molecules/cm^2, while the number of available bonding sites (for a single crystal SiO_2) is 4.6×10^{14} sites/cm^2 [2.14]. The molecular density therefore appears to be limited more by stearic constraints than the number of available bonding sites. Furthermore, it appears that FOTAS films on polysilicon structural members have coverage less than saturation, even for deposition times investigated that were longer than that used in the standard process.

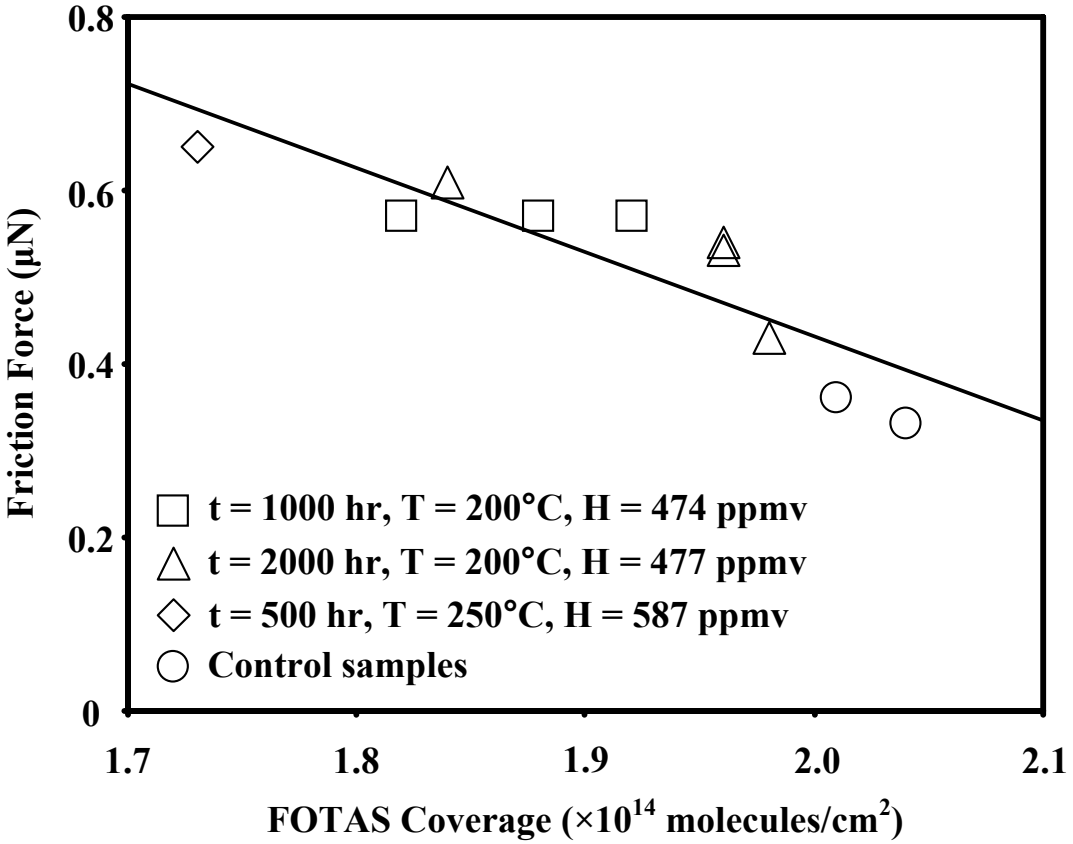

Figure 2.37 Static friction force as a function of FOTAS concentration.

Similarly, the engineering coefficient of friction decays with increasing monolayer coverage. This is shown in Figure 2.38. The data shows a decrease of 0.2 in this particular range of coverage. Again, it is predicted that this decrease will saturate as the available bond sites on the surface become scarce.

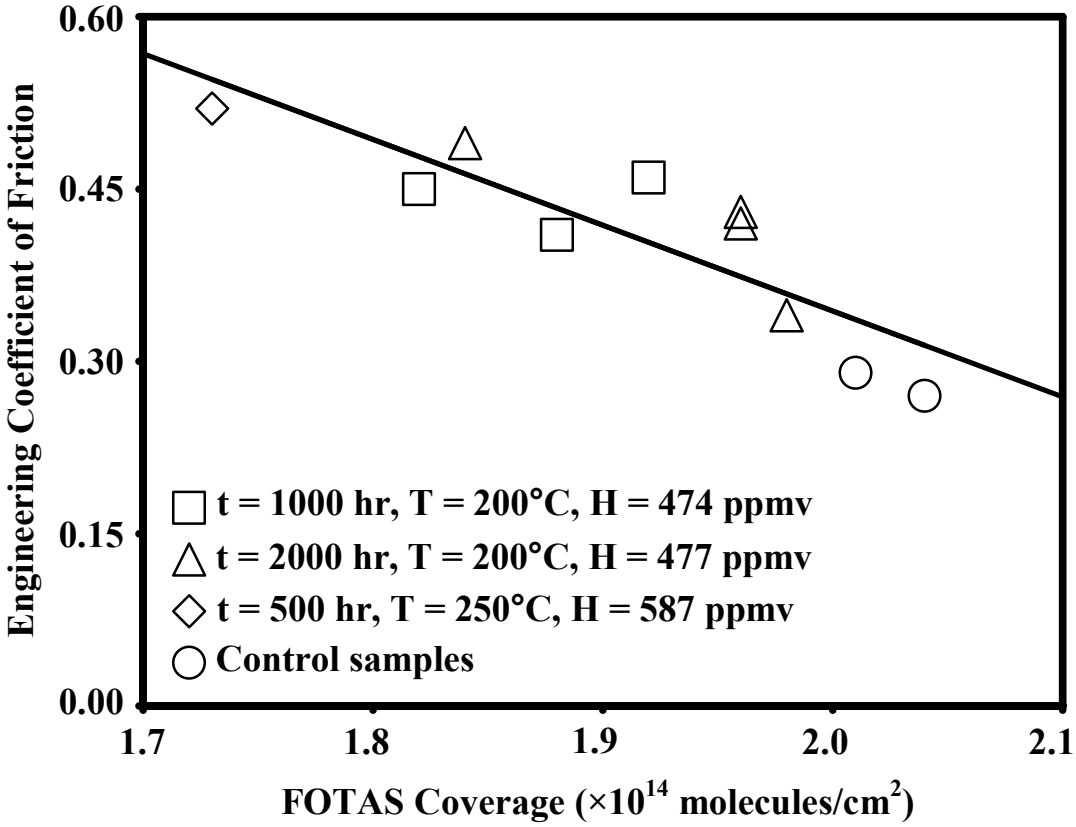

Figure 2.38 Engineering coefficient of friction as a function of FOTAS concentration showing a decrease of friction with increasing surface coverage.

The behavior of the adhesion force as a function of surface coverage is shown in Figure 2.39. Over this range of monolayer coverage, the adhesion force decreases by 0.076 μN.

The adhesion and friction data are combined in Figure 2.40 to show the true coefficient of friction as a function of the monolayer coverage. Over the range of monolayer coverage examined herein, the true coefficient of friction decrease 0.2. It is noted that this is the same decrease as the engineering coefficient of friction. This agreement is due to the fact that, at the tested external load (1.25 μN) and with the low surface energy coating (FOTAS), the adhesion force is not an appreciable portion of the total contact load. If the experiments were performed at a lower load or on devices with a higher surface energy, the adhesion force would be a more significant portion of the total normal load and therefore would have a greater impact on the true coefficient of friction. This hypothesis is consistent with experiments performed by Timpe and Komvopoulos that found a major difference between the engineering coefficient of friction and the true coefficient of friction only at low loads [2.15].

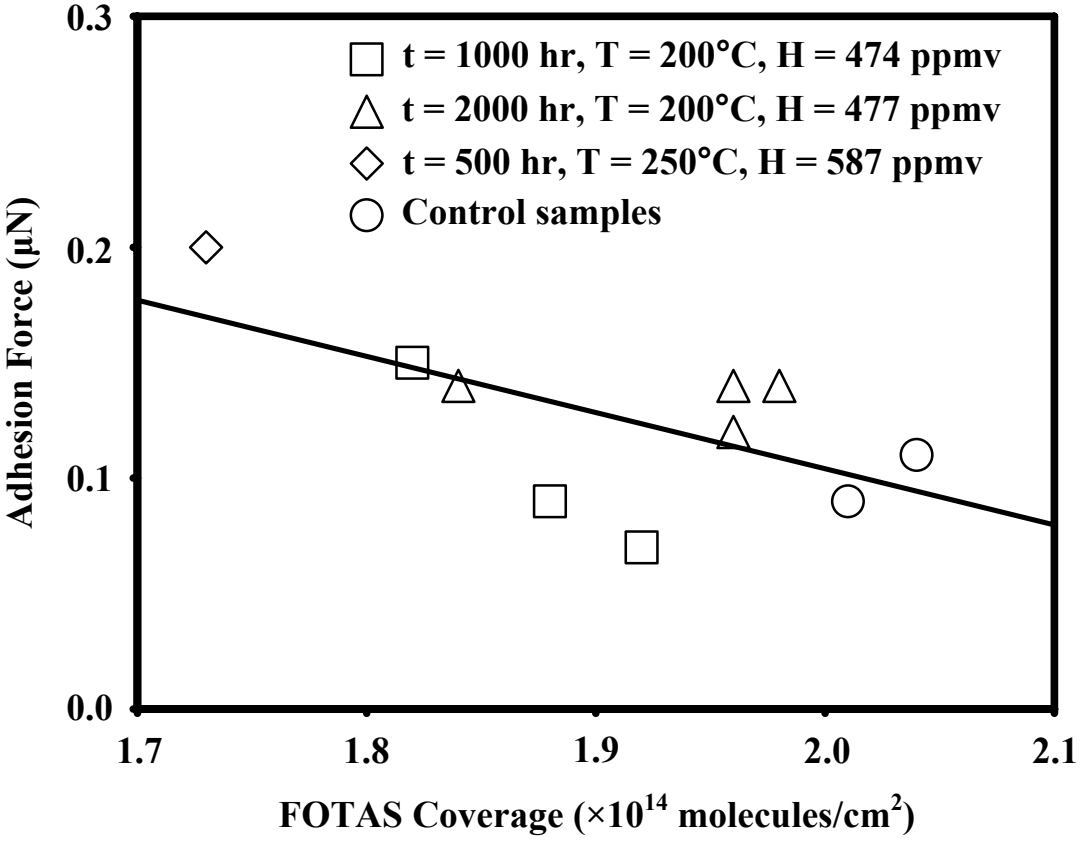

Figure 2.39 Adhesion force as a function of FOTAS concentration showing a decrease in adhesion with increasing concentration.

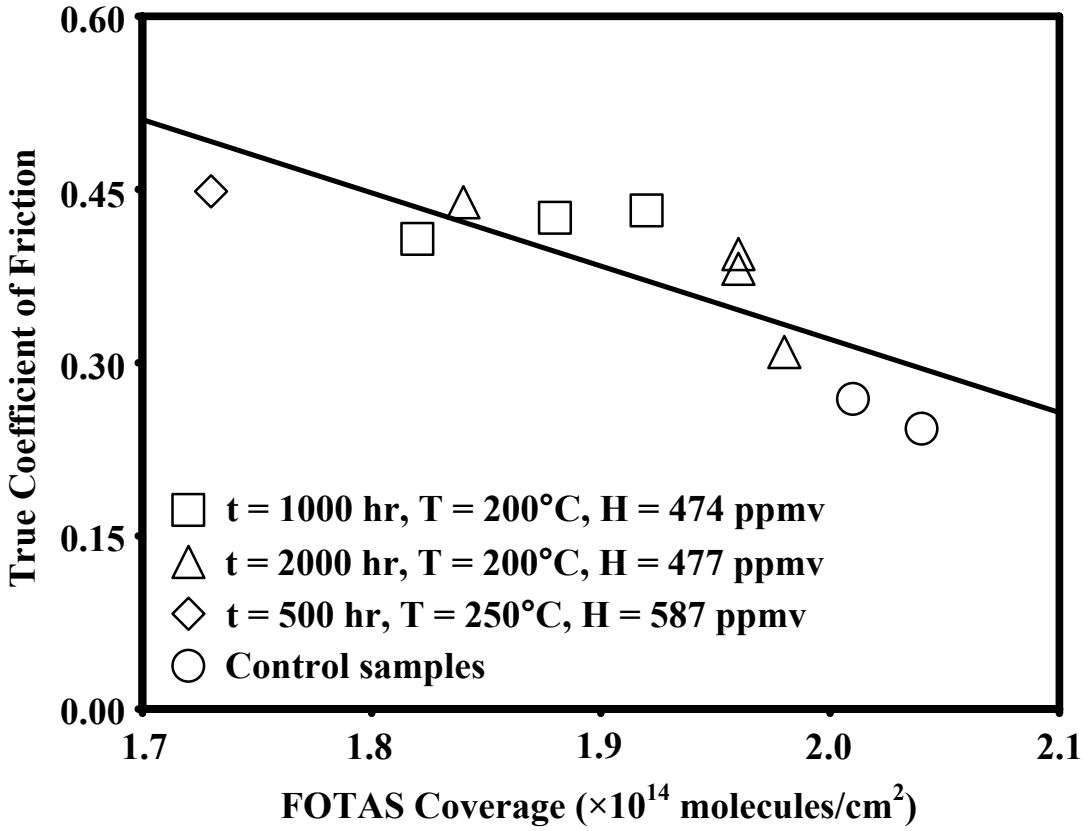

Figure 2.40 True coefficient of friction, corrected for adhesion force, as a function of FOTAS concentration.

2.4.3 VSAM Process Changes

The VSAM deposition process consists of cleaning the die in an oxygen + water vapor plasma, and then exposing them to the FOTAS precursor for a limited time. In the process used for the aging die discussed above, the FOTAS precursor was held at 50°C and the die were exposed for 10 minutes. The deposition chamber was cleaned only with a nitrogen plasma between coating deposition runs, resulting in a background residual pressure of FOTAS fragments that would begin adsorbing on the surface immediately after the die were introduced. This resulted in some variability in coverage even when the process was run with identical parameters each time. Unfortunately, the VSAM deposition process was changed during the course of this project, in January 2005. An oxygen plasma was used to clean the chamber between runs, resulting in no residual FOTAS presence until the valve to the precursor was opened. Water contact angles were found to be lower for the same 10 minute deposition time used previously, so the precursor temperature was raised to 60°C and the standard deposition time change to 12 minutes.

The net result of the VSAM process changes are expected to produce films with a concentration of FOTAS per unit area that is much closer to saturation than before, and these films are expected to be more resistant to adsorption of contaminants and attack by water vapor. This results in much better control of what is chemisorbed on the surface, but precludes direct comparison of future studies with the hundreds of aging die coated previously as part of this project, since the residual concentration in the deposition chamber "aged" by cleaning with only nitrogen plasma cannot be reproduced. Still, with the capability to quantify FOTAS areal density using ToF-SIMS, the aging information generated here is still relevant, although it probably yielded coverage that is below saturation. The observed aging behavior could therefore be considered a worst case compared to newer parts coated using the new VSAM process.

2.4.4 Friction of Partially-Coated Devices

Procedure

In light of the narrow range of VSAM coverage exhibited by the tests of aged packages, an examination of friction behavior as a function of FOTAS coverage over a larger range of coverage was desired. The friction of completely uncoated devices is virtually impossible to obtain, since uncoated devices have low yield through release, and the surfaces are immediately contaminated by residues from supercritical drying as well as adsorption from the atmosphere. However, the coverage can be adjusted by varying the amount of time the FOTAS precursor is exposed to the surface during vapor deposition.

For these experiments, friction devices were released as before, and supercritically dried. The modules were cleaned in an oxygen + water vapor plasma to oxidize and hydrolyze the surface in preparation for FOTAS chemisorption. The VSAM deposition process was repeated with the precursor at 50°C and then at 60°C to quantify differences in coverage due to precursor temperature. The test devices were then placed in the vapor deposition tool for times between 60 and 1300 seconds, in order to vary the FOTAS coverage.

After the modules were treated, FOTAS coverage was quantified using ToF-SIMS as described above for the aging modules, and static friction was measured as described above, for the set of modules coated at 60°C precursor temperature.

Results

The results of FOTAS coverage with the new VSAM process, and the precursor held at two temperatures, is shown in Figure 2.41. As expected, the higher precursor temperature resulted in greater coverage of FOTAS at all deposition times. The figure also shows that the range of coverages observed on aging die are significantly less than what would be expected of future depositions using 60°C precursor for 12 minutes exposure (~2.7×10^{14} FOTAS/cm^2). Finally, this data suggests that the surface is still not saturated with FOTAS using the new VSAM deposition process. The coverage at 1300 seconds deposition time suggests that saturation coverage may be near 3.0×10^{14} FOTAS/cm^2.

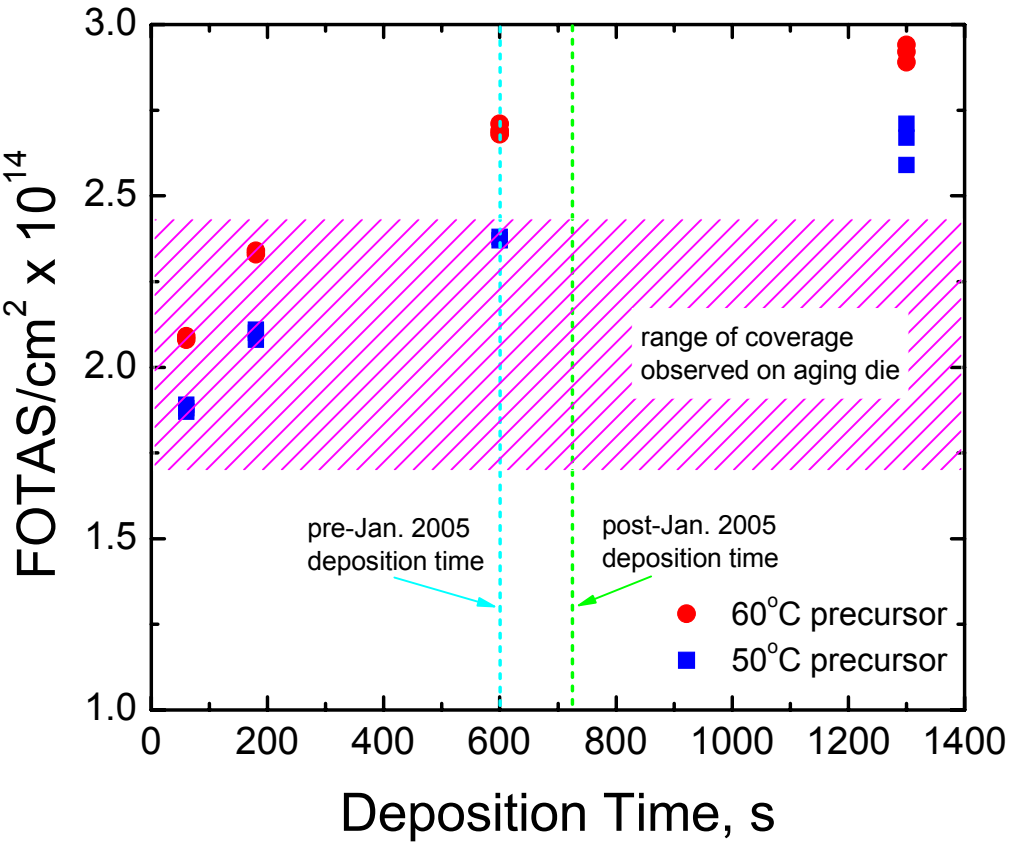

Figure 2.41 FOTAS coverage as a function of deposition time for 50°C and 60°C precursor temperatures.

Results of static friction measurements on these die are shown in Figure 2.42, which also shows the friction measurements on the aged modules discussed previously. Note that the friction measurements from the "partial coverage" die cannot be directly compared to those from the "degradation" experiment due to changes in the process (principally the change in chamber cleaning process prior to the partial coverage experiments). However, a similar range of friction coefficient values are obtained in the latter work. Friction decreases with increasing coverage, from 0.45 at 2.1×10^{14} FOTAS/cm^2 to about 0.30 at 2.7×10^{14} FOTAS/cm^2, or a 50% reduction in friction for a 33% change in coverage. Since some of the data for the degradation experiment was acquired on control die, stored in N_2 after FOTAS deposition, it appears that the die coated for longer times in the partial coverage experiment have about 50% more FOTAS on them than resulted from the previous VSAM process. The die coated for the longest time in this experiment have FOTAS coverage much closer to what would be expected based on stearic constraints on molecular packing (~3.4×10^{14} FOTAS/cm^2).

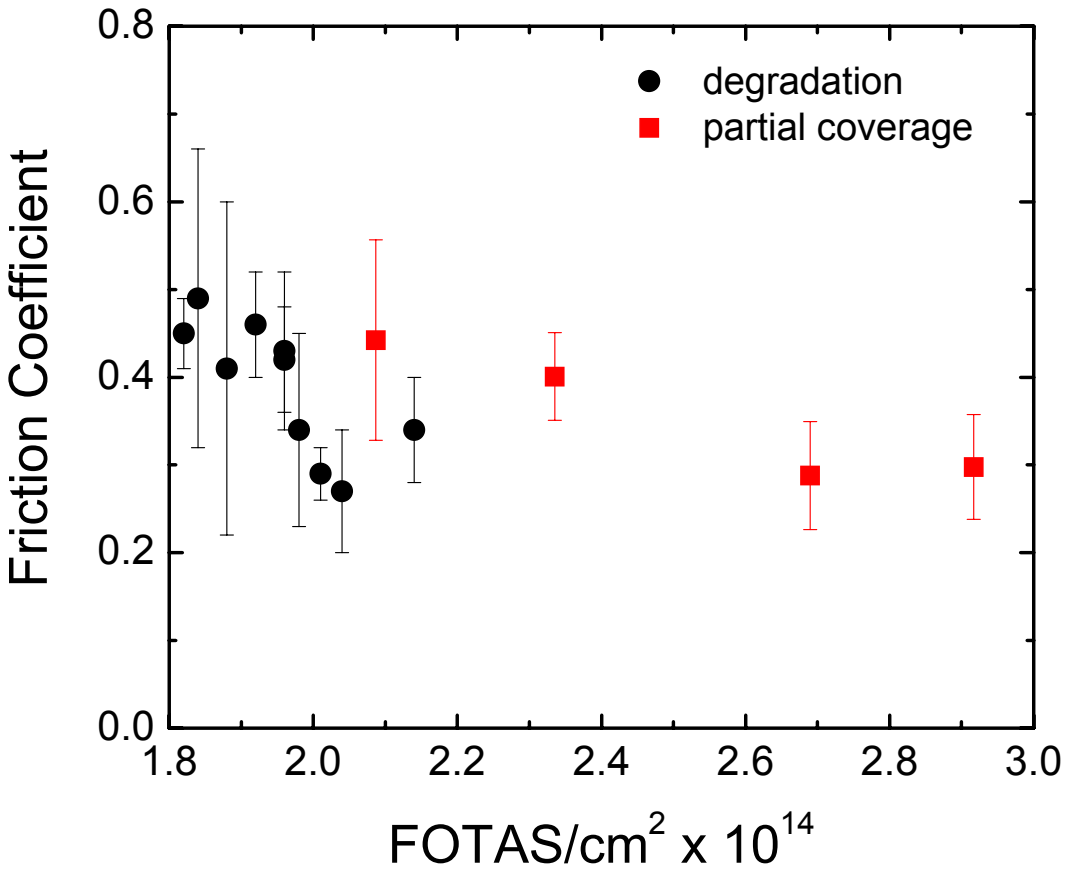

Figure 2.42 Static friction coefficient as a function FOTAS coverage determined by ToF-SIMS for "degradation" die coated with the old VSAM process, and for "partial coverage" die coated using the new process.

2.4.5 Conclusions

The aged devices exhibit FOTAS coverage between 1.7 and 2.1 x 10^{14} molecules/cm^2, and although the control samples contain the most FOTAS and the 250°C samples the least, there is significant variability in FOTAS coverage on the die selected for friction measurement. The variability is so large, in fact, that it masks any trends in coverage with exposure temperature, time, or water vapor concentration. This is true despite the fact that most of the tested packages came from one release run. However, plotting friction and adhesion force as a function of FOTAS coverage reveals a correlation between the two in dry nitrogen operating environments – adhesion and friction decrease with increasing FOTAS coverage.

Relationships such as that shown in Figure 2.42 can form the basis of an age-aware model of interface behavior. For any surface treatment process, the interface behavior can be characterized as a function of surface composition. If the surface composition can be related to exposure time via a kinetic model of the degradation process, then an age-aware model can be developed to describe how the behavior of the interface changes with time. Generating reproducible coverages significantly below 2.0x10^{14} FOTAS/cm^2

would be challenging with the current VSAM process, but a modified process could be used to generate an even wider range of coverages. Additional work to quantify the kinetics of the hydrolysis reaction that results in loss of FOTAS with exposure to water vapor could then be used to determine coverage as a function of age. Friction or adhesion could then be predicted based on the anticipated storage environment, and these parameters used in a dynamic model of device function to predict the impact of aging on device behavior.

Issues associated with dynamic modeling of MEMS devices are discussed in the next section.

Chapter 2 References

2.1. M.G. Hankins, P.J. Resnick, P.J. Clews, T.M. Mayer, D.R. Wheeler, D.M. Tanner, and R.A. Plass, "Vapor deposition of amino-functionalized self-assembled monolayers on MEMS," Proceedings of the SPIE - The International Society for Optical Engineering, 2003; **V4980**, pp. 238-47.

2.2. S.T. Patton, W.D. Cowan, K.C. Eapen, and J.S. Zabinski, "Effect of surface chemistry on the tribological performance of a MEMS electrostatic lateral output motor," *Tribology Letters*, 2001; **V9**, No. 3-4, pp. 199-209.

2.3. H.W. Liu and B. Bhushan, "Adhesion and friction studies of microelectro-mechanical systems/nanoelectromechanical systems materials using a novel microtriboapparatus," *Journal of Vacuum Science & Technology*, 2003; **V21**, No.4, pp. 1528-1538.

2.4. D.M. Tanner, J.A. Walraven, S.S. Mani, and S.E. Swanson, "Pin-Joint Design Effect on the Reliability of a Polysilicon Microengine," Proceedings of IRPS, 2002, pp. 122-129.

2.5. W. Nelson, *Accelerated Testing: Statistical Models, Test Plans, and Data Analyses*, New York: John Wiley & Sons, 1990, ch. 3, pp. 145-154.

2.6. SUPREM, Stanford University, http://www-tcad.stanford.edu/tcad/programs.html

2.7. M.P. de Boer and T.A. Michalske, "Accurate method for determining adhesion of cantilever beams," in *Journal of Applied Physics*, **V 86**, No. 2, 15 July 1999, pp. 817-827.

2.8. B.D. Jensen, M.P. DeBoer and S.L. Miller, "IMaP: Interferometry for Material Property Measurement in MEMS," proceedings of the 1999 International Conference on Modeling and Simulation of Microsystems, San Juan, Puerto Rico, April 19-21, 1999.

2.9. J.A. Ohlhausen, M.R. Keenan, P.G. Kotula, and D.E. Peebles, "Multivariate statistical analysis of time-of-flight secondary ion mass spectrometry images using AXSIA," in *Applied Surface Science*, **V231-232** (2004) p.230-234.

2.10. U. Srinivasan, M.R. Houston, R.T. Howe, and R. Maboudian, "Alkyltrichlorosilane-Based Self-Assembled Monolayer Films for Stiction Reduction in Silicon Micromachines" *J. Microelectromechanical Systems* **7**, pp. 252-260, 1998.

2.11. M.T. Dugger, R.J. Hohlfelder and D.E. Peebles, Degradation of monolayer lubricants for MEMS, Proceedings of the SPIE - The International Society for Optical Engineering **vol.4980** (2003) pp. 138-150.
2.12. T.M. Mayer, M.P. de Beer, N.D. Shinn, P.J. Clews and T.A. Michalske, "Chemical vapor deposition of fluoroalkylsilane monolayer films for adhesion control in microelectromechanical systems," *Journal of Vacuum Science & Technology B* **vol.18** (2000) pp. 2433-40.
2.13. M.G. Hankins, P.J. Resnick, P.J. Clews, T.M. Mayer, D.R. Wheeler, D.M. Tanner and R.A. Plass, "Vapor deposition of amino-functionalized self-assembled monolayers on MEMS," proceedings of the SPIE - The International Society for Optical Engineering **vol.4980** (2003) pp. 238-47.
2.14. Thornberg, Brown, Zavadil, Ohlhausen, Tallant, Garcia, Simpson, Kent and Ordonez , "MEMS Characterization LDRD Final Report (FY03-FY05)," **SAND2005-7083** (2005), Sandia National Laboratories, p. 30.
2.15. S.J. Timpe and K. Komvopoulos, "A Combined Experimental Study of Friction and Adhesion in Microelectromechanical Systems" (in preparation), 2006.

3. Modeling

The initial objective of the modeling component of this study was to provide a predictive capability for the behavior of MEMS devices after a period of dormancy. The experimental results indicate that we do not have a complete enough understanding of the physical mechanisms that produce "adhesion failure" at start-up (e.g., deposition of materials at interfaces) to incorporate them in a model. Nonetheless, progress was made on modeling MEMS devices with adhesion.

The study focused on device level modeling and in particular gear-hub interactions. Since there was an initial interest in modeling the dynamics of a complete DMS gear train, we took an approach that used both finite element analyses (FEA) and rigid body dynamic (RBD) analyses. This approach also had the potential advantage of allowing random initial configurations of a gear train for examining start-up. However, RBD models by definition do not address component stiffness and inertia from an elastic continuum point of view. We assumed that local deformation of the individual components of the MEMS device could be treated with simple contact models and that vibration of individual components (e.g., of an individual gear) was not an important factor.

To examine the potential for incorporating the effects of adhesion in RBD analyses, FEAs were conducted to assess the effect of adhesion on the gear-hub interaction. The hub and gear hole side-wall surfaces were idealized as cylinders. Of course these idealizations are questionable, since these surfaces can be relatively rough. As such, the FEA results might be viewed as first order approximations, since more accurate analyses would need to address the interaction of asperities (which is beyond the scope of this study). While the initial motivation for this aspect of the work was to incorporate a simplified adhesion-friction model into the RBD models (for dynamic analysis), the final application was to estimate the importance of this contact toward inhibiting start-up.

The following sections address: (1) gear-hub contact modeling, and (2) rigid body dynamic modeling of devices.

3.1 Gear-Hub Contact Modeling

An initial goal of the gear-hub contact modeling was to determine if a complete FEA of the DMS gear train was possible, or if we would need to take a combined FEA-RBD approach as outlined above. To assess the needed mesh density in the region of contact, the FEA results were compared with a closed form solution (for the case of no adhesion) that is available in the literature [3.1].

3.1.1 Closed-Form Solution

A closed form solution for a cylindrical pin contacting a cylindrical hole in a thin, infinite plate (plane stress) was obtained by Persson [3.1]. He assumed that the pin and plate are made of the same homogeneous, isotropic, elastic material and that the plate was of unit thickness. The following relations were used to relate a measure of the contact area to contact force.

$$\frac{E\Delta R}{Q} = \frac{2}{\pi}\frac{1-b^2}{b^2} - \frac{I_6}{\pi^2 b^2 (1+b^2)} \tag{3.1}$$

Where

$$I_6 = \int_{-b}^{b} \frac{\ln \dfrac{\sqrt{b^2+1}+\sqrt{b^2-t^2}}{\sqrt{b^2+1}-\sqrt{b^2-t^2}}}{1+t^2} dt$$

$$b = \tan\frac{\alpha}{2}$$

α ~ the angle over which contact occurs on the pin
E ~ modulus of elasticity
ΔR ~ difference in the radii of the cylinders, and
Q ~ force applied to the center of the pin.

Clearly, application of the above solution to gear-hub contact idealizes the hub as a solid cylinder and the gear as a "large diameter" disk with a hole.

3.1.2 Quasi-Static Finite Element Analysis Without Adhesion

The finite element model of the gear-hub contact (Figure 3.1) is based on the gear and hub in the DMS gear train that is closest to the microengine. As in the analytical model, the geometry is simplified to a "pin in a hole," but the plate has a finite outer radius of 92 μm and a thickness of 2.5 μm. The radius of the hole in the gear is 7 μm, and the radius of the sidewall of the hub is 6.7 μm. The outside of the gear is constrained to zero displacement in all directions. Contact is defined between the sidewalls of the hole of the gear and the hub. For this first model the axis of the hub has a prescribed displacement in the negative x-direction that pushes the hub into the side of the hole – the *in-plane model*. The model utilizes symmetry to reduce the size and run time of the analysis and contains one element through of the thickness. The meshes were created with CUBIT [3.2] and the quasi-static analyses were performed with ADAGIO [3.3].

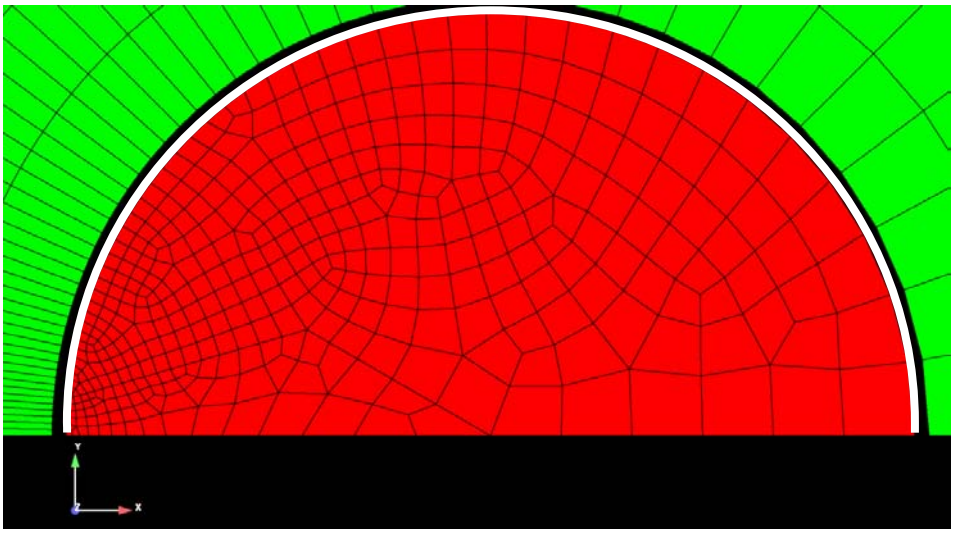

Figure 3.1 Gear-hub mesh with six elements across the first five degrees.

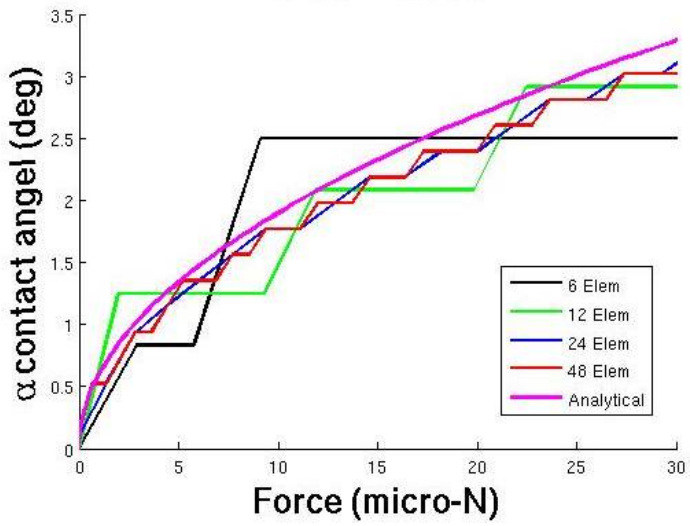

Figure 3.2 Contact angle vs. reaction force for various refinements in the θ-direction.

To determine the sensitivity of the model to the number of elements in the contact region the mesh density in the first five degrees was varied. The results of contact angle *vs*. reaction force (at the hub's center) for models with 6, 12, 24, and 48 elements (edge lengths of 0.1, 0.05, 0.025, and 0.0125 μm, respectively) in this five-degree section are compared to the analytical solution in Figure 3.2. As the number of elements in the contact region increases the contact angle better matches the analytical solution, but refining the mesh in the θ-direction alone is clearly not sufficient. The best numerical results still fall slightly below the analytical results. Decreasing the mesh size in the *r*-direction, to match the mesh size on the contact surface, improves the correlation to the analytical model as seen in Figure 3.3.

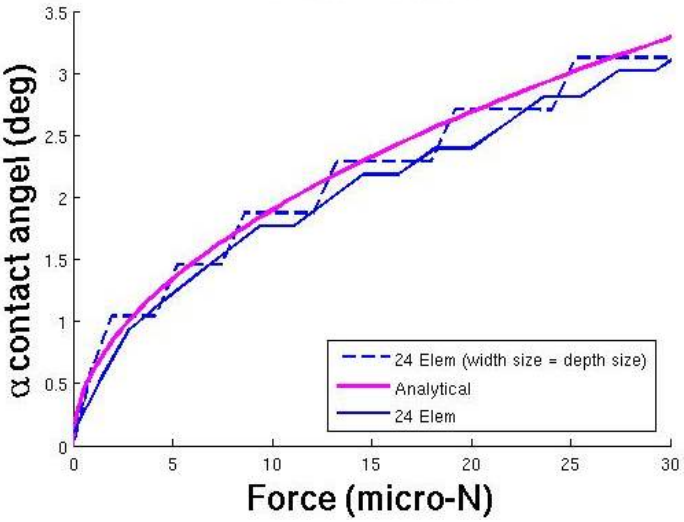

Figure 3.3 Contact angle vs. reaction force with mesh refinement in the radial direction.

The convergence studies described above make it clear that a mesh fine enough to address in-plane contact at arbitrary points within the DMS gear train would require a mesh that is too costly for this study. As is shown below, if we were to allow contact with the gear at an arbitrary orientation relative to the hub, the problem becomes more difficult. To bound the possible orientations of the gear, the maximum tilt (0.8 deg) was used in an analysis with the same boundary and displacement conditions as the in-plane analyses. (The maximum tilt was estimated from the geometrical constraints on the actual gear.) The meshes through the thickness of the gear and hub were modified. The element face length in the thickness direction begins at the same length as in the other two directions then increases as shown in Figure 3.4. The contact area shown at the right of the figure is 0.0717 μm^2 under a force of about 29 μN. Figure 3.5 compares the in-plane and titled contact area *vs*. reaction force.

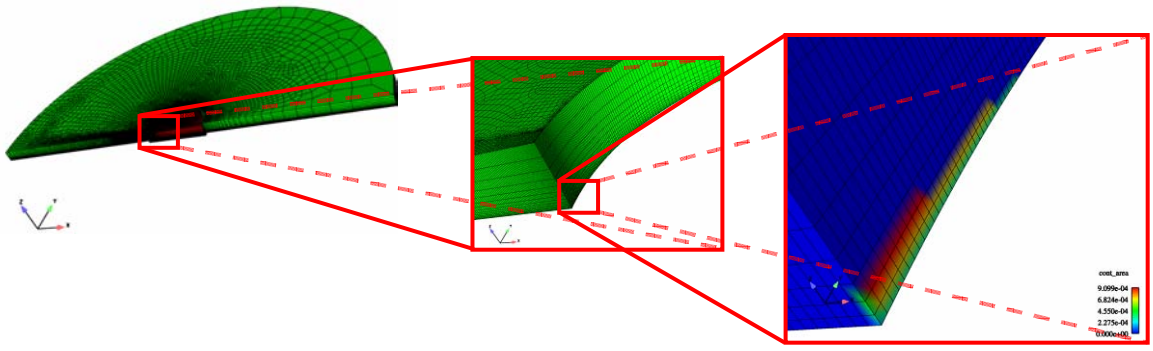

Figure 3.4 Mesh and contact area for the tilted gear.

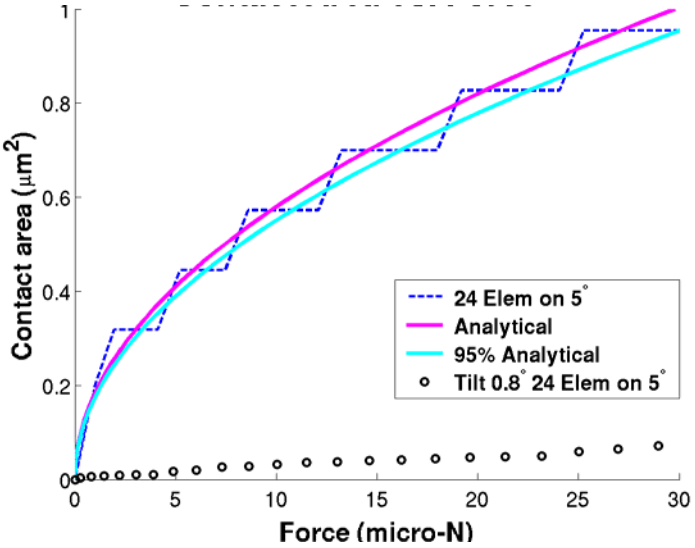

Figure 3.5 Contact angle vs. reaction force, comparison of in-plane results to tilted gear results.

While mesh convergence studies for the z-direction were not conducted, these results lead to the following preliminary observations.

(1) The contact area for the tilted-gear case is nominally an order of magnitude smaller than the in-plane case. Thus even if one were to argue that the asperity density was high enough to justify the idealization of a smooth interface for the in-plane case, the same argument is more difficult to defend for the tilted gear; for this later case, in particular, a few asperities on the surfaces may be dominating the interaction.

(2) The number of elements that would be required to perform an analysis of an entire gear train in motion with arbitrary contact points would be extremely large, if not prohibitive, assuming the contact is to be modeled with high fidelity. While the problem size barrier might conceptually be overcome with adaptive mesh refinement in the contact areas, it appears to be beyond our current modeling capabilities.

As previously discussed, the approach pursued in this study was to use a rigid body dynamic model for the device but to use FEA to estimate the effects of adhesion for the cases where the contact area changes with deformation (*e.g.*, the sidewall contact examined above). In the section below, we examine the effects of adhesion on the in-plane case. In particular the additional normal force created by the adhesion will increase the maximum friction force that can be attained over a contact region.

3.1.3 Quasi-Static Finite Element Analysis With Adhesion

Currently, ADAGIO does not have an adhesion modeling capability that can be applied to curved surfaces. As such, the explicit dynamic code PRESTO [3.4] is applied to this problem by using slow enough loading to minimize dynamic effects. In PRESTO, the adhesion is modeled by using a digitized form of the following traction-separation relationship:

$$t = \frac{A}{6\pi\left(d_{\min} + u\right)^3} \tag{3.2}$$

where

$d_{\min} = \sqrt{\frac{A}{12\pi\Gamma}}$, minimum separation distance
A ~ Hamaker constant ($5\text{x}10^{-20}$ Joules)
Γ ~ adhesion energy
u ~ normal separation from the contact state
t ~ traction

Equation (3.2) is obtained from the parallel plate relationship presented in [3.1]. The addition of d_{min} is a modification that prevents t from being unbounded and more importantly allows the adhesion energy to be prescribed. The actual surface has some roughness, and thus d_{min} can be thought of as an "effective separation" that exists when rough surfaces are in contact.

Figure 3.6 and Figure 3.7 depict the traction-separation relationships for total adhesion energies of 10 and 1700 $\mu J/m^2$, respectively. These values were the bounds obtained for the adhesion energies from the exposure tests of Chapter 2. The smaller value corresponds to an unexposed, control case.

The actual implementation of the digitized models must pass through the origin for Presto; thus, though not depicted in these graphs, the actual models had a very steep, linear ascending region that connected the origin to the maximum traction. The actual value of d_{min} thus differed from that given by the expression above to account for the energy associated with the "linear ascent." Because PRESTO requires the adhesion model to give zero tractions at initial contact, PRESTO will not predict the additional normal traction that results in the contact region due to adhesion in the contact region. It does account for the additional normal traction that occurs in the contact region due to the tractions in the near-contact region. To account for the adhesion acting over the contact region, one can calculate the additional normal force from the product of the contact area and the maximum adhesion traction – treating the linear ascending part of the response as merely a computational requirement of Presto that the response pass through the origin.

These adhesion models were applied in PRESTO to a simpler device for which start-up failures were quantified. The device is the TRA with a single resistance gear as discussed in Chapter 2. The adhesion model was applied to estimate the normal force between the small gear and its hub due to adhesion alone. The initial position corresponded to the gear and hub touching along a vertical line (*i.e.*, the in-plane case). The hub was free to move, and thus the adhesion tractions pulled the two sidewall surfaces into additional contact. The calculated adhesion forces and contact areas for these two adhesion energy cases are given in Table 3-1.

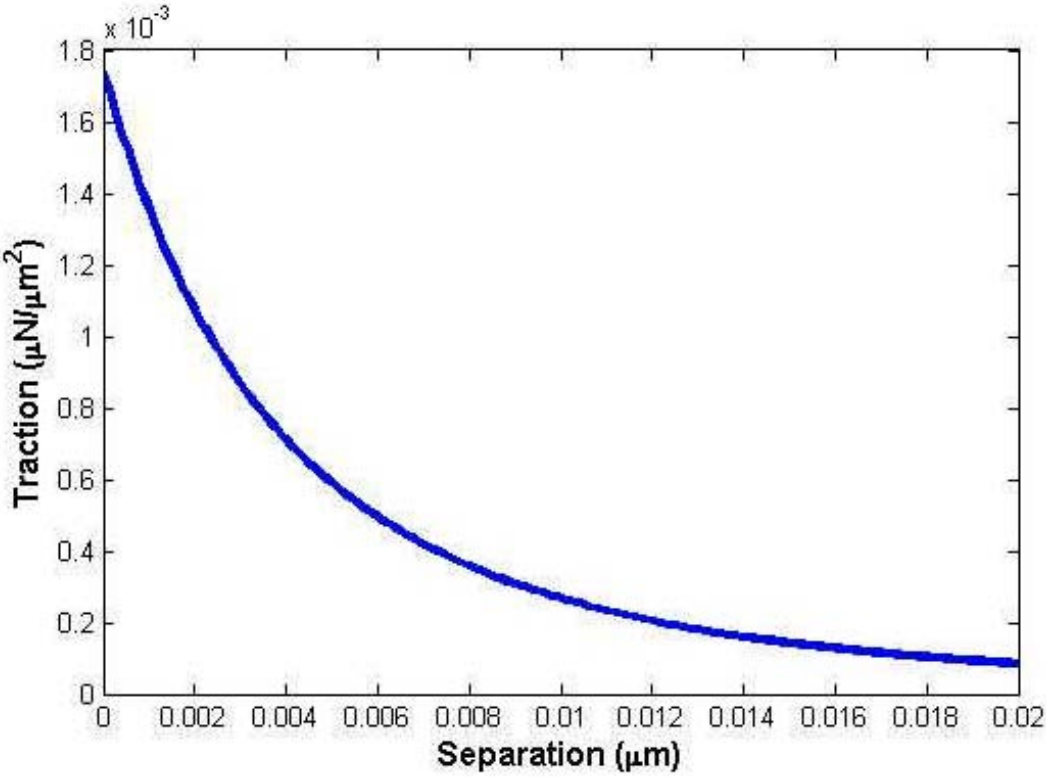

Figure 3.6 Traction vs. separation for 10 μJ/m^2.

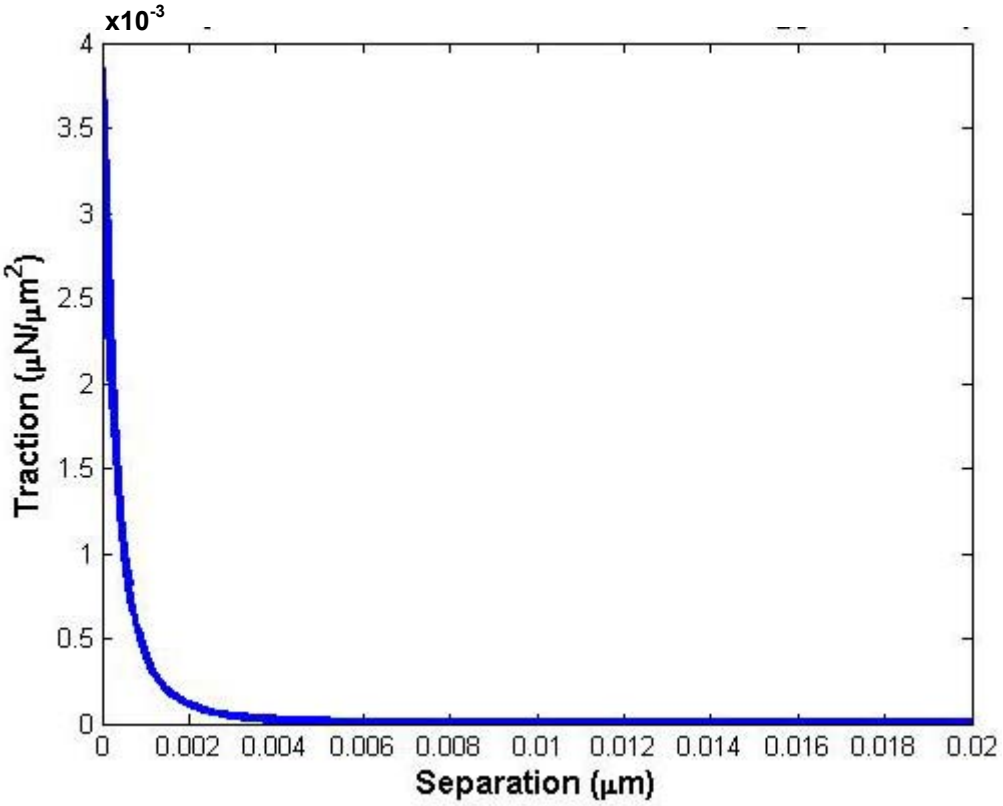

Figure 3.7 Traction vs. separation for 1700 μJ/m^2.

Table 3-1. Cylinder-cylinder contact results for two adhesion energies.

Γ ($\mu J/m^2$)	Contact Area (μm^2)	t_{max}[1] ($\mu N/\mu m^2$)	Normal force due to contact adhesion[2] (μN)	"Normal force" in Presto[3] (μN)	Normal force Total (μN)
10	0.02545	0.001692	0.00004307	0.00625	0.00629
1700	0.2291	2.790	0.6391	2.999	3.638

(1) These values differ with those depicted in Figure 3.6 and Figure 3.7 because the models for Presto include an initial elastic slope, as discussed earlier.
(2) Product of the contact area and t_{max}.
(3) Actually the x-component of the resultant force on the contact surface.

Note that in both cases the normal force is dominated by the contribution of the adhesion in the near contact region. These normal forces are used in the next section to estimate the resistance to start-up using a simple "hand calculation." However, one must keep in mind that each contribution is dependent upon the traction-separation relationship that is used.

While not addressed in this report, an approach was devised that would allow FEA results with adhesion to be included for dynamic analyses. Essentially the FEA would be used to provide empirical data on contact with adhesion. Functions to represent this data would then be used to estimate the additional normal force that would occur in contact with adhesion present. In this study, we apply the same ideas but to individual static states.

3.2 Rigid Body Dynamics Modeling of Devices

While the FEA could be used to examine contact response, RBD modeling allows idealized models of complete devices to be examined. Unfortunately surface interactions in RBD models are treated in a simplified manner and yet are very important in predicting the behavior MEMS devices. The RBD models were developed using LMS Virtual.Lab Motion software [3.5], which allows a user to modify a subroutine that affects the contact interaction. For brevity, the software will be referred to simply as LMS in this report.

Two devices were modeled in this effort: (1) a simplified model of a DMS gear train, and (2) a more detailed model of the TRA-resistance gear device. This section presents information on how MEMS geometry was imported into the RBD code, how contact was modeled, and some initial results that incorporate the effects of adhesion.

3.2.1 Importation of MEMS Geometry

The geometry of the hub was based on devices fabricated from the SUMMiT V process using a pin joint cut. The geometry file was based on the AutoCAD layout of RS 424. The 3D geometry file was created using the 3D Modeler software added by Sandia to the

framework of AutoCAD. The ACIS format file titled Filename.sat was read into Solidworks. Within Solidworks, the file must be scaled and is saved as a parasolid of file format filename.x_t. LMS can import parasolid geometry.

LMS uses a consistent set of units for all internal calculations. Within the solution set dialogue, the calculation units can be chosen. The model dimensions can be displayed and queried in any units based on choices made in the tools/options menu. However, the graphics are limited to showing features of 1 micron or larger. Therefore the geometry was scaled by a factor of 1000 before the .x_t file was imported into LMS. The units in which LMS calculates the solution are meter, kilograms, seconds, Newtons and Pascals. In the model, the dimension of microns was translated into millimeters because of this scaling factor of 1000. Therefore the units displayed in LMS must be mapped to the following units: millimeters, milligrams, seconds, nanoNewtons, and milliPascals, respectively. This mapping is shown in Table 3-2.

Table 3-2. Mapping of units to LMS.

	LMS input/output units	Real world units
Length	meter	millimeter
Mass	kilogram	milligram
Time	second	second
Force	Newton	nanoNewton
Pressure	Pascal	milliPascal

3.2.2 DMS Gear Train Model

The Discriminating Micro Switch (DMS) consists of a gear train driven by a microengine as shown in Figure 3.8. The first gear of the gear train is pulled by arms in perpendicular directions as seen in Figure 3.9. Contact forces cause wear on the hub and gear surfaces. The load on the first gear is a function of the friction and adhesion that must be overcome on each gear-hub interface. This model was created with the gear-hub interactions defined as joints. The joint definition is a mathematical constraint and does not account for wobble, friction, or adhesion. As joint definitions were replaced with contact definitions, the model became more realistic and more time-consuming to troubleshoot and to solve. After the simplified model was created and during the course of adding contact definitions, the focus of the experiments shifted from the DMS gear train to the TRA-resistance gear device. Therefore only intermediate results were obtained from this model before beginning work on the TRA model.

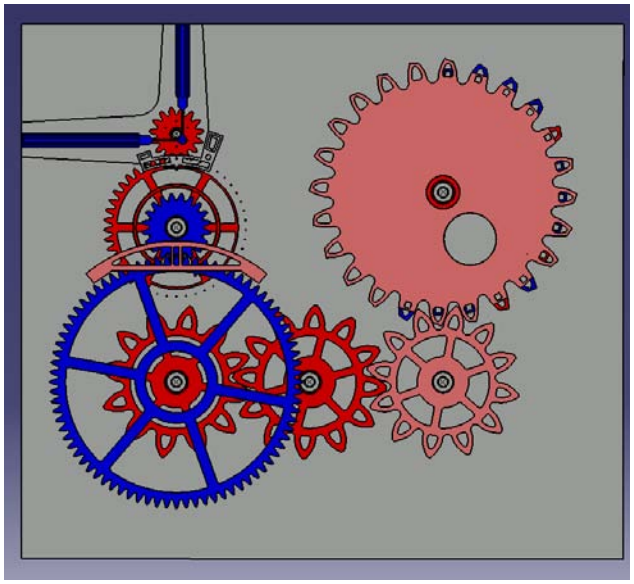

Figure 3.8 Top view of DMS gear train model.

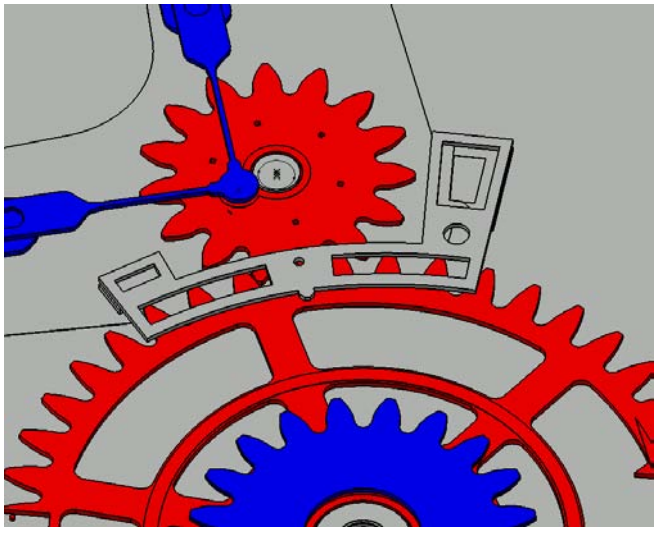

Figure 3.9 Detail view of first gear of DMS gear train.

3.2.3 TRA-Resistance Gear Model

The TRA-resistance gear device consists of a torsional ratcheting actuator (TRA) that loads a typical drive gear. The small drive gear is loaded by a beam that must bend for the gear teeth to pass by. The device is depicted in Figure 3.10 and Figure 3.11. The large blue ring represents the outer ring of the TRA, the drive gear is red, and resistance beam is green.

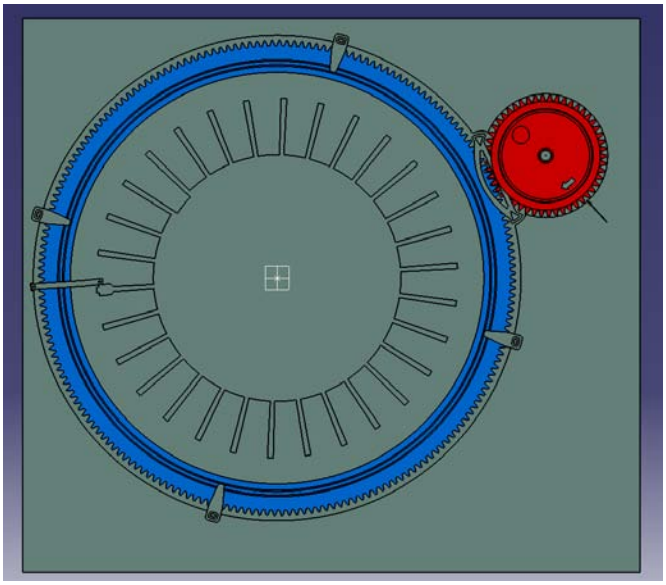

Figure 3.10 Top view of TRA-resistance gear model.

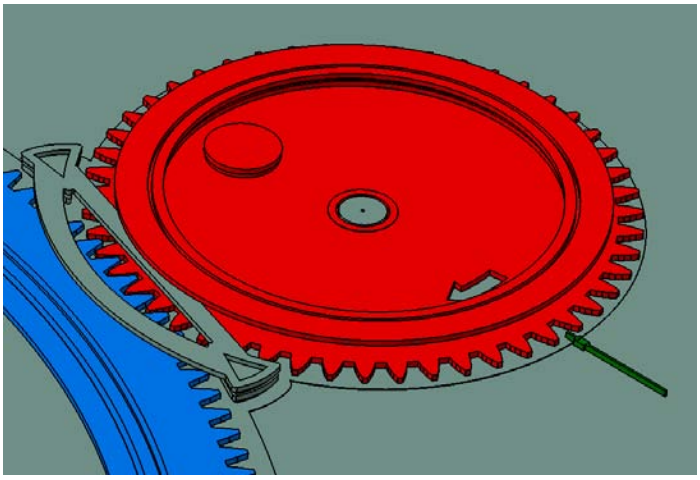

Figure 3.11 Detail view of gear and resisting beam.

The model is defined by importing geometry, creating bodies from the geometry and adding necessary features to create forces, constraints, joints and drivers. The approach taken in this model was to create idealized constraints and joints. Then as more contacts were added, joints were disabled and eventually deleted, allowing the contacts to enforce the "connections." Much time was spent debugging the model during each step.

LMS can only model point contact, and from a practical point of view each contact pair must be defined *a priori*. Options exist for sphere to sphere contact, sphere to revolved or extruded surface contact, and extruded surface to revolved surface contact. However, the surfaces must have curvature such that contact only happens at one point. Line contact or contact at multiple points of a contact pair will cause the contact algorithm to fail. While only point contact can be modeled, many discrete contact sets can be used to approximate continuous contact, which is the approach taken in this study.

Thirty-three contact pair definitions are used to model the gear-hub interface. There are eight spheres equally spaced around the inner hole of the gear like the one shown in Figure 3.12. The sphere diameter represents the gear thickness and interacts with the hub surface above and below the sphere. These spheres interact with the hub surface above and are repeated to interact with the hub surface below the gear. There are also eight spheres along the edge of the upper hub ring that interact with the top surface of the gear and similarly eight spheres along the lower hub ring which interact with the bottom surface of the gear (Figure 3.13).

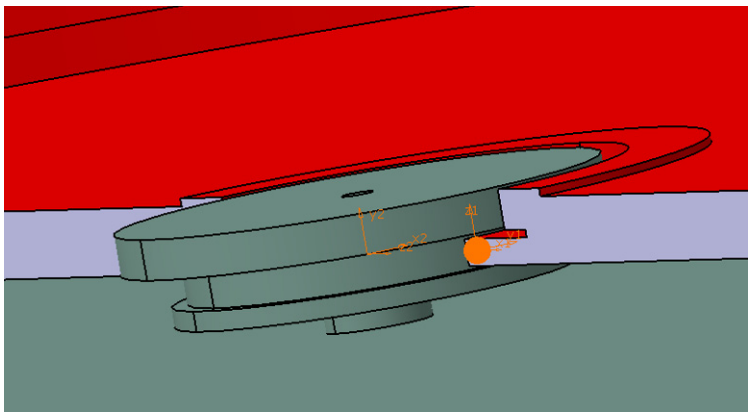

Figure 3.12 Detail view of hub and cross section of gear. Orange sphere used for contact definition and interacts with the lower surface of the hub.

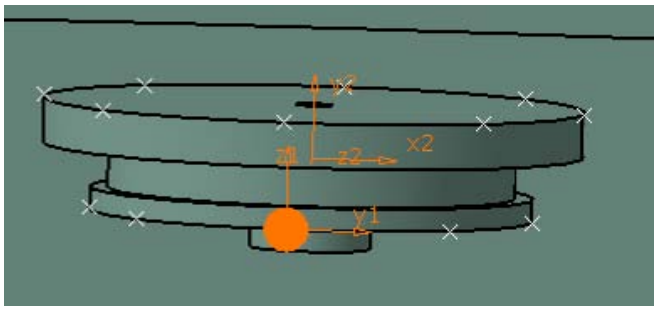

Figure 3.13 Detail view of hub. Each x marks a contact sphere location. Highlighted orange sphere used for contact definition and interacts with surface on the bottom of the gear.

Lastly, there is one sphere in the center of the hub that interacts with the cylindrical surface of the gear's inner hole. This last contact set makes the simulation very slow, on the order of days instead of minutes. To reduce calculation times, an idealized cylindrical joint is used. The contacts on the bottom surface of the hub support the weight of the hub, but the gear is forced mathematically to stay centered along the axis of the hub.

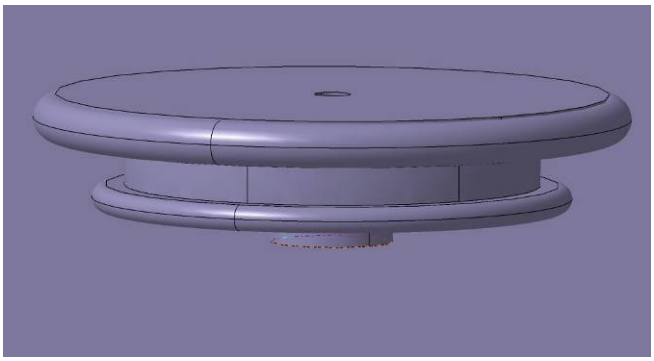

Figure 3.14 Detail of alternative contact definition. Toroids define edges of hub.

An alternative modeling approach for the gear-hub contact was tried (Figure 3.14), but solution times were excessive. The contact between the hub and the gear that restrict vertical motion was achieved by revolving circles that formed toroids around the outside edge of the hub. Flat sections on the top and bottom of the gear make up the other side of contact with the toroids. Contact spheres were placed so that the flat sections would hit them just before hitting the toroid forcing the flat sections to tilt and only touch the toroids at one point. There was also a contact set that kept the gear centered on the hub using a cylindrical extruded surface for the hub cylinder and a revolved surface with a large curvature for the surface of the hole in the gear. With this approach, a total of five contact sets could be used to capture the behavior of the gear-hub interface.

Friction is an important factor in modeling the start-up behavior of a device. LMS defines the coefficient of friction in terms of the sliding velocity as

$$\mu_{act} = \mu_{nom} \tanh\left(\frac{5v_{slide}}{2v_{trans}}\right) \tag{3.3}$$

where

μ_{act} ~ the actual coefficient of friction used in the calculations
μ_{nom} ~ the nominal coefficient of friction
v_{slide} ~ sliding velocity
v_{trans} ~ transitional velocity

Note that this functional form is defined so that the coefficient of friction is zero when the sliding velocity is zero, thus static friction is never calculated; the contact must be sliding for any frictional force to be calculated. (This does not pose a problem in the start-up calculations as formulated here, because as discussed below the TRA ring is under displacement control.) The form also accounts for the frictional force being opposite to the direction of motion via the sign of the coefficient of friction. A smooth function is required for stability of the solution. When a step function between negative and positive μ was programmed into the contact user-defined subroutine, the model failed.

The input for this model is the angular displacement (as a function of time) of the large outer ring of the TRA. The displacement represents the 2.25 degree ratcheting motion of a TRA driven by a 60 Hz square wave and was modeled by a cubic spline function

(Figure 3.15). With the model under displacement control, the start-up failure criterion is: a reaction torque that exceeds that of the TRA (as measured by the normal force on the gear teeth).

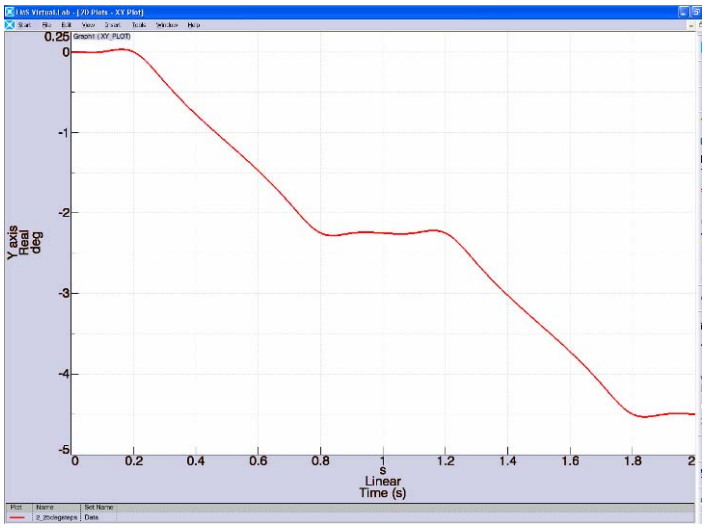

Figure 3.15 Graph of input rotation of TRA gear.

In LMS, the adhesion is only added after contact occurs; it does not pull two bodies in close proximity into contact. When contact is detected the user subroutine is called to calculate a normal force and a friction force. The subroutine bases calculations on inputs from each contact definition. The variable defined in LMS for contact spring stiffness is not necessary for our models because the stiffness is accounted for by the Young's modulus of the materials in contact. Therefore, this variable was chosen to pass the adhesion area into the subroutine. The adhesion area was calculated for each contact based on either geometry or FEA results. The adhesion traction values ranged from 0 to 3849.3 $nN/\mu m^2$, which are based on an adhesion energy range of 0 to 1700 $\mu J/m^2$. The adhesion force is calculated as the product of the adhesion traction and the adhesion area. The adhesion force is added to the normal force only for the sake of calculating the frictional force. The user subroutine for adhesion force at contact points is based on the subroutine available within LMS for contact force. The purpose of the subroutine is to calculate normal and friction forces given the penetration depth, velocity of penetration, sliding velocity, and local curvature of the contact. Normal forces are generated by any combination of the following: linear stiffness and damping factors, non-linear stiffness and damping curves, and Hertzian contact (Young's modulus plus coefficient of restitution). Friction is based upon the normal force, nominal friction coefficient, and the ratio between the sliding velocity and a reference velocity (Equation 3.3).

The changes to the subroutine are shown in Figure 3.16 in bold print. Traction values were "hard coded," and one value left uncommented determined the value used for all contacts. The contact area, which can vary for each contact, was input from the contact definition using the spring stiffness variable which otherwise is unused in this model. This variable passed to the subroutine as STIFF is renamed as CONTACTAREA and used to calculate the adhesion force (ADHFRC). The variable STIFF should then be set

to zero or the calculation for the linear spring force must be commented out. The normal force with adhesion (FNORMADH) is calculated and in turn used to calculate the frictional force (FFRIC).

```
c=====================================================================
c           Calculate an adhesion force based on contact area and traction.
c           Use STIFF as variable for passing in contact area info for each adhesive contact.
c           If there is zero contact area, there is zero adhesion.  Use microns squared as
c           units for contact area.  All but one value for traction is to be commented out.
c           Traction is in units of nanoNewtons per micron squared
c     TRACTION=0.0000
c     TRACTION=1.7366
c     TRACTION=2.5741
c     TRACTION=155.33
c     TRACTION=285.36
c     TRACTION=2574.1
      TRACTION=3849.3
      CONTACTAREA=STIFF
      ADHFRC=CONTACTAREA*TRACTION
c   Calculate the normal force, including Hertzian contact force, linear spring force, nonlinear spring force, linear damping
c   force, and nonlinear damping force.
      FNORM = HZFRC + KFRC + CFRC + KCRVFRC + CCRVFRC
      FNORMADH = FNORM - ADHFRC
c   Calculate the two friction forces
      IF (MUCRV .NE. 0) THEN
        XMU = FSPLN(VSLID,0.0D0,MUCRV,INTMU,A,IA,0,0,46,EE)
      ELSE
        XMU = MUNOM * DTANH(2.5D0*VSLID/VEPS)
      END IF
      FFRIC  = XMU * FNORMADH
```

Figure 3.16 Partial listing of user subroutine for contact.

The model was used to examine the effects of adhesion on start-up. Figure 3.17 shows the normal contact force on the gear teeth with and without adhesion. Adhesion significantly increases the force transferred between the gears. Figure 3.18 presents the force on the gear teeth in contact versus the adhesion traction for three values of the coefficient of friction. The models indicate that adhesion forces (as calculated here) are not high enough to impede start-up of the device. The maximum required force of 18.4 μN is much lower than the maximum force output of the new TRA, estimated at 40 μN.

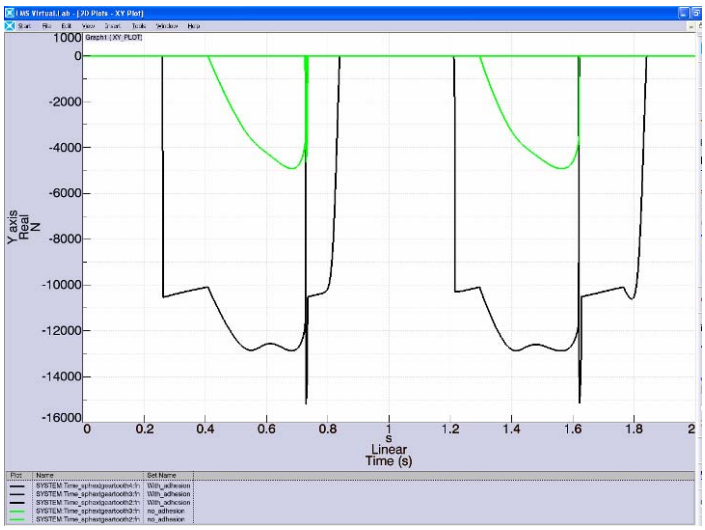

Figure 3.17 Comparison of normal contact force on gear teeth with adhesion (black) and without adhesion (green). The coefficient of friction is 0.3, and the adhesion energy is 1700 μJ/m^2.

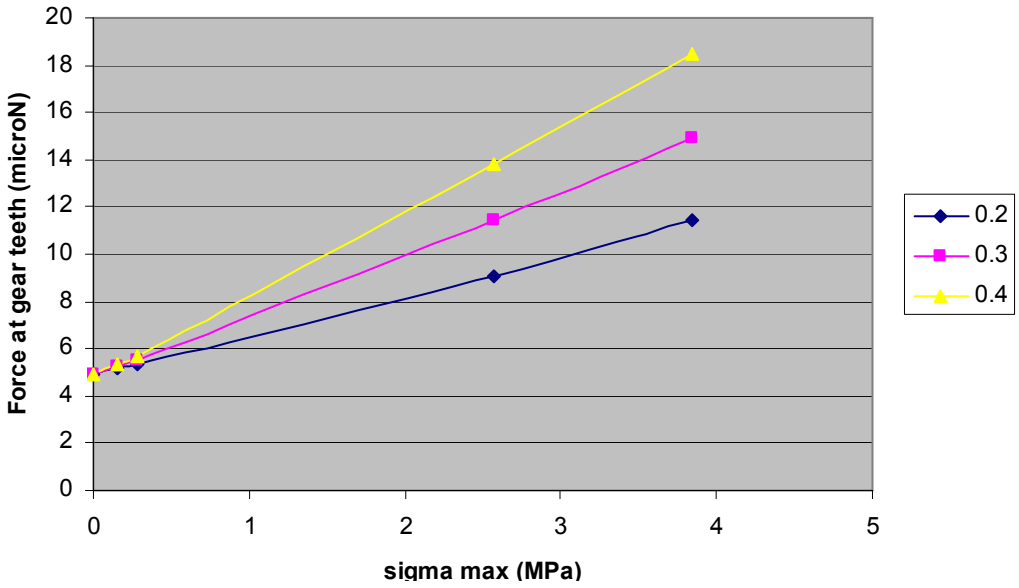

Figure 3.18 Gear tooth contact force vs. adhesion traction (in contact) for three values of coefficient of friction.

As a check on these results, a simple analytical model was solved to determine the range of adhesion tractions and friction coefficients that prevent start-up. Let's again assume that the new TRA will be able to generate a maximum force of 40 μN and that the "contact radius" of the resistance gear is 100 μm. Assume the resistance gear is centered about the hub, so there is no contact on the sidewall and the contact region on the bottom of the gear is a ring. The inner (r_i) and outer (r_o) diameters are of the contact ring are 7 μm and 9 μm, respectively. Now let's take a "strength of materials" approach to determining the frictional resistance due to contact on the ring. Similar to a perfect plasticity model, we can determine the torque required to cause each point on the ring to slide (T_f) by integrating the sliding friction shear traction (τ_f) over the whole ring.

$$T_f = \int_{r_i}^{r_o} 2\pi\tau_f r^2 dr = \frac{2\pi\tau_f}{3}\left(r_o^3 - r_i^3\right) \tag{3.4}$$

Assuming that adhesion is the only contributor to the normal traction, the sliding friction traction can be related to the adhesion traction (t_{max}) by Coulomb's law: $\tau_f = \mu\, t_{max}$. Substituting this relation into Equation (3.4) and equating it to the torque applied to the gear by the TRA (40 μN x 100 μm) gives

$$t_{\max} = \frac{3000}{193\pi\mu} MPa \tag{3.5}$$

Figure 3.19 shows a plot of this relation and boxes denoting ranges of interface parameters for the three exposure states. For all exposure states, the simple model indicates the devices will startup. The experimental results yield mixed results for all exposure states – some devices start up and others do not. To estimate the added contribution that sidewall adhesion might have, let's examine the additional torque that could be created by friction on this surface. Using the normal force given for the extreme exposure case in Table 3-1, a moment arm of about 6.8 μm, and a coefficient of friction of 0.3 yields a torque that is less than 0.2% of the torque generated by the TRA.

3.3 Conclusions

While there are many simplifying assumptions used in the device models, the fact that experimental results include many devices that fail to startup is an indication that adhesion modeling only based upon values of adhesion energy from cantilever beams is inadequate. An obvious potential weakness of the modeling approach taken here is that the adhesion tractions were obtained by assuming the traction-separation relationship for a parallel plate is applicable (in a truncated form). Traction-separation data for surfaces with representative roughnesses could provide more complete information. Another uncertainty is whether the adhesion energies of the cantilever beams are representative of those that exist in the actual device. Material deposition that bridged initial gaps was observed in the TRA-resistance gear device that potentially inhibits start-up more than the adhesion model indicates. Advances were made in our ability to model MEMS devices, but additional combined experimental-modeling studies will be needed to advance the work to a point of providing predictive capabilities.

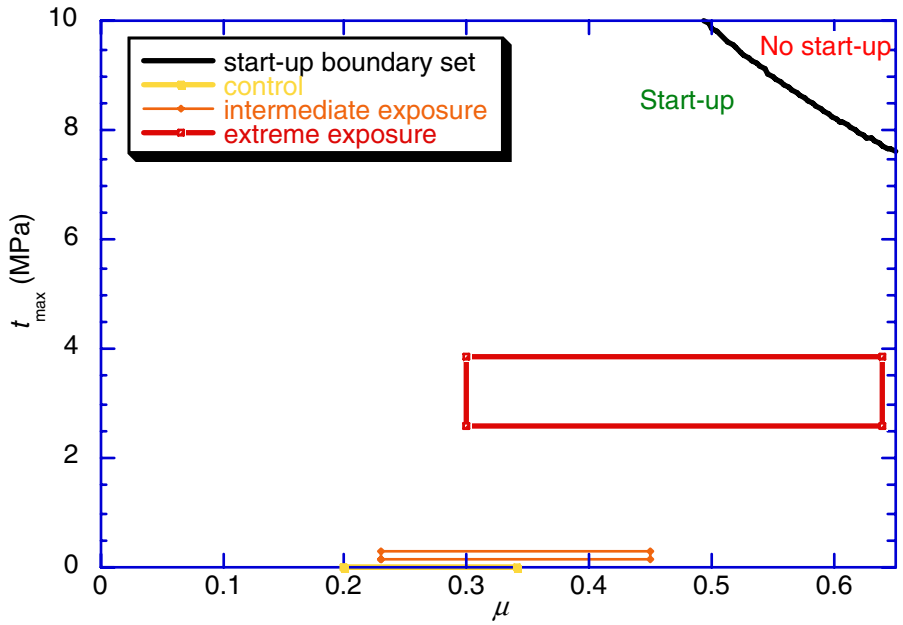

Figure 3.19 Start-up states for ranges of adhesion tractions and coefficients of friction.

Chapter 3 References

3.1. Persson, A. (1964). "On the Stress Distribution of Cylindrical Elastic Bodies in Contact," J. Israelachvili (1992). Intermolecular and Surface Forces, 2nd ed., Academic Press, p. 450.

3.2. S.J. Owen, "CUBIT 10.0 Mesh Generation Toolkit User Documentation." Ph.D. Dissertation, Göteborg, Sweden, Department of Mechanical Engineering, Chalmers University of Technology (2005), p. 147.

3.3. J.A. Mitchell, J. Hales and K. Pierson "Adagio/Andante User Documentation," (2003).

3.4. J.R. Koteras, A.S. Gullerud, N.K. Crane and J.D. Hales "PRESTO User Documentation" (2005).

3.5. LMS International, "LMS Solutions Guide LMS Virtual.Lab Motion," (2004).

4. Packaging

4.1 Introduction

Packaging of MEMS devices is an important enabling capability for the Science of Dormancy LDRD for three main reasons. First, in order to test the shear number of parts efficiently the MEMS devices would need to be placed in a ceramic dual in line (DIP) package to quickly change from part to part and not use electronics probes. Second, all of the devices would need to see a set of packaging processes that are not only consistent across all of the test vehicles, but representative of the way they would be handled and packaged as in a real product. Three, before this project there were no consistent and practiced means or guidelines by which MEMS devices should be handled and processed after the MEMS device release step. Therefore it was a necessity to formalize a set of baseline packaging processes for SUMMiT-V devices.

The following pages show the process flow and describe the improvements made to the packaging process to enable high yield of MEMS parts. The following sections address six main areas (1) die attach epoxy and dispense, (2) automated die placement, (3) die attach epoxy curing, (4) automated wire bonding, (5) application of low temperature glass lids and (6) a recap of the entire packaging process.

4.2 Die Attach Epoxy and Dispense

4.2.1 JM7000

JM7000 is an electrically conducting, silver filled, one part epoxy manufactured by Emerson and Cumming. JM7000 was chosen to be the epoxy of choice at SNL for WR electronics die attach in 1998 after an exhaustive study of COTS epoxies in FY96-FY97 ("SECS Adhesive Evaluation Report" Garrett. S. and Conley, B. et al). It was found in the study that JM7000 produced the least outgassing of water and ammonia (known contributors to failure of electronic circuitry and mechanical connections such as wire bonds) over time in hermetically sealed volumes compared to all of the other epoxies tested. JM7000 is also regarded as a "space qualified" epoxy. MEMS packaging borrows heavily from electronics packaging at SNL, so JM7000 became the standard for die attach and was used exclusively for die attach in the Science of Dormancy test modules.

4.2.2 Automated Epoxy Dispense

Packaging at SNL is traditionally an intensely manual process due to the small quantities and short-run production nature of SNL product lines. Until about 3 years ago there was little reason to change to automated means of epoxy dispense, die placement and wire bonding as these methods were reserved for commercial packaging houses producing millions of components per year.

In the case of the Dormancy LDRD the need for consistency in packaging processes combined with the regular need for quantities of 100's parts per month regardless of the packaging technologist(s) available drove the need to develop and adopt an automated epoxy dispense capability on the Palomar 3500II automated assembly cell (Figure 4.1).

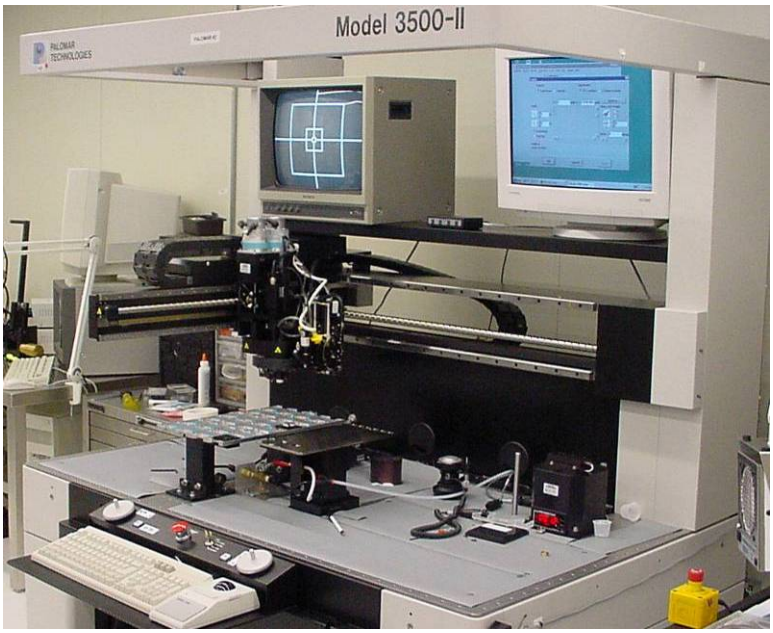

Figure 4.1 Picture of Palomar 3500II automated assembly cell.

The first attempts at die attach used the stock auger style pumps (Figure 4.2 a). These pumps were very difficult to clean and required a great deal of attention when used with JM7000 to prevent the pumps for clogging and internal components from sticking together. The auger style system was replaced by a pneumatic dispense system (Figure 4.2 b).

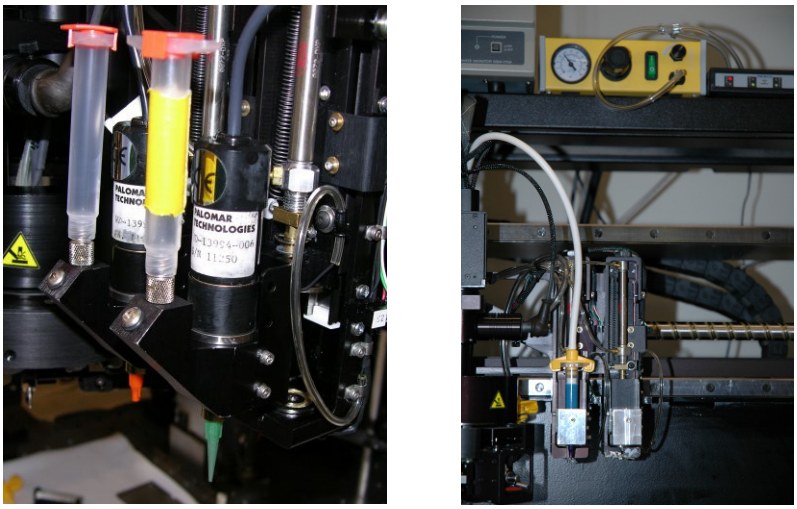

(a) (b)

Figure 4.2 Close-up of auger pump (a), and pneumatic dispense system (b) with yellow controller box and custom made epoxy syringe holder.

This system was essentially a pneumatic controller used with manual dispense hooked up to the electronics of the 3500II and triggered seamlessly through the standard 3500II machine interface. This system was able to produce very consistent epoxy applications and was used during the last year and a half of the science of dormancy project.

4.2.3 Automated Die Placement

Aside from the production speed and part volume required was the need for a fast, particulate free, high precision placement of the MEMS device in the package well across the complete set of parts. Manual means of die placement are less accurate than a machine (10+mils manual vs. 0.5mils by machine). Tweezers used in manual die placement can also produce particulates as the die edges can chip off that can jam MEMS devices. Therefore an automated, particulate free means of die placement was required.

To achieve this, specially designed vacuum tools were used on the Palomar 3500II (Figure 4.3 a and b). These tools land on the die surface and pickup the die using vacuum ported through the holes on the tool stanchions (Figure 4.3 c).

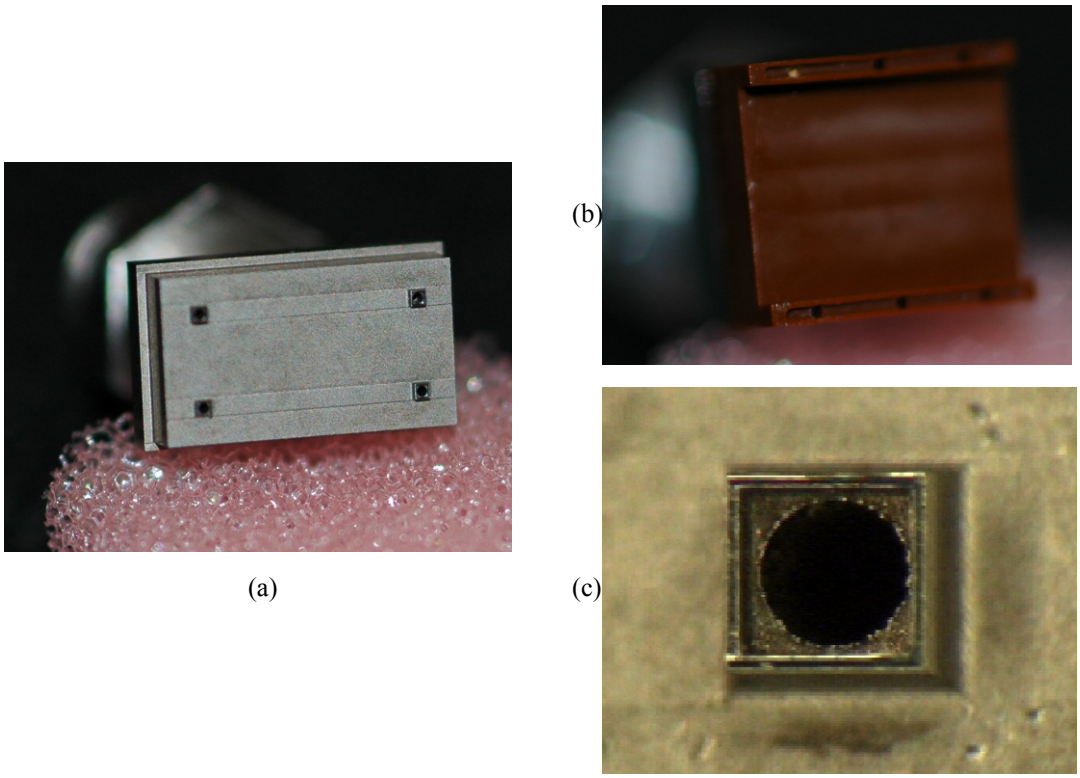

(a) (b) (c)

Figure 4.3 Single mod tool (a), double mod tool (b), and close-up of vacuum hole in tool stanchion (c).

4.2.4 Cleanliness of JM7000 during cure

Early on in the Science of Dormancy LDRD there were a number of failures that occurred after the die attach cure cycle. It was speculated that the epoxy may be outgassing during the cure cycle and that the outgassed material could be settling on the die and somehow modify the surface chemistry to make the MEMS devices more apt to fail.

To verify this, several samples of JM7000 were cured at 150ºC for 30 minutes in an oven. Nitrogen was circulated through the oven and into a mass spectrometer where it was sampled and tested for other compounds (Figure 4.4).

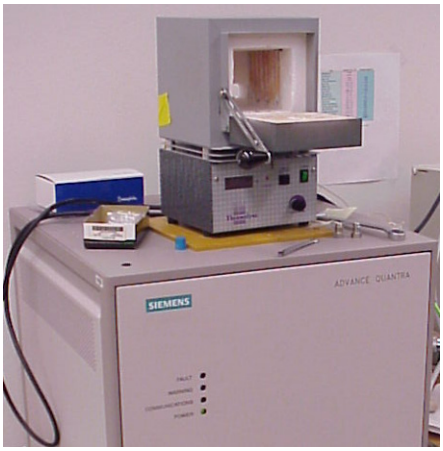

(a)

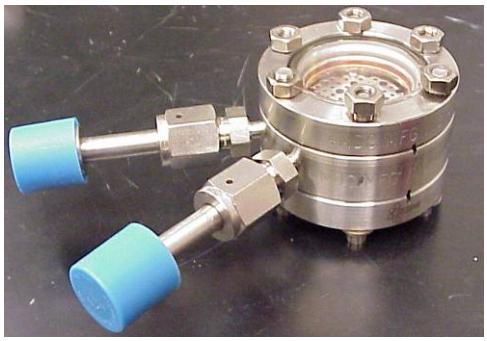

(b)

Figure 4.4 Oven and mass spectrometer (a) and custom sample manifold (b) to allow sampling atmosphere during epoxy cure.

During these tests there was no evidence of water or any other compound, within the resolution of the instrument, that was a by-product of the curing process of JM7000, establishing that outgassing of the die bond epoxy during curing is not a significant source of contaminants inside packaged MEMS.

4.2.5 Curing JM7000

The mass spectrometer tests essentially ruled out JM7000 itself as a potential source of surface contaminates during cure. The other likely source was the oven itself that was used to cure the epoxy after die attach. The original process used a clean room convection oven. Parts were placed in a loosely covered stainless steel container and placed in a preheated, nitrogen purged oven. The oven however was relatively large and had a vent in the back of the oven. Even though there was a nitrogen purge in the oven, there was no way to guarantee that the environment inside was dry, oxygen and particulate free. To ensure that the environment was truly dry and inert a vacuum oven was employed (Figure 4.5).

Figure 4.5 Vacuum oven used for curing epoxy.

The vacuum oven with vacuum pump provided a closed, air tight system that could be purged with nitrogen and continuously bled with nitrogen to prevent the infiltration of oxygen and remove surface adsorbed water. Using the vacuum oven provided complete control over the cure atmosphere producing more consistent results with fewer failures at post die attach functionality testing.

4.3 Automated Wire Bonding

To achieve the speed and accuracy of wire bonds (placement, loop height and bond force parameters) automatic wire bonding was used on the Delvotek 6400 Automated Wedge Bonder (Figure 4.6 a). Aluminum pads on the die are conducive to using 1mil diameter aluminum wedge-wedge bonds (Figure 4.6 b).

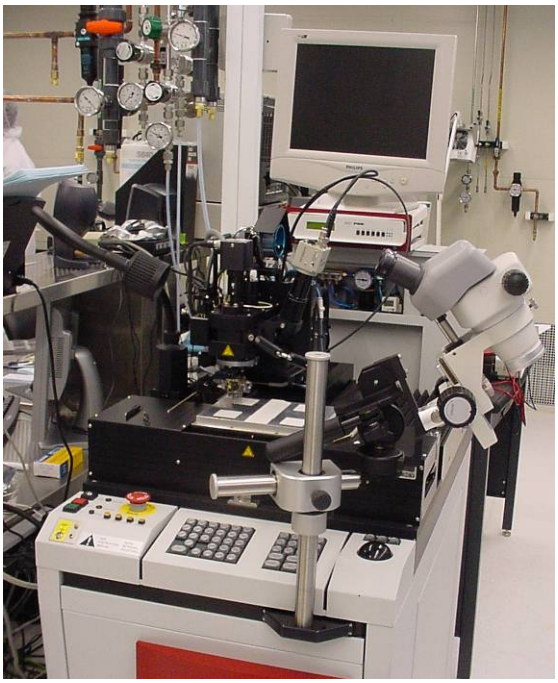

(a)

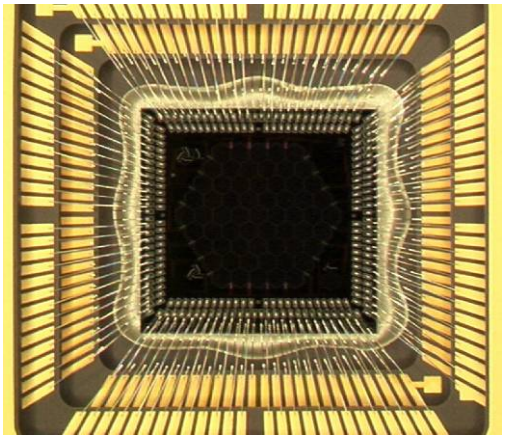

(b)

Figure 4.6 Delvotek 6400 Automated Wedge Wire Bonder (a) used for making Al wedge-wedge wire bonds (b).

During the wire bonding development process, it was noticed that the wire stay slip on the back of the tool (Figure 4.7 a) would interfere with the package edge during normal die to package wire bonding operations. The bonding direction was reversed (package to die), however this made the low part of the loop com in contact with the edge of die. This contact would create and electrical short between the wire and the die, causing some components on the die to not work (Figure 4.7 b).

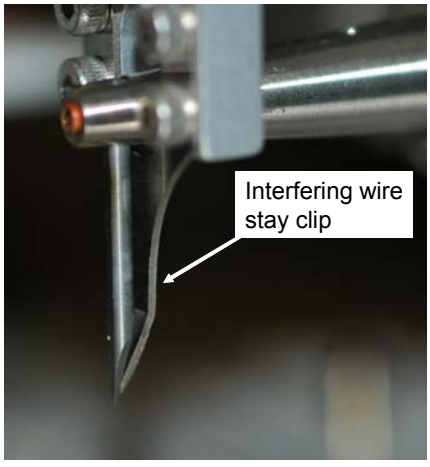

(a)

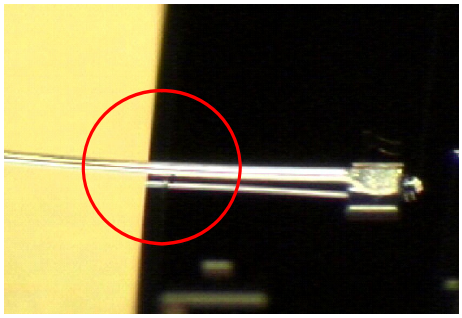

(b)

Figure 4.7 Wire stay slip that would interfere with package (a). Shorting of bond wire to a top poly layer caused some TRA's to not work properly (b).

The issue of shorting was corrected on parts where it was a problem by pulling up the appropriate wires using the Dage wire pull tester. This eliminated the short and allowed the device to work properly.

The long term solution was to remove the wire stay clip from the bond tool (Figure 4.7 a). By removing the wire stay clip, wire bonding could be performed from die to package without interference with the bond tool which places the tallest part of the wire bond loop over the die edge.

Using automated wire bonding with aluminum wire on aluminum MEMS bond pads, approximately 1000 wire bonds would be placed with only 2 reworked bonds per 1000 with average pull strengths of 6grams.

4.4 Application of Low Temperature Sealing of Glass Lids

The most challenging requirement for packaging for the science of dormancy LDRD was to create a glass lid sealing process with the following requirements:

- Hermetically sealed at a temperature lower than 280ºC
- The glass had to have an index of refraction of 1.5 or less.
- A means to introduce a specific gas and water environment into the package.

It turned out that this was too difficult to achieve on the limited time and budget under the LDRD. Therefore a solution of using hermetically sealed tube chambers was developed (explained in section 2). Although the complete lidding process was not successful, a great deal was learned about lid sealing at low temperatures.

4.4.1 Solders for lid sealing

Solders can either require flux or not require flux (fluxless). Flux does not eliminate or chemically remove oxides, it merely moves them out of the way and prevents new oxides from forming that would impede the solder reflow and bonding process.

In the MEMS world it has been shown that MEMS devices need to be handled and packaged in as close to pristine environment as possible. Water, particulates, ammonia, carbon and essentially any material that is foreign to the MEMS construction material system raises the possibility of device failure. To reduce the possibility of introducing materials that will complicate the MEMS device lifetime performance all lid sealing methods had to be fluxless.

There are only two truly fluxless lid sealing solders – 80% gold, 20% Sn (80Au20Sn melts at 280ºC) and 80% gold, 20% germanium (88Au12Ge melts at 356ºC) others generally require some type of flux. Table 4-1 shows the melting points for common solders.

Table 4-1. Properties of Common Solders

WAM Solder	Nominal Composition	Solidus		Liquidus		Density (g/cc)	Electrical Conductivity (% of IACS)	Thermal Conductivity (W/m*C)	Thermal Coefficient Of Expansion (Micro in/in/C) (20C)	Tensile Strength (psi)
		F	C	F	C					
WS96	30Pb, 18Sn, Bi52	205	96	205	96	9.58	3.2	15	38	3200
WS118	48Sn, 52In	244	118	244	118	7.3	11.7	34	20	1720
WS143	3Ag, 97In	290	143	290	143	7.38	4.5	73	22	800
WS145	58Sn, 42In	244	118	293	145	7.3	11.2	33	31	5900
WS149	5Ag, 15Pb, 80In	288	149	300	149	7.85	6.7	43	28	2550
WS157	100In	315	157	315	157	7.31	5.6	82	24.8	575
WS174	30Pb, 70In	329	165	347	174	8.19	8.8	38	28	3450
WS179	2Ag, 36Pb, 62Sn	354	179	354	179	8.41	11.9	42	27	6380
WS181	37.5Pb, 37.5Sn, 25In	273	134	358	181	8.42	7.8	23	23	5260
WS183	37Pb, 63Sn	361	183	361	183	8.34	11.8	51	25	7500
WS185	40Pb, 60In	343	173	358	185	8.52	7	29	27	4150
WS186	30Pb, 70Sn	361	183	367	186	8.17	12.5	53	27	7800
WS187	2.8Ag, 77.2Sn, 20In	347	175	369	187	7.25	9.8	54	28	6800
WS188	40Pb, 60Sn	361	183	376	188	8.5	11.5	49	21.6	7610
WS199	20Pb, 80Sn	361	183	390	199	7.85	13.8	59	24.5	5800
WS200	45Pb, 55Sn	361	183	392	200	8.68	11.2	48	22.6	6800

The solder alloy 90Sn10Au (eutectic melts at 217ºC) was chosen since it can, under the right conditions of argon plasma cleans and nitrogen atmosphere reflow, be used without flux.

4.4.2 Types of lids and their cost

Glass lids come in two types – framed and unframed. Framed lids are by far the most expensive. Framed lids for small packages start at around $100/ea. Unframed lids start at around $20/ea. Whether one buys a framed or unframed lid is not a free choice as there are engineering considerations that directly drive the lid design choice.

The purpose of the frame is to mitigate the stress that builds up between the glass and the package due to coefficient of thermal expansion mismatch. The amount of stress depends upon the CTE difference between the two materials and the solidus temperature of the sealing solder - the larger the CTE difference and higher the solidus temperature, the greater the stress. This is extremely important since a poor selection of the materials can build up enough stress at the sealed edge to fracture the lid during the cool down cycle

during the lid seal process. Frames are generally made of kovar or in some cases invar. Frames are mechanically drawn and then punched to the correct form. These forming and punching tools are expensive. The glass material is then brazed on to the frame (Figure 4.8 a).

An unframed lid may be used if the designer is lucky enough to have a material set between the glass lid material, package material and the solder that will generate low local stresses at the glass lid edge that will not produce glass failure (Figure 4.8 b).

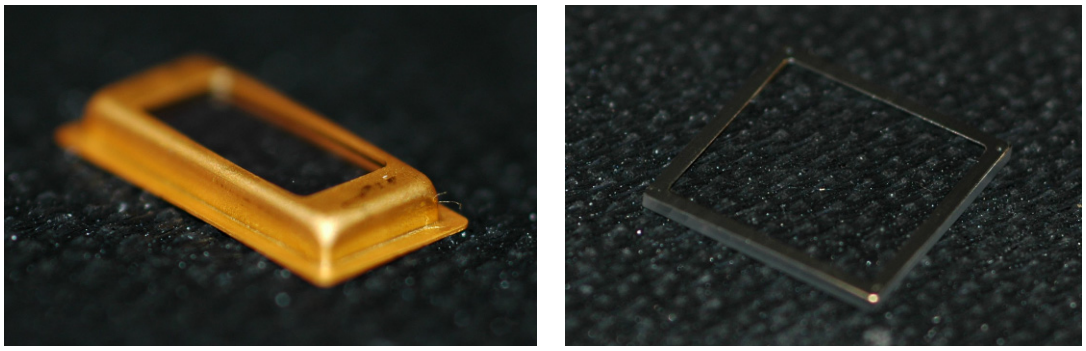

(a) (b)

Figure 4.8 Framed sapphire lid (a) and unframed BK-7 lid with installed preform from Williams Advanced Materials (b).

4.4.3 The tradeoffs in lid design

Since lids that require Kovar frames are prohibitively expensive the only alternative is to make a glass lid that it directly sealed to the ceramic package itself. In order to do this properly it is important that the glass and package coefficients for thermal expansion (CTE) match as closely as possible to avoid building up stress at the glass edge which would make the lid fail (Figure 4.9). This must be done while enforcing a constraint on the glass's index of refraction. Table 4-2 shows a variety of glasses with their index of refraction, modulus of elasticity and CTE's.

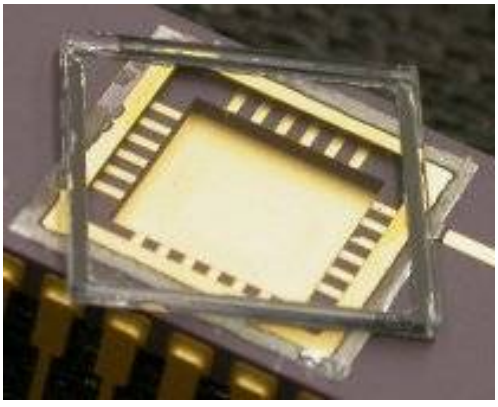

Figure 4.9 Quartz lid failed due to gross CTE mismatch to package ceramic.

Table 4-2. Index of refraction and mechanical properties of common glasses.

Material	Index of Refraction	CTE (um/m/C)	Modulus of elasticity (Pa)
Kyocera A440 black ceramic	Opaque	***7.1***	3.10E+11
Sapphire	1.768	6.05	3.45E+11
Quartz GE214	1.459	0.45	7.00E+10
BK-7	1.509	***7.00***	8.10E+10
Pyrex	1.473	3.25	6.40E+10
Soda Lime	1.523	8.60	7.20E+10

As one can see from Table 4-2 choices are very limited that meet these requirements. BK-7 however showed the most promise. BK-7 VisiLids were ordered from Williams Advanced Materials with Ti-N-Au photo-defined under metal and 90Sn10Au solder preforms tacked on (revisit Figure 4.8 b).

4.4.4 Lid seal process experiments

In theory, these lids should have worked almost out of the box with the right lid sealing temperature profile. While after many experiments and consultations with Williams Advanced Materials an acceptable temperature profile was created that consistently yielded good looking solder reflows (shiny, smooth bead formation – Figure 4.10), there was very little repeatability in the helium fine leak test results that could guarantee hermetic packages. In the end the glass lids were abandoned due to other project time constraints.

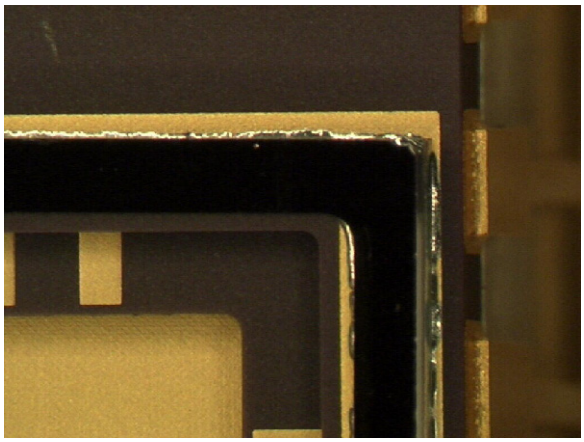

Figure 4.10 A BK-7 lid on 24 pin wide well package appears to be a high quality seal but in reality is not hermetic.

4.5 Finalized MEMS Packaging Flow

Step Number	Process Name	Description	Max Temp and Atmosphere
1	Epoxy defrost	Defrost frozen JM7000 (-40ºC) at room temp.	25ºC, room atm. 40min
2	Package clean (Glen Systems 4a Plasma Cleaner)	All packages undergo a plasma clean in the Glenn Systems 4a Plasma Cleaner immediately before die attach step.	40ºC, dry 100mTorr argon, 400W, 5 min
3	Automated Epoxy dispense and die placement (Palomar 3500II)	1. Operator puts on ESD strap before die handling. 2. Die manually loaded into die holder fixtures on the Palomar 3500II. 3. Cleaned packages loaded into fixtures. 4. Program loaded into computer. 5. Dry run executed. 6. Dispense and placement program executed.	25ºC, room atm.10min
4	Epoxy cure (Blue-M Vacuum Oven)	1. Operator puts on ESD strap before part handling. 2. Preheat the oven to 150ºC, vacuum pump turned on. 3. Parts placed in loosely covered stainless steel vessel. 4. Vessel placed in vacuum oven and the door is closed and locked. 5. Oven manually evacuated (200mTorr). 6. Oven manually backfilled with nitrogen. 7. Nitrogen flow adjusted to sustain a chamber pressure slightly lower than ambient to ensure the door seals stay engaged to the oven housing.	150ºC, 30min, dry N2
5	Automated wedge-wedge wire bonding (1mil round aluminum) (Delvotek 6400)	1. Operator puts on ESD strap before part handling. 2. Load parts into vacuum fixtures. 3. Load program for wirebonding. 4. Perform dry run. 5. Execute bonding program.	25ºC, room atm. 8min
6	Lid cleaning (Glen Systems 4a Plasma Cleaner)	All lids undergo a plasma clean in the Glenn Systems 4a Plasma Cleaner immediately before lid seal step.	40ºC, dry 100mTorr argon, 400W, 5 min
7	Lid sealing (Kovar lids with 80Au20Sn) (SST-1200 Vacuum Reflow Oven)	1. Clean chamber and prebake fixtures according to use instructions. 2. Load cleaned lids perform side up. 3. Operator puts on ESD strap before part handling. 4. Load packages to be sealed seal ring side down. 5. Install load plate and wing nuts.	320ºC peak temp. for 6 min. dry N2

		6. Engage spring pins to 2.3lbs on each package. 7. Install fixture in machine. Install thermocouple. 8. Load program and run. 9. Program executes 3 pump/purge cycles and 1 dewater cycle at 200°C before ramping to reflow temperature.	
8	Lead trim	1. Operator puts on ESD strap before part handling. 2. Parts are placed in shearing device. 3. Leads are trimmed. 4. Lidded parts are put in box with anti-static foam. 5. Non-lidded parts are not put in foam only in anti-static container.	25ºC, room atm. 5min

4.6 Packaging Conclusions

Many improvements were made to the standard packaging process for MEMS devices. There was no single "magic bullet" to the improvement of packaging yield. Rather it was a collection of many incremental improvements on many different unit processes, each one making yield a little better than before. The one constant among all of the improvements is cleanliness. Each one of the improvements mainly had something to do with cleanliness of the surface either through particulates or suspected surface chemistry modification. The major conclusion from this work is that MEMS must be kept as clean as possible after release. Each process must be scrutinized as to its effect on the MEMS and final surface chemistry.

5. Conclusion and Recommendations

In this broad suite of experiments we have documented failures in complex MEMS devices with contacting surfaces due to humidity and temperature over specified time intervals. In these same experiments, we have seen degradation of the FOTAS coverage and changes in the static friction coefficient of sidewall surfaces. Although there was a 50-nm particle density problem that interfered with many surface adhesion measurements, we observed the trend of higher Gamma Change as a function of humidity, temperature, and time interval. If we assume that the degradation mechanism is hydrolysis of the FOTAS chains, that may have an exponential dependence on water content (NEED REF) we can fit the most complete data set (TRA driving a load) to an Arrhenius-like model. We used the method of least squares to fit the data to this equation

$TF = A_0 e^{b(ppmv)} e^{E_a / k_b T}$ where TF is the predicted Time-to-Failure, A_0, b, and E_a are the fit parameters. We achieved a fit with $R^2 = 0.96$ and the parameters A_0, b, and E_a having values of 3.1 x 10^{-7} hours, -0.00122 $ppmv^{-1}$, and 1.0 eV, respectively. The fit lines corresponding to humidity levels of 520, 2000, and 5000 ppmv are shown in Figure 5.1. Also marked in the graph are the typical lifetime of 30 years and a temperature stress of 125°C.

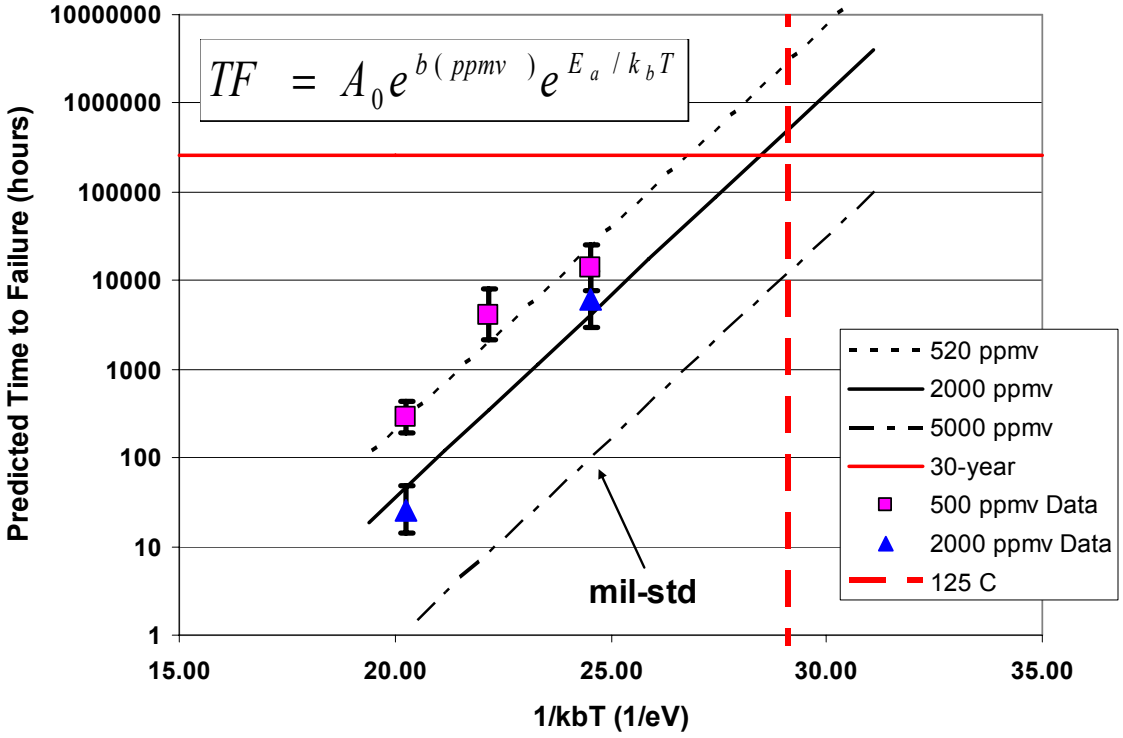

Figure 5.1 Failure data from TRA (one hub) device fit with an Arrenhius model. Lines represent predictions for various humidity levels. The number of hours to 30 years and the typical stress temperature of 125°C are also indicated.

There is only one hub region for the TRA driving a load. All of the failures were located in the gap in this region. It is apparent from the prediction that the military standard packaging humidity level of 5000 ppmv will not be sufficient for long-term storage. Levels of 2000 ppmv might be acceptable; levels of 500 ppmv probably will be acceptable.

The most robust MEMS device tested was the NVM in the unlatched state. In most cases there were zero failures to record which made predictive analysis difficult. In the unlatched state, there were no surfaces in contact which helped reduce any adhesion-related failures. There was one case (300°C, 500 ppmv, 200 hours) where material agglomerated under the dimple of a shuttle and caused failure. This dimple gap is less than 0.5 μm.

Device failures have been shown to relate to measurable changes in contacting surfaces using test structures and surface analysis techniques. Shorter time intervals at higher humidity produce the same surface degradation as longer times at lower humidity.

The results of this project suggest that if there are hubs in the design, a VSAM coating must be used to get reproducible yield through packaging. If the design is complex with many hubs, the device should be actuated after the coating process and before the packaging process. If the packaging humidity level is 2000 ppmv or less, a design with one hub may last 30 years in dormant storage.

Designs without hubs are robust. We saw zero failures in the TRA actuator throughout all these tests. However, surfaces in contact, such as a latched switch (NVM) may adhere. Designs should use high-force actuators to assure functionality.

The VSAM deposition process has been developed based on examination of water contact angle and the yield of working devices (microengines). While these factors are necessary measures of the success of the process, they are not sufficient to fully describe the chemistry of the treated surfaces on which adhesion and friction will depend. Applications where reproducibility in long term aging behavior is critical should require a more direct, quantitative measurement of the coverage of molecules used to control adhesion and friction. Direct measurement on SUMMiT modules requires the use of a technique such as ToF-SIMS, which has both the spatial resolution to select specific areas of a MEMS die for analysis, as well as the ability to determine the various compounds adsorbed on the surface. The ToF-SIMS data can be correlated to XPS measurements on larger analysis areas to quantify the areal density of specific molecules.

Appendix A: Lessons Learned

A.1 TRA Electrostatic Discharge Prevention

Even though we took proper ESD precautions (always wore grounded wrist-strap) when handling these packages, there were a significant number of failures caused by ESD events. The problem was related to the design of a set of comb fingers. As shown in Figure A.1, the tip of one finger gets close enough to discharge and adhered to the grounded, movable set of fingers. The design problem was that the length of the fingers did not follow the correct radial line from the center of the device resulting in a longer top finger. Note that the triangular fingers maintain the proper distance.

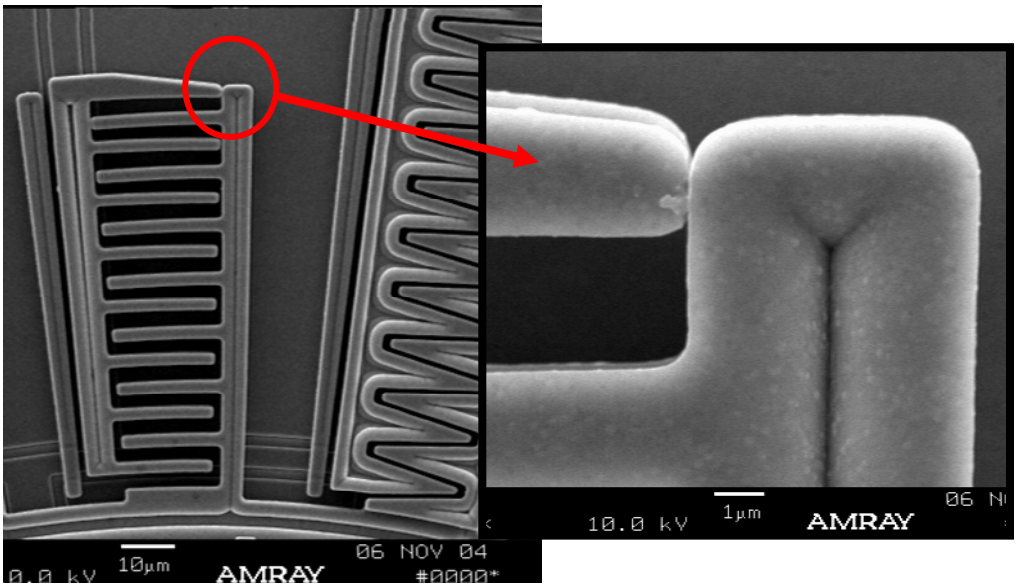

Figure A.1 SEM showing incorrect radial line on comb fingers resulting in electrostatic discharge and adhesion of the comb

We corrected the design by removing this small set of comb fingers. These fingers were fabricated only in the poly12 laminate and supplied a negligible amount of force to the actuator. The corrected version is shown in Figure A.2 where the two locations are indicated. An SEM image was also included to provide higher magnification of the region.

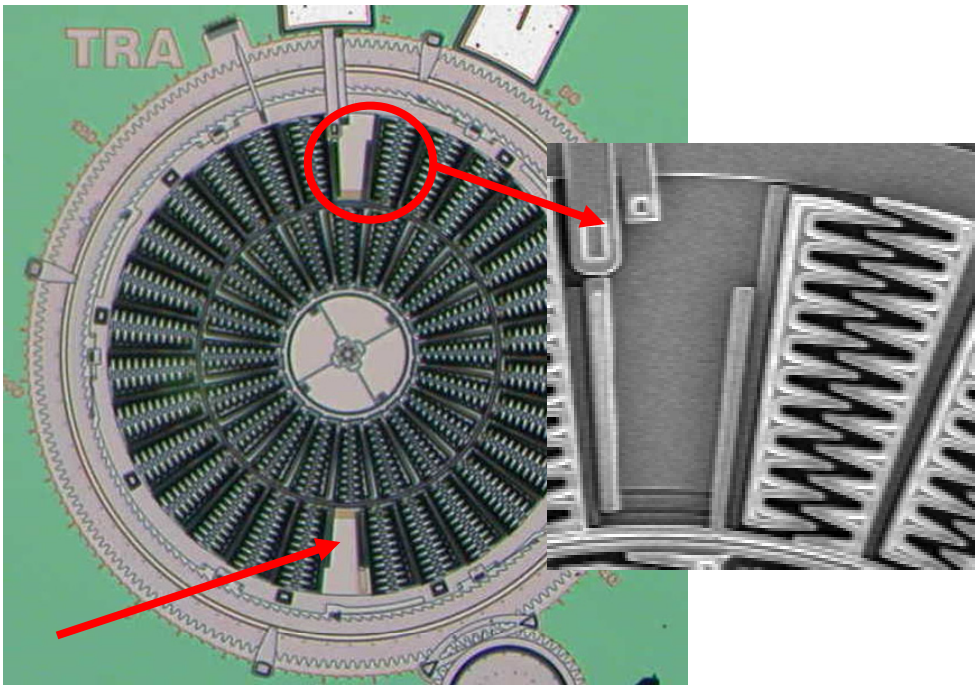

Figure A.2 Comb finger removal in the two ESD-susceptable areas noted. On the right is an SEM image of the region showing open (no voltage) triangular fingers.

These ESD events could also be minimized by the bond pad layout. The most susceptible package pins (for a 24-pin DIP package) are 1, 12, 13, and 24, the four corners. If these pins are tied to ground in the module (rather than supply voltage to an electrostatic actuator) ESD is less likely.

A.2 TRA Dimple Groove Solution

Dimples are used on gears to minimize the contact area and thus prevent stiction. The fabrication process also allows designers to add dimples to close gaps between layers for stability reasons. For some process runs, there was an over-etch into the lower layer producing a groove. The groove edge presented a likely spot for adhesion of the dimple, thus preventing motion of the radial comb actuators. In Figure A.3 we show a FIB cross section of a dimple region, which revealed a dimple groove. A dimple adhered to the groove edge is shown in Figure A.4 where a FIB cross section was performed which separated the dimple from the pawl anchor. Once separated, the restoring force of the springs in the actuator returned the actuator support to the as-fabricated rest position.

Failures of the TRA due to dimples adhering to the groove edge were random. They were very problematic to the dormancy experiments as they could have no relation to the stressing problem. The solution was to remove the dimples between poly3 and poly12 in the layout of the TRA. There was some concern about the stability of the actuator movement, but the device was rigid enough for that not to be an effect.

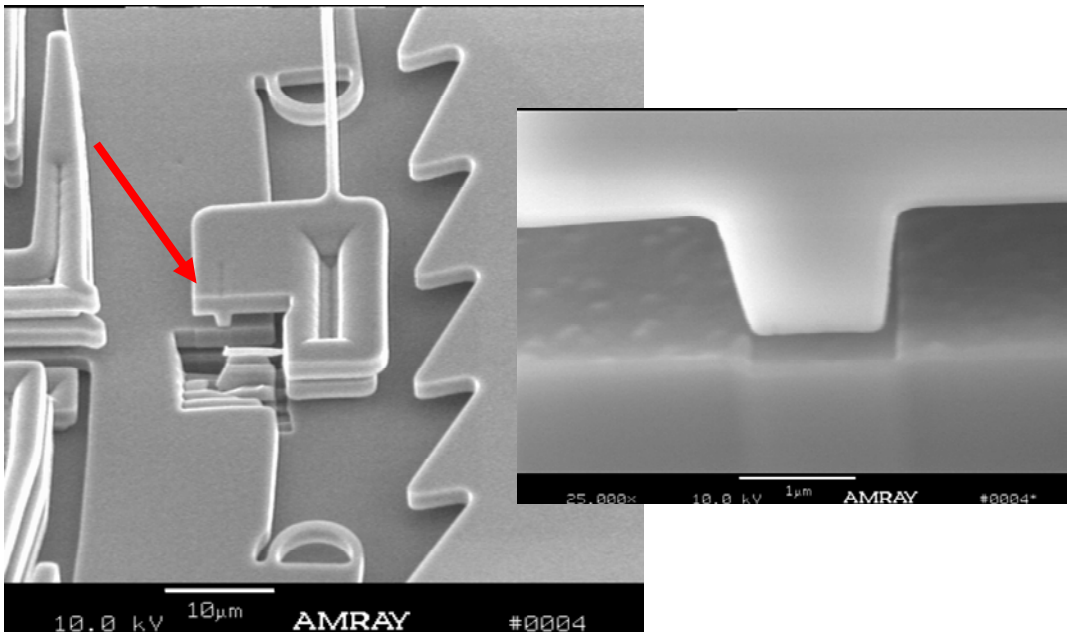

Figure A.3 The SEM image on the left shows the dimple region on the actuator support. The cut into that region was performed on a FIB. On the right is a high magnification of the dimple located in the groove.

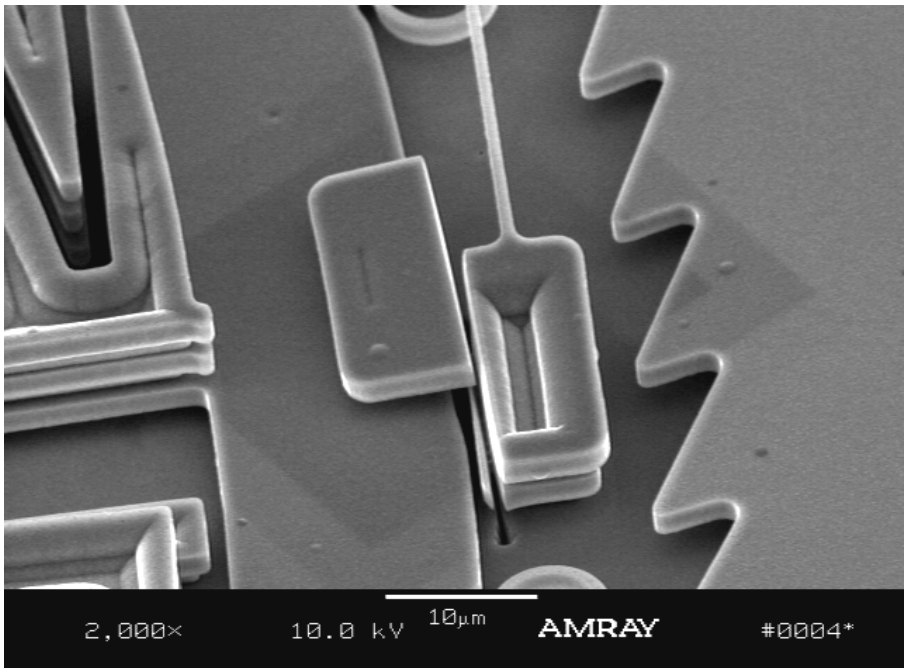

Figure A.4 After the FIB was used to cut the dimple region from the pawl anchor, the actuator ring moved back to its rest position, indicationg that the dimple was adhered in the groove.

A.3 Packaging and Yield

As mentioned in earlier sections, we stopped using the microengine actuator because of low yields through our packaging process. The packaging steps were only die attach and wire bond to the pads. We did not go through a lid seal because we were interested in environmental effects on the surfaces. The yield of devices is shown in Figure A.5 where the microengine driven DMS is included to show the very low values. There is a definite increase in yield for the TRA after the ESD fix which was described in Appendix A.1. Of note is the incredible yield of the NVMs which are the highest force actuators. Additionally, there is no surface in contact in the NVM during the packaging process. The dimple groove fix did not have a great effect on yield, but reduced our failure analysis effort greatly.

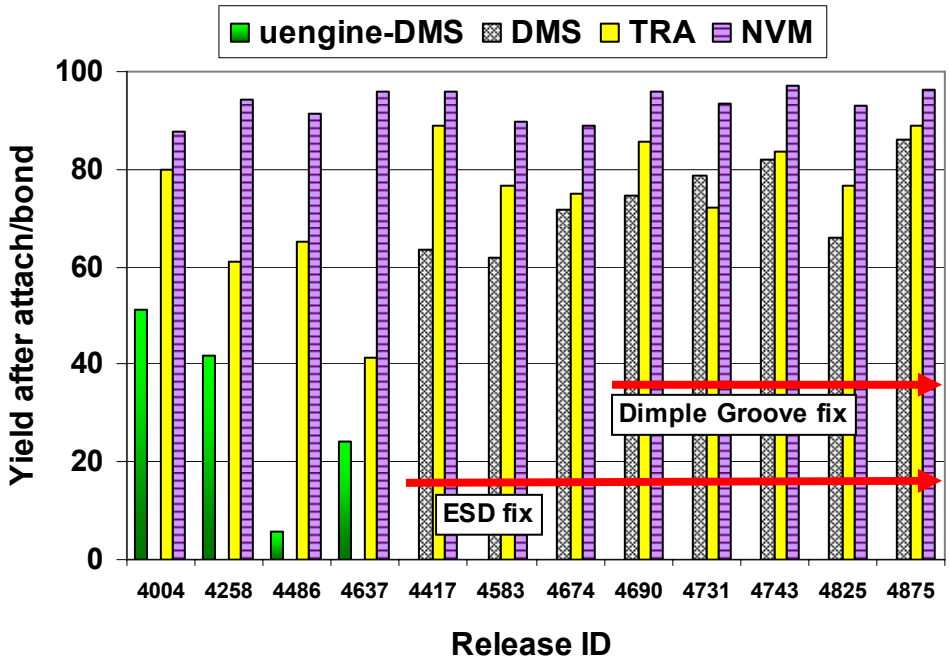

Figure A.5 The yield through the limited packaging process for the devices in the dormancy experiment.

The yield of the NVMs was so good that we did not test these devices at the die level, but waited until they were packaged and easier to test. We attempted to do the same for a subset of the DMS and TRA devices. Only one row and one column of the dice were tested for functionality before packaging. Unfortunately, for the DMS, these were the only devices that worked after packaging. The actuator combs showed slight movement, but not enough to break the gear train free, producing yields that were below 40%. A slight poke to the outer gear with a probe tip produced functioning devices. The TRA device (driving only one gear hub) yielded above 80% under the same conditions. We conclude that a complex MEMS device using many hubs should be actuated at the die level to insure functionality through the packaging process. In light of the fact that VSAM was demonstrated to be incapable of penetrating very small gaps in devices, it is

likely that gear hubs represent areas where some initial surface contact combined with a very convoluted path result in areas of the surface that are not covered. These areas are prime locations for adsorption of water or other contaminants during subsequent handling and processing, and can then lead to adhesion of the contacting surfaces.

A.4 Uniformity of the Surface Treatment Process

The analysis of many VSAM coated die with ToF-SIMS has shown that for a given coating process, the VSAM coverage is uniform on exposed as well as hidden areas of the surface. However, the ToF-SIMS measurements also showed that narrow gaps between surfaces may be insufficient for penetration of the FOTAS molecule during the coating process. MEMS designs will generally not contain large flat areas in contact without some dimple present to minimize the true contact area between the surfaces, such as those deliberately created in this work to test VSAM conformality. This result does suggest, though, that the FOTAS molecule cannot adsorb on surfaces that are in physical contact. Devices that contain contacting surfaces that are not otherwise suspended to maintain a gap during the coating process will therefore have microscopic areas that are not covered with FOTAS, corresponding to the real areas of contact created after the device is released. Given the roughness of polysilicon surfaces, these areas are probably on the order of nanometers to 10's of nanometers in diameter, and are too small to detect with surface analysis tools. They do provide a path for ingress of water to the base of the molecule where hydrolysis reactions can occur to remove the FOTAS molecules. They also provide sites for adsorption of contaminants that may also adhere the devices together. Possible solutions are to actuate devices at the die level during the coating process, or coat devices, remove and actuate to create different points of contact, and recoat immediately after actuation. Another solution would be to use a surface treatment with a mobile phase that can fill the defects in the VSAM layer, and actuate after coating to expose the previous real contact areas to allow the mobile phase to infill before subsequent processing.

Another important finding associated with the surface treatment process is that absolute FOTAS coverage levels vary significantly from run to run. This is the underlying reason that FOTAS degradation after humid environment exposure had to be measured by normalizing the measured FOTAS coverage after exposure to that before exposure. While factors such as water contact angle and percent of functioning devices used as process monitors during VSAM deposition may indicate that coverage is sufficient to prevent capillary adhesion in devices, previous work has shown that at the high levels of coverage the water contact angle is not sensitive to the amount of FOTAS present. Therefore, the process may yield high water contact angle and a large fraction of functioning devices, but this is due to the fact that water cannot adsorb on surfaces in these short term measurements. The surfaces may in fact exhibit large fluctuations in the amount of FOTAS present, and this would be expected to significantly impact the friction and durability of the monolayer in mechanical contacts, as well as the aging behavior of devices.

Finally, during the course of this project the surface analysis tools mentioned above were used to modify the VSAM process. The chamber is now cleaned using an oxygen plasma to reduce background levels of FOTAS in the deposition chamber that were present even when the FOTAS source was not exposed to the chamber. Further, since the standard VSAM deposition process did not result in saturation coverage, the process has been modified to produce FOTAS coverage closer to saturation. These changes should improve the uniformity of the process as well as the resistance of the surfaces to aging and adsorption of contaminants. The issue related to lack of FOTAS penetration at real areas of contact remains, however. Therefore, the best protection of MEMS surfaces may still require the use of a bound plus a mobile layer of lubricant.

Distribution:

1	MS0319	M.A. Polosky	02614
3	MS0372	T.J. Skousen	01524
3	MS0886	J.V. Cox	01526
3	MS0886	J.A. Ohlhausen	01822
1	MS0888	K.R. Zavadil	01823
1	MS0889	J.S. Custer	01824
1	MS0889	B.L. Boyce	01824
1	MS0889	T.E. Buchheit	01824
3	MS0889	M.T. Dugger	01824
1	MS0889	S.M. Thornberg	01825
3	MS1064	M.A. Duesterhaus	02619
1	MS1064	E.J. Garica	02614
1	MS1069	M.S. Baker	017691
3	MS1069	S.A. Candelaria	017691
3	MS1069	T.B. Parsons	017691
3	MS1069	D.M. Tanner	017691
3	MS1076	B. Jokiel, Jr.	017452
1	MS1080	A.D. Corwin	01749
1	MS1080	M.P. De Boer	01769
1	MS1080	P.J. Resnick	01749
1	MS1080	D.R. Sandison	01769
3	MS1081	M.W. Jenkins	01739
1	MS1084	P.J. Clews	01746
1	MS1084	M.G. Hankins	01746
2	MS9018	Central Technical Files	8944
2	MS0899	Technical Library	4536
1	MS0123	D. Chavez, LDRD Office	1011